SINGLE-MOLECUE STUDY ON GPIB-ALPHA AND VON WILLEBRAND FACTOR MEDIATED PLATELET ADHESION AND SIGNAL TRIGGERING

A Dissertation

Presented to

The Academic Faculty

by

LINING JU

In Partial Fulfillment

of the Requirements for the Degree

Doctor of Philosophy in the

School of Biomedical Engineering

Georgia Institute of Technology

December 2013

SINGLE-MOLECUE STUDY ON GPIB-ALPHA AND VON WILLEBRAND FACTOR MEDIATED PLATELET ADHESION AND SIGNAL TRIGGERING

Approved by:

Dr. Cheng Zhu, Advisor
Wallace H. Coulter Department of
Biomedical Engineering
Georgia Institute of Technology
and Emory University School of Medicine

Dr. Larry V. McIntire
Wallace H. Coulter Department of
Biomedical Engineering
Georgia Institute of Technology
and Emory University School of Medicine

Dr. W. Robert Taylor
Wallace H. Coulter Department of
Biomedical Engineering
Georgia Institute of Technology
and Emory University School of Medicine

Dr. Jennifer E. Curtis
School of Physics
Georgia Institute of Technology

Dr. Jing-fei Dong
Hematology Division, Department of
Medicine
University of Washington, Seattle

Date Approved: November 11, 2013

To my dearest family.

I dedicate this thesis

to

My parents

I am forever indebted to my parents, 居礼 (**Li Ju**) and 孙淑 (**Shu Sun**). I would not have been able to finish my Ph.D. thesis without their priceless love, endless patience and unconditional supports.

My girlfriend

I am so grateful to my girlfriend, **Danmei Fan,** who was always there to support, comfort and encourage me to go through hardship.

ACKNOWLEDGEMENTS

TABLE OF CONTENTS

LIST OF FIGURES

LIST OF ABBREVIATIONS

ADP	Adenosine diphosphate
Arg	Arginine (also R), an amino acid
Asp	Aspartic acid (also D), an amino acid
BSA	Bovine serum albumin
BFP	Biomembrane force probe
CHO	Chinese hamster ovary
DBS	Dynamic bond stiffening
E. coli	Escherichia coli
FITC	Fluorescein isothiocynate
Gly	Glycine
GOF	Gain-of-function
GPIbα	Glycoprotein Ibα
GPIIb/IIIa	Glycoprotein IIb and IIIa (integrin $\alpha_{IIb}\beta_3$)
HRP	Horseradish peroxidase
HSA	Human serum albumin
k_{off}	Off-rate
k_{on}	On-rate
LOF	Loss-of-function
pt-VWD	Platelet type von Willebrand Disease
RGD	Arginine-Glycine-Aspartic Acid

PBS	Phosphate buffered saline
PZT	Piezoelectric translator
VWD	von Willebrand disease
VWF	von Willebrand factor
γ	Shear rate
MD	molecular dynamics
WT	Wild type
μ	Viscosity

SUMMARY

Platelet adhesion plays a key role in forming a hemostatic plug at the site of vessel breach (hemostasis) or occlusive arterial thrombi at the site of atherosclerosis plaque (thrombosis). After vascular injury, a number of subendothelial matrix proteins become exposed to blood, including von Willebrand factor (VWF), collagens, fibronectin (FN) and fibrinogen, which support platelet adhesion through the engagement of specific receptors. In the current view, under conditions of rapid blood flow, as occurs in arterioles or atherosclerotic arteries with restricted lumen, platelet adhesion is initiated in a two-step cascade: 1) Fast tethering mediated by binding of glycoprotein Ibα (GPIbα), the ligand-binding subunit of the GPIb-IX-V complex, to the A1 domain of VWF immobilized on collagen, recruits platelets to the site of vascular injury. However, A1–GPIbα interaction can only support translocation (rolling) with stop- and-go motion due to its rapid on-/off-rate. Mutations in VWF and/or GPIbα may alter the mechanical regulation of platelet adhesion at this step and cause bleeding disorders as found in patients with von Willebrand disease (VWD). 2) Stable adhesion mediated by integrins, such as $\alpha_{IIb}\beta_3$ bound to the Arg-Gly-Asp (RGD) motif in the VWF or fibronectin. Activated $\alpha_{IIb}\beta_3$ serves also to immobilize plasma proteins, mainly VWF and fibrinogen, on the surface of adherent platelets to propagate thrombus formation through crosslinking. Although it seems clear about the general procedure of thrombus formation, the detailed molecular events such as how VWF interacts with platelet especially under pathophysiological shear forces and how a mechanical stimulus is translated into

transmembrane biochemical signals to connect the two-step cascade are not well understood.

To explore these questions regarding force, binding kinetics and signal transduction, an advanced single molecule tool, the 2nd generation biomembrane force probe (BFP-2), was built. The spatial and temporal precisions of the BFP-2 were about 2 nm and 0.4 ms respectively. The spring constant of the BFP force probe was set over a wide range from 0.1 pN/nm ~ 1.2 pN/nm by adjusting aspirating pressures on the force probe. The separation distance between a receptor and a ligand could be controlled due to a double-edge tracking algorithm. Thus, this instrument allowed us to measure force-dependent lifetimes of individual molecular bonds with a force sensitivity of ~1 pN, to determine the formation and association of individual bonds and to estimate kinetics. Moreover, a new protocol has been developed to capture the fresh human platelets on a target micropipette for the single-platelet manipulations. Most importantly, to study the mechanotransduction at the single platelet level and to prove GPIbα acting as a mechanosensor, we upgraded the BFP into the fluorescence BFP (fBFP) to simultaneously analyze 2D kinetics and observe Ca^{2+} signaling in the same platelets loaded with fura-2 dye by ratiometric imaging. A customized temperature controller was integrated into the fBFP system to maintain platelets at 37 °C.

The new BFP brought us new insights on platelet adhesion, which can be ascribed to following biophysical mechanisms:

1) VWF–GPIbα catch bond: VWF–GPIbα displays a counterintuitive behavior called catch bond that a force prolongs rather than shortens the lifetime of the VWF–GPIbα bond. The causal relationship between catch bonds and flow-enhanced adhesion (increasing flow augments cell adhesion despite higher dislodging forces) has been established for platelet rolling on VWF. The VWF-A1 N-terminal flanking region (Q1238-E1260) is a key structural determinant of the VWF-GPIbα catch bond. It plays a key role in stabilizing the A1-GPIbα interaction under force, because truncating this sequence eliminated the A1 catch bond with GPIbα. Type 2B VWD A1 mutations unanimously eliminated the catch bond by prolonging lifetimes at low forces.

2) Transport dependent VWF–GPIbα association: GPIbα plays a pivotal role in tethering platelets at the high shear due to the rapid VWF–GPIbα on-rate under dynamic shear conditions where various transport mechanisms are at work. We found that the gap distance between A1- and GPIbα-bearing surfaces modulated the apparent on-rate. A distance threshold about 80 nm (beyond which bond formation became prohibitive) was identified to be the total length of the receptor and ligand molecules. The BFP spring constant and diffusivity of the protein-bearing beads also significantly influenced a measured on-rate in accordance to the hypothesized transport mechanism.

3) GPIbα mediated mechanotransduction: GPIbα binding to VWF may initiate a platelet activation cascade. However, the mechanism by which binding a receptor

on platelet surface triggers intracellular signaling remains poorly understood. Using the newly developed fBFP and manipulating a single human discoid platelet, we showed a 25-pN force prolonged VWF–GPIbα bond lifetimes for A1WT (catch) but shortened those for 2B mutant (slip). Both the magnitude and duration of a force are important for triggering as the maximal Ca^{2+} was induced by 25-pN force applied via A1WT. This force produced the longest lifetime for the A1WT catch bond but the shortest lifetime for the 2B mutant A1R1450E slip bond, which did not trigger Ca^{2+}. The strong correlation between bond lifetimes and triggered Ca^{2+} levels across various A1 constructs supports a model where mechanical force and structural variation regulate platelet signaling via the engagement duration of VWF–GPIbα, suggesting that GPIbα is a mechanosensor. A type 2B A1 mutation that rapidly reduced a A1–GPIbα bond lifetime with increasing forces and a type 2M A1 mutation that globally shortened a bond lifetime induced the same net outcome: Inefficient Ca^{2+} triggering at high forces. This suggests a new concept about VWD: the signaling defect.

4) GPIbα triggered integrin priming: We developed a novel BFP "switch" assay to investigate the sequential bindings of platelet to GPIbα and integrin $\alpha_{IIb}\beta_3$. We found that the $\alpha_{IIb}\beta_3$ binds to the FN with an intermediate cellular affinity following the GPIbα induced Ca^{2+} signal. Note that the platelet shape remains discoid for the entire experiment suggesting this GPIbα induced integrin priming is activation independent. Although the FN– $\alpha_{IIb}\beta_3$ has a low binding propensity under the high shear condition due to its small on-rate, it may play an adhesion

reinforcement role to support initial GPIbα mediated tethering under high shear condition, and such reinforcement requires the initial mechanosignaling from GPIbα. This could be the mechanism that GPIbα cooperates with integrin $\alpha_{IIb}\beta_3$ in promoting the initial formation of discoid platelet aggregates at a shear rate in the arterial microcirculation or in regions of arterial stenosis.

CHAPTER 1: INTRODUCTION

1.1 Specific aims

Platelet adhesions play a key role in the initiation of hemostasis and thrombosis. von Willebrand factor (VWF), a multimeric protein circulating in the plasma, functions as the main clotting factor to induce platelet aggregation and thrombus formation in blood vessels subjected to high haemodynamic shears (Ruggeri, 2002; Andrews and Berndt, 2004; Jackson, 2011). The early platelet adhesion features a two-step cascade: 1) VWF is engaged to the glycoprotein (GP) Ib-IX-V receptor complex on platelet mediated via the binding of A1 domain of VWF to the GPIbα subunit of the complex; 2) VWF promotes the expansion of the platelet plug by cross-linking platelets via the binding of C1 domain of VWF to GPIIb/IIIa (or integrin $\alpha_{IIb}\beta_3$) (Ruggeri and Mendolicchio, 2007; Jackson et al., 2009; Ruggeri, 2009). The regulation of this early adhesion process is crucial: insufficient adhesion cannot stop bleeding to maintain hemostasis while excessive adhesion results in thrombosis (Lenting et al., 2010). Therefore it is essential that VWF-platelet interactions occur timely. Researchers have long used flow chambers (Doggett et al., 2002; Doggett, 2003; Kumar et al., 2003; Yago et al., 2008; Coburn et al., 2011) and microfluidic devices (Gutierrez et al., 2008; Tovar-Lopez et al., 2010; Colace and Diamond, 2013) to mimic blood flow so as to uncover regulatory mechanisms of platelet adhesion. However, the molecular basis for platelet adhesion remain poorly understood due to two major limitations of traditional approaches: 1) low temporal and spatial resolutions and 2) insufficient capabilities to characterize kinetics of these molecular interactions. We propose to use single-bond experiments with a newly built

biomembrane force probe (BFP) that has improved force/distance-precision, reduced noise and added fluorescence imaging capability to systematically characterize adhesion and signaling functions of the mechanoreceptor GPIbα. Our specific aims are:

Specific Aim 1: To study how VWF regions surrounding A1 regulates the VWF–GPIbα interaction under mechanical forces.

Circulating platelets do not bind VWF in plasma unless putative conformational changes occur around its A1 domain that exposes the GPIbα binding site (VWF activation) by a hemodynamic force. Many lines of evidence suggest that the N-terminal flanking sequence Q1238-E1260 of the VWF-A1 plays an important role in the VWF activation. In addition, using long constructs with this sequence (N-longer A1) and the shorter constructs without this sequence (N-shorter A1) resulted in discrepant observations in previous studies. Thus, the biophysical and structural basis of how the VWF–GPIbα interaction is regulated remains unclear in part because of discrepant data. Here we used a BFP and a flow chamber to gain mechanistic insights into the regulatory effects of VWF regions surrounding A1, especially its N-terminal flanking region, on the force-dependent VWF–GPIbα interaction in the following steps:

i) Used a BFP to analyze the single-bond dissociation of GPIbα from VWF, N-longer A1 (1238-A1) and N-shorter A1 (1261-A1) under forces lower than those previously studied in the absence and presence of the Q1238-E1260 peptide in the solution.

ii) Used a BFP to examine the effect of structural variation on intrinsic VWF–GPIbα kinetics. The following wild-type (WT) and mutant constructs of GPIbα or VWF-A1 were studied.

Table 1-1. The WT and mutant constructs of GPIbα and VWF-A1 monomers used.

GPIbαN		VWF-A1	
Glycocalicin (GC)	WT	1238-A1	WT
GPIbα from platelet lysates	WT	1261-A1	WT
GPIbα from CHOαβ9 lysates	WT	1238-A1, R1450E	Type 2B VWD (GOF)
GPIbα, G233V from CHOαβ9 lysates	β-switch mutants, Platelet-type VWD (GOF)	1238-A1, I1309V	Type 2B VWD (GOF)
		1238-A1, R1306Q	Type 2B VWD (GOF)
		1238-A1, G1324S	Type 2M VWD (LOF)
		1238-A1, V1279I	Type 2M VWD (LOF)

iii) Used a flow chamber to measure the rolling velocity of washed platelets over VWF, 1238- and 1261-A1s immobilized glass surfaces under different shear

rates. To investigate the significance of the N-terminal sequence with a functional assay, whole blood mixed with soluble Q1238-E1260 polypeptide or scramble control polypeptide was also perfused over collagen-, VWF- and A1-coated surfaces.

Results from these experiments can help pinpoint structural determinants of the VWF–GPIbα bond regulation, to explain the discrepant published data, and to elucidate regulating mechanisms for VWF to be activated by hemodynamic force generated in the flowing blood.

Specific Aim 2: To characterize physical regulation of VWF–GPIbα 2D association.

A two-dimensional (2D) cell membrane may alter the affinity and on/off rates by several orders of magnitude to reveal a highly dynamic level of protein interactions. We hypothesized two biomechanical mechanisms for the flow-enhanced platelet adhesion to VWF: transport-dependent acceleration of bond formation and force-dependent deceleration of bond dissociation. The former may include three distinct transport modes: sliding of platelet bottom on the vascular surface, Brownian motion of platelets, and rotational diffusion of the interacting molecules, and the latter may involve a counterintuitive behavior called catch bonds where force prolongs rather than shortens the lifetime of the VWF–GPIbα bond. To elucidate these mechanisms, we used a BFP to answer two key questions:

4

i) How does transport regulate the VWF–GPIbα formation?

ii) How does force regulate VWF–GPIbα dissociation?

Specific Aim 3: To study how force triggers platelet calcium signaling via GPIbα.

Although GPIbα has long been hypothesized as a mechanosensor, the connection between its functions in adhesion and signaling is still poorly characterized on the molecular level. Before this study, it has been clear that intra- and inter-cellular processes could generate force that would impact receptor-ligand interactions. Most previous studies on platelet signal transduction were done under conditions either in the absence of force or with complex flow. Here we aimed to demonstrate that mechanical force regulates platelet triggering in the following subaims:

i) Defined the elongated interactions of VWF–GPIbα catch bonds as the fundamental property required for optimal platelet triggering. To directly interrogate triggering with response, we concurrently analyzed 2D VWF-A1–GPIbα kinetics and intracellular Ca^{2+} signaling at the level of single GPIbα bond using BFP and fluorescence imaging (fBFP). This technique allowed us to determine that A1–GPIbα catch bond efficiently lead to Ca^{2+} release without contributions from other receptors.

ii) Used the BFP "switch" assay to show the sequential binding from GPIbα and $\alpha_{IIb}\beta_3$ and verified the hypothesis that calcium signal following the VWF-A1–GPIbα engagement can prime platelet integrins to bind VWF and/or fibronectin.

Findings from these experiments would help answer a fundamental question in platelet biology as how a platelet is triggered in response to hemodynamic force.

1.2 Background and significance

1.2.1 *Molecular interactions that mediate platelet adhesion to subendothelial surfaces*

When blood vessels are disrupted, circulating platelets adhere to the exposed subendothelial surface and recruit platelets into aggregates that function as a procoagulant surface (Figure 1) (Ruggeri et al., 1999; Jackson et al., 2000; Andrews and Berndt, 2004; Ruggeri and Mendolicchio, 2007; Jackson et al., 2009). Insufficient adhesion may result in prolonged bleeding, thereby upsetting hemostasis. However, excessive adhesion can be prothrombotic (Lenting et al., 2010). Elucidating how platelets interact with each other and with the subendothelial matrix at sites of injury will help us better understand the pathogenesis of diverse thrombotic and bleeding disorders, understanding the biophysical regulation of platelet adhesion will help us better solve clinical issues such as a partial luminal obstruction (a developing thrombus, an atherosclerotic plaque or an intravascular device), a change in vessel geometry (extrinsic constriction of blood vessels, vascular bifurcation or aneurysm) or sudden flow changes (vessel hypoperfusion due to shunting or upstream obstruction) (Jackson et al., 2009; Jackson, 2011).
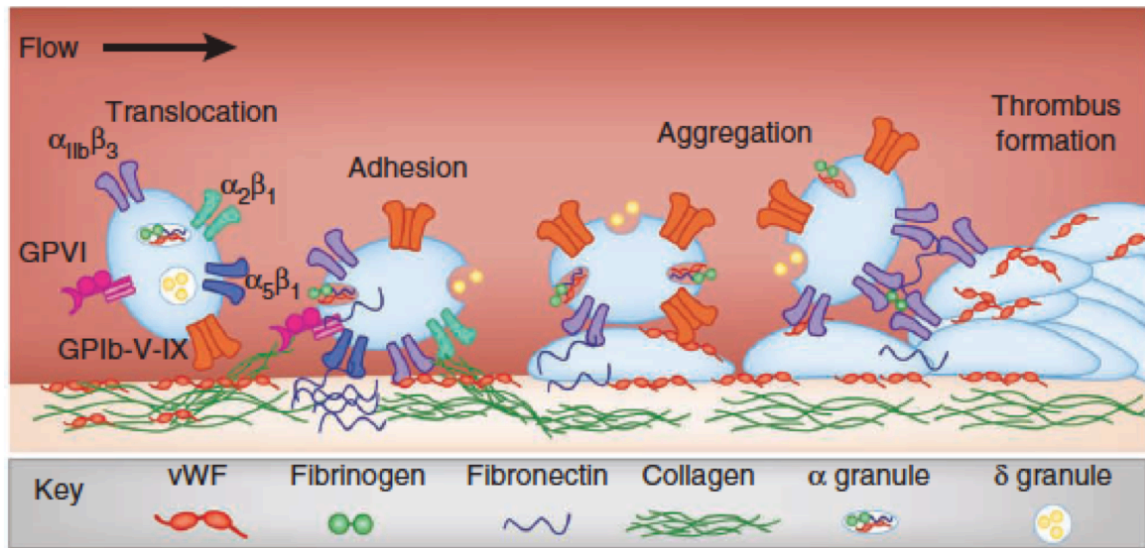
Figure 1-1. A model of platelet adhesion cascade in hemostasis and thrombosis. At the early stage, platelets are recruited to the injured vessel wall from flowing blood through the specific interaction of the platelet GPIb-IX-V complex with collagen-bound VWF exposed on the subendothelium. This ligand-receptor interaction has a rapid on-/off- rate that supports platelet translocation at the vessel wall. Stable platelet adhesion occurs through the binding of platelet GPVI to fibrillar collagen as well as the ligation of multiple β_1 integrins, including the collagen–$\alpha_2\beta_1$ interaction and fibronectin engagement of $\alpha_5\beta_1$. After the early stage adhesion, once firmly adhered, platelets undergo a series of biochemical changes that induce integrin $\alpha_{IIb}\beta_3$ activation, leading to the high affinity interaction with adhesion proteins including VWF, fibrinogen and fibronectin. These adhesive interactions are indispensable in the ability of platelets to form stable aggregates with other activated platelets and promote thrombus growth. Major ligands and receptors mediating platelet adhesion at sites of vascular injury are indicated in the bottom. Adapted and modified from (Jackson, 2011).

Vascular injury exposes a number of subendothelial matrix proteins that are capable of binding to their corresponding platelet receptors, including VWF–GPIb-IX-V (Ruggeri et al., 1999; Ruggeri, 2009), collagen–GPVI/$\alpha_2\beta_1$ (Cruz et al., 2005), fibronectin–$\alpha_5\beta_1$ and laminin–$\alpha_6\beta_1$ (Ruggeri, 2009) (Figure 1-1). The relative contributions of individual receptor-ligand interactions to the platelet adhesion cascade depends on the blood flow and the extent of vascular injury (Ruggeri et al., 1999; Jackson et al., 2009; Jackson, 2011). Under conditions of rapid blood flow, as occurs in arterioles

and stenotic arteries, GPIb complex plays a pivotal role in tethering platelets to and roll (or translocate) on VWF that is bound to collagen on the subendothelium at the early stage (Figure 1-1). However, the bond between GPIbα and VWF has an intrinsically rapid off-rate that does not support stable adhesion independent of other ligand-receptor interactions (Savage et al., 1998). As a consequence, platelets typically translocate over a VWF substrate (Figure 1-1) and require the engagement of collagen, fibronectin or laminin to their corresponding β_1 integrin receptors (Figure 1-1). As the stably adhered platelets become activated, they arrest on the disrupted vessel wall and form platelet plugs through interactions of β_1 and β_3 integrins with adhesive ligands such as collagen, fibrinogen, fibronectin, and VWF itself (Ruggeri et al., 1999; Ruggeri, 2002; Andrews and Berndt, 2004; Jackson, 2011). This process resembles the multistep adhesion and signaling cascade of leukocytes at sites of inflammation where the initial tethering and rolling of leukocytes on endothelium is mediated by interactions of selectins with ligands.

The GPIb-IX-V complex consists of 4 subunits GPIbα, GPIbβ, GPIX, and GPV (Clemetson, 2007; Du, 2007; Li and Emsley, 2013). The VWF binding site is located at the N-terminal domain (GPIbαN) of the GPIbα subunit, which also includes a heavily glycosylated long stalk, a transmembrane domain, and a cytoplasmic tail (Figure 1-2). GPIb–IX is a highly stable complex containing GPIbα, GPIbβ and GPIX in a ratio of 1 : 2 : 1 (Luo et al., 2007) (Figure 1-2). In contrast to the tight association between GPIb and GPIX, GPV is weakly associated with GPIb-IX through the transmembrane domains (Mo et al., 2012) (Figure 1-2). The structural details of the association of GPIb–IX with GPV await further elucidation, but it is very possible that GPIb–IX exists as the least independent functional protein complex on the platelet surface.

VWF is a multimeric protein composed of identical 250-kD subunits (Figure 1-3). Each subunit has 12 domains, including D1-D3 domains that are cleaved in the matured VWF. Of particular interest to this proposal are three A-type domains: a 24-kD A1 (residues 1272-1458, the VWF numbering in my thesis adds the first 763 propeptide residues of the D1-D2 domains), a 22-kD A2 (residues 1494-1670), and a 23-kD A3 (residues 1686-1872) (Sadler, 2005b; Ruggeri, 2007; Springer, 2011). Endothelial cells initially secrete ultralarge forms of VWF (ULVWF), which are hyperactive and readily bind platelet GPIbα. ULVWF is quickly cleaved by the plasma protease ADAMTS13 to yield smaller and less active VWF, which still typically exceed 1,000 kD (Dong et al., 2002; Springer, 2011; Gandhi et al., 2012). VWF becomes activated upon binding to collagen in the subendothelium, which enables flow-dependent, GPIbα-mediated platelet adhesion. A1 domain contains the binding site for GPIbα. A2 domain contains the cleavage site for ADAMTS13. Both A1 and A3 contain binding sites for collagen (Figure 1-3) (Morales et al., 2006; Auton et al., 2012).
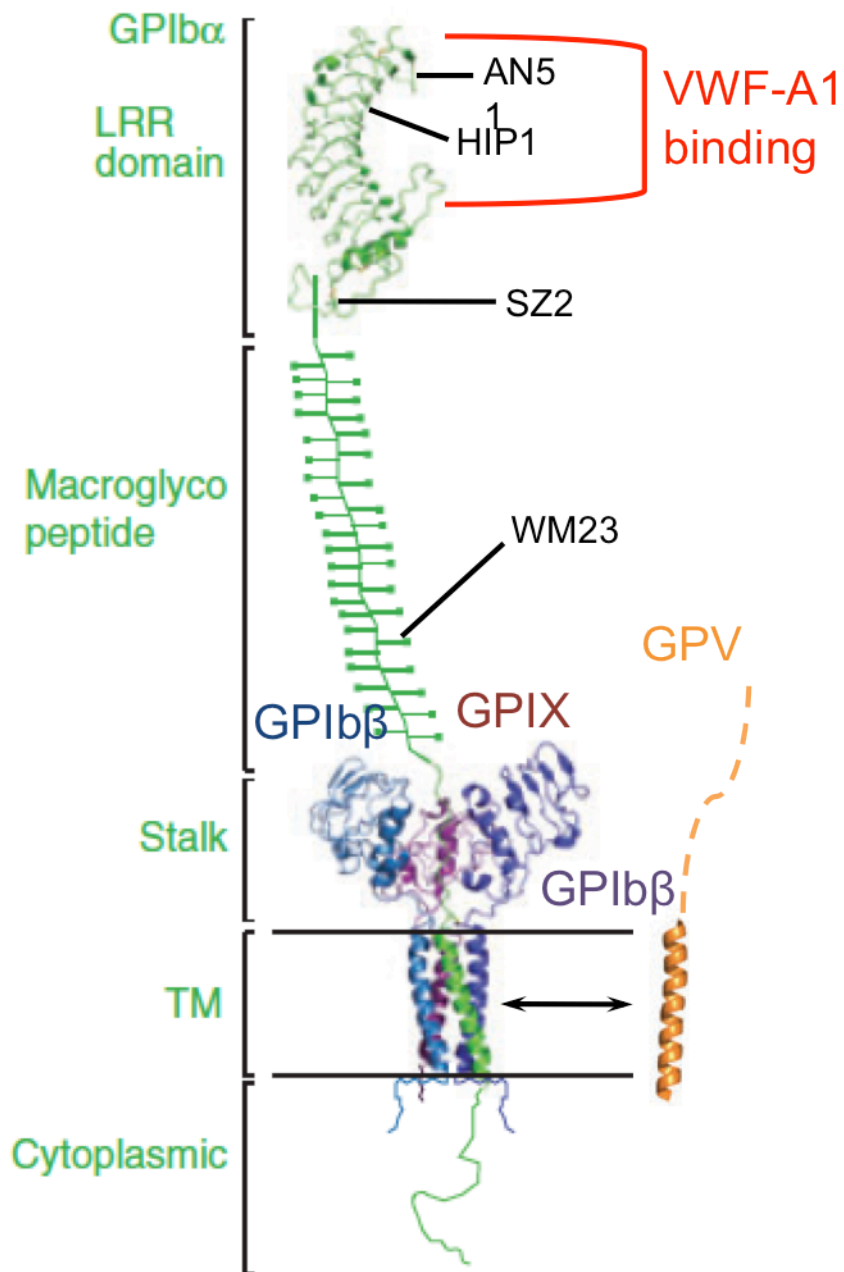
Figure 1-2. The latest model of the GPIb-IX-V complex largely drawn as ribbon diagrams. GPIbα (green), GPIbβ (blue) and GPIX (purple) subunits are colored differently. Various parts of GPIbα are labeled on the left. The weak interaction of GPV (orange) with GPIb–IX is through transmembrane (TM) domains. The binding region for the VWF-A1 is marked in red and the binding epitopes for mAbs AN51, HIP1, SZ2 and WM23 are also indicated. Adapted and modified from (Li and Emsley, 2013).
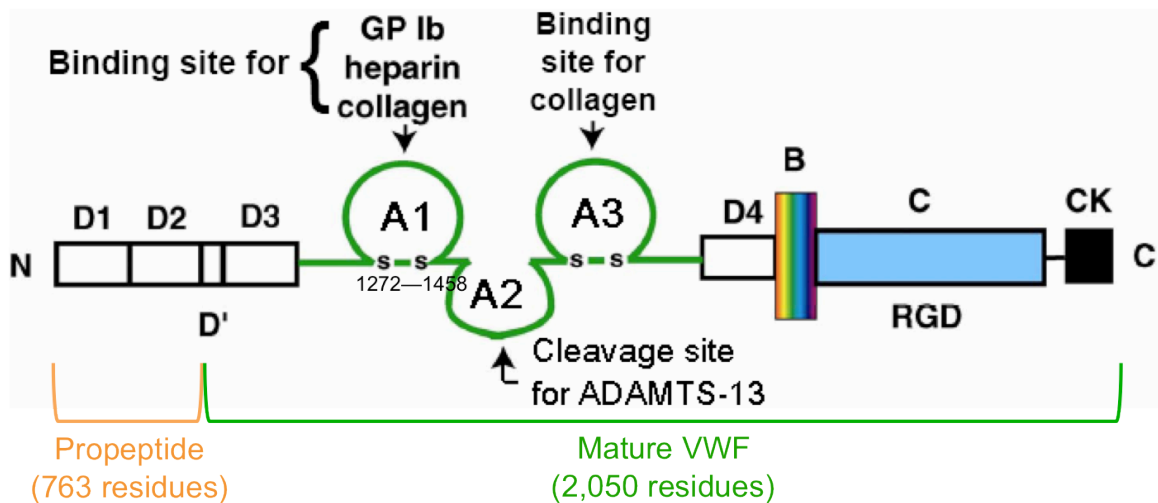
Figure 1-3. The VWF domain organization. Within each monomer of this multimeric protein, VWF contain a triplicate repeat sequence of A domains in the central portion of the 2,050-residue mature subunit (D'-D3-A1-A2-A3-D4-B-C). The A1 domain (the disulfide loop C1272-C1458) contains contact sites for the platelet GPIbα, heparin, and collagen. Its homologous A3 domain binds only collagen. The central A2 domain contains a proteolytic site for the metalloprotease ADAMTS-13.

1.2.2 _Kinetic and mechanical properties of VWF–GPIbα interaction_

A central feature of hemostatic responses is that platelet adhesion to a vascular surface occurs in a mechanically stressful environment of the circulation. This implies that VWF–GPIbα binding must have rapid kinetics because the fast rolling of platelets on VWF requires that adhesive bonds form and break rapidly. A series of flow chamber studies support this concept (Doggett et al., 2002; Doggett, 2003; Kumar et al., 2003; Yago et al., 2008; Coburn et al., 2011). Surprisingly, radioimmunoassay in the fluid phase yielded orders-of-magnitude slower kinetic rates for interactions between GPIbα and VWF (Miura et al., 2000). This finding underscores the difference between binding of soluble molecules to the cell surface (three-dimensional, or 3D, interaction) and binding of molecules on apposing membranes (two-dimensional, or 2D, interaction)

(Dustin et al., 2001; Huang et al., 2010; Zhu et al., 2013). In my study, we systematically measured 2D kinetics of VWF–GPIbα interactions.

In addition to placing a constraint on the kinetic and mechanical properties of the VWF–GPIbα interaction, the hydrodynamic forces also regulates platelet adhesion by affecting these properties. The relative motion between flowing platelets and a vascular surface brings GPIbα to the vicinity of VWF to promote the bond formation. However, the same motion also takes the two molecules apart and limits the time for them to bind. Moreover, bonds thus formed are subjected to force, which affects their dissociation. How force regulates the rate of biochemical interactions is a fundamental issue.

1.2.3 *Flow-enhanced platelet adhesion to the vessel wall*

It has long been recognized that increasing shear rate leads to the increased deposition of platelets onto thrombogenic surfaces and the rate of thrombus growth (Weiss et al., 1978; Turitto and Baumgartner, 1979; Baumgartner et al., 1980). A cardinal feature of GPIb-mediated platelet rolling on VWF is its flow dependence (Savage et al., 1996; 1998). Counterintuitively, flow enhances rather than impedes platelet adhesion, despite the dislodging fluid shear forces (Yago et al., 2008). Indeed, a minimal flow rate is required for platelets to tether to and roll on VWF (Doggett et al., 2002; Doggett, 2003; Yago et al., 2008). Platelets usually do not adhere to VWF at lower flow rates, and rolling platelets detach if arterial flow rates are reduced. This intriguing phenomenon may be ascribed to three distinct force-dependent mechanisms:

1) VWF activation: Circulating plasma VWF has a limited binding potential for GPIb due to its autoinhibitory mechanism (Ulrichts et al., 2006; Auton et al., 2012); however, once immobilized onto subendothelial collagen (type I, III and

VI) and exposed to hemodynamic drag forces, VWF macromolecule adopts an unfolded conformation that facilitates the engagement of A1 to GPIbα (Barg et al., 2007; Schneider et al., 2007).

2) VWF–GPIbα catch bond: VWF–GPIbα displays a counterintuitive behavior called catch bond that force prolongs rather than shortens the VWF–GPIbα bond lifetime. The causal relationship between catch bonds and flow-enhanced adhesion (increasing flow augments cell adhesion despite higher dislodgment forces) has been established for platelet rolling on VWF (Yago et al., 2008). Similar mechanism also explains flow-enhanced leukocyte rolling (Yago et al., 2004; Long et al., 2006).

3) Mechanotransduction: Upon binding to VWF, GPIbα transduces signals necessary for integrin $\alpha_{IIb}\beta_3$ affinity upregulation, which was regarded as an response to the stimulus of shear stress (Mazzucato et al., 2002; 2007). Under a flow condition, the interaction of platelet GPIbα with VWF leads to 2 distinct types of calcium (Ca^{2+}) elevations correlated with the sequential stages of GPIbα signal transduction and integrin $\alpha_{IIb}\beta_3$ binding enhancement: the first stage features a intracellular Ca^{2+} peak in a short time frame and appears to have been initiated by mechanical stimulation via GPIbα (Mazzucato et al., 2002; Nesbitt et al., 2002); while the second stage is considered as a stronger Ca^{2+} influx that correlates with $\alpha_{IIb}\beta_3$, although specific pattern characterization and triggering pathway still remains controversial. Nevertheless, the first stage of Ca^{2+} release from the internal storage appears to be more important than the second stage Ca^{2+} influx

because it is a signal from VWF/GPIb-IX-V to $\alpha_{IIb}\beta_3$ that occur independently of other receptors leading to activation of $\alpha_{IIb}\beta_3$ (Kasirer-Friede et al., 2004).

Other than the biophysical regulation, flow-enhanced platelet adhesion can also be regulated biochemically, i.e., by modulators botrocetin and ristocetin, which induce VWF–GPIbα binding at lower shears (Andrews et al., 1989; Girma et al., 1990). Flow-enhanced platelet adhesion can also be altered by structural variations. For example, the GPIbαN mutations M239V (Russell and Roth, 1993; Moriki et al., 1997) and G233V (Miller et al., 1991; MURATA et al., 1993) as well as the A1 mutation I1309V (Federici et al., 1997) also lower the shear requirements for VWF binding (Doggett et al., 2002; Doggett, 2003); These gain-of-function (GOF) mutations occur naturally in patients with platelet-type VWD or type 2B VWD who have prolonged bleeding time. Flow-enhanced rolling may be biologically important, because it potentially ensures that platelets adhere to disrupted arterial surfaces where platelet hemostasis is most needed. Conversely, it is possible that disorders such as platelet-type and type 2B VWD no longer exhibit flow-enhanced platelet adhesion (Doggett et al., 2002; Doggett, 2003), resulting in pathological platelet agglutination (Sadler, 2005a). Despite intensive investigation, biophysical mechanisms and structural bases of the flow requirement for platelet tethering and rolling on VWF remain unclear. We hypothesize two mechanisms for flow-enhanced platelet adhesion to VWF: transport-dependent acceleration of bond formation and force-dependent deceleration of bond dissociation. An important goal of the present proposal is to elucidate these mechanisms.

1.2.4 Structures of A1–GPIbαN complex

GPIbαN includes an N-terminal sequence (residues 1-35, mauve), eight leucine-rich repeats (residues 36-200, blue), a C-terminal flanking disulfide loop (residues 201-268, brown and green with cyan disulfide bonds), and an anionic peptide sequence (residues 269-282, not resolved) with three tyrosine sulfates (Figure 1-4 A) (Dumas et al., 2004; Varughese et al., 2004). VWF-A1 is a Rossman folding with a central β sheet surrounded by α helices (Figure 1-4 B, cyan) homologues to the I domain and I-like domain of integrins (Emsley et al., 1998).
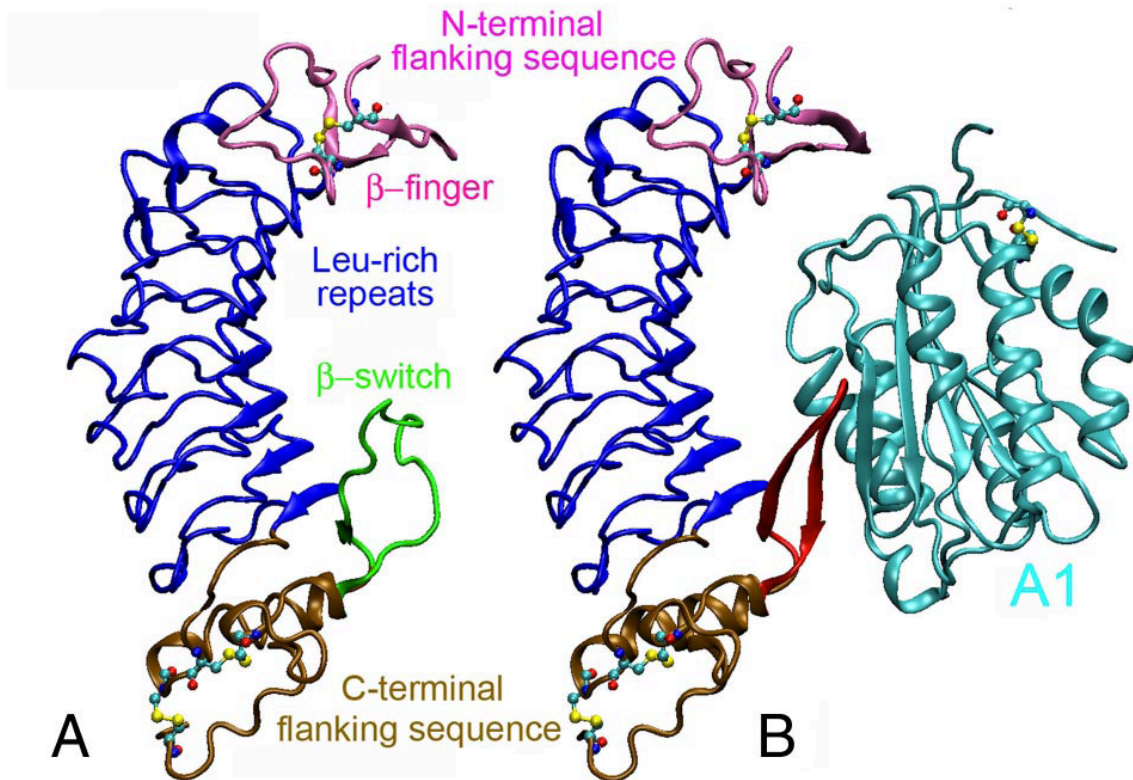
Figure 1-4. Structures of A1–GPIbαN complex. Structures of unliganded GPIbαN (A) (PDB code 1QYY) (Varughese et al., 2004) and GPIbαN in complex with VWF-A1 (cyan) (B) (PDB code 1SQ0) (Dumas et al., 2004). The N-terminal flanking sequence (mauve), leucine-rich repeats (blue), C-terminal flanking sequence (ochre), and cysteine residues (balls and sticks) of the GPIbαN are shown. The loop conformation of the β-switch (residues 227–243) in A is shown in green, and its β-hairpin conformation in B is shown in red. Adapted and modified from (Lou and Zhu, 2008).

15

Several crystal structures of GPIbαN alone (Clemetson and Uff, 2002; Varughese et al., 2004) (Figure 1-4 A) and in complex with A1 (Huizinga et al., 2002; Dumas et al., 2004) (Figure 1-4 B) have been solved. Regions of GPIbαN at each end of the leucine-rich repeats, respectively termed β-finger and β-switch, bind to the top and bottom of the A1 domain, respectively. The sulfated tyrosines do not contact VWF, although mutants of GPIbαN lacking sulfated tyrosines interact much less well with VWF under flow (Dong, 2001). Mutations of GPIbα in other regions also reduce binding affinity to VWF, and transfected cells expressing these mutants roll more rapidly on VWF (Dong et al., 2000; Doggett et al., 2002; Doggett, 2003). Conversely, patients with platelet-type and type 2B VWD have respective mutations in GPIbαN and A1 that enhance binding, which results in spontaneous platelet agglutination (Othman, 2007). Paradoxically, many mutants found to affect VWF–GPIbα binding experimentally are not located at or near the contact interface. For example, VWF-A1 mutations known to cause type 2B VWD, such as R1306Q and I1309V, locate on the opposite side of the A1 molecule from the interface.

CHAPTER 2: MATERIALS AND METHODS

2.1 Proteins

The recombinant WT VWF-A1 monomeric domain (residues 1238-1471, 1238-A1 or mA1) as well as single-residue 2B mutants: R1450E and I1309V; and 2M mutants: V1279I and G1324S were listed in Table 1-1 and described previously (Cruz et al., 2000). A N-terminally-truncated monomeric A1 domain (residues 1261-1471, 1261-A1) was expressed in bacteria and purified as the 1238-A1 protein (Ju et al., 2013b; Tischer et al., 2013). The 1238-A1A2A3 monomeric tridomain (residues 1238-1874) and the N-terminally truncated 1261-A1A2A3 monomeric tridomain (residues 1261-1874) were described (Auton et al., 2012). The recombinant WT dimeric VWF-A1 domain (residues 1208-1496, dA1) was a gift from Dr. Zaverio Ruggeri (Scripps Research Institute, La Jolla, CA) and described previously (Azuma et al., 1991; Mazzucato et al., 2002; Kasirer-Friede et al., 2004). The biotin-labeled polypeptide of VWF 1238-1260 (Lp, QEPGGLVVPPTDAPVSPTTLYVE) and the scramble peptide (Sp, QLPTGVLGEPSDAVPTVYEVTPP) were synthesized (Selleck Chemicals LLC, Huston, TX). All recombinant A domains and peptides were provided by both Drs. Miguel Cruz (Baylor college of Medicine, Huston, TX) and Matthew Auton (Mayo Clinic, Rochester, MN). To acquire dimeric pVWF (dVWF), the sequence encodes for pro-peptide portion was deleted from the VWF cDNA (termed "Δpro-VWF") (Wu et al., 1996). HEK293 cells were transfected with the pMT-Δpro-VWF plasmid to express VWF dimer, which was purified by a heparin column from Dr. Jing-fei Dong's lab.

Plasma VWF (pVWF) was purchased (Calbiochem Inc., San Diego, CA). Glycocalicin (extracellular domain of GPIbα) was cleaved and purified from outdated platelets as previously described (Clemetson et al., 1981; Yago et al., 2008; Ju et al., 2013b). The recombinant fibronectin fragment $FN_{III7-10}$ with a biotin tag at the N terminus was a gift from Dr. Andrés J. García (Georgia Institute of Technology, Atlanta, GA) and was described previously (Petrie et al., 2006). Anti-GPIbα monoclonal antibodies (mAbs): AK2, HIP1, SZ2 (Abcam, Cambridge, MA) and AN51 (Millipore, Billerica, MA) were purchased; WM23 was a gift from Dr. Renhao Li (Emory University, Atlanta, GA). Anti-GPIbβ mAb was purchased (LS-B3174; LifeSpan BioSciences, Seattle, WA). Anti-$\alpha_{IIb}\beta_3$ mAb was purchased (PAC-1; BD Biosciences).

2.2 Red blood cells and platelets

Human red blood cells (RBCs) for BFP experiments were isolated from whole blood of healthy volunteers by finger prick according to protocols approved by the Institutional Review Board (IRB) of Georgia Institute of Technology. RBCs were washed, biotinylated, and stored (up to 2 weeks) for experiments as previously described (Evans et al., 1995; Chen et al., 2008a).

Fresh human platelets for all experiments were isolated from venous whole blood of healthy volunteers by a phlebotomist (Dr. Wilbur Lam lab, Georgia Institute of Technology, GA) according to protocols approved by the IRB. The whole blood of 3 ml (for BFP experiments) or 20~45 ml (for flow chamber assays or acquiring platelet lysate GPIbα) (Evans et al., 1995; Chen et al., 2008a) were collected. Platelet-rich plasma (PRP) was prepared in a 1:10 citrate buffer (170 mM sodium citrate and 83 mM citric acid in distilled water) for the flow chamber assay and in an ACD buffer (6.25 g sodium

citrate, 3.1 g citric acid anhidrous, 3.4 g D-glucose in 250 ml H_2O, pH 6.7) for fBFP assay. In selected platelet adhesion studies to prevent unwanted platelet activation, 2 μM prostaglandin E1 (PGE_1) (Sigma-Aldrich)was added to the citrate buffer (not for the signaling study). The whole blood at this stage can be used directly for the functional assay.

To get washed platelets, the whole blood was centrifuged at 150 g for 15min without brake at room temperature. After the first centrifugation, the PRP was extracted and centrifuged again at 900 g for another 10 min. In selected Ca^{2+} imaging fBFP experiments, 0.5 ml PRP was extracted, incubated with fura-2-AM (Sigma-Aldrich) at 30 μM for 30 min before the second centrifuge. Washed platelet (white pellet) was finally resuspended in the Hepes-Tyrode buffer (134 mM NaCl, 12 mM $NaHCO_3$, 2.9 mM KCl, 0.34 mM sodium phosphate monobasic, 5 mM HEPES, and 5 mM glucose, 1% bovine serium albumin (BSA), pH 7.4) for BFP experiments.

To calibrate the high affinity state of activated platelet integrins, washed platelets were incubated with ADP (Sigma-Aldrich) at 10 μM for 15 min to activate platelets. In selected control studies, $\alpha_{IIb}\beta_3$ antagonist integrilin (eptifibatide) (provided by Dr. Wilbur Lam (Georgia Institute of Technology, Atlanta, GA); COR Pharmaceuticals, Middlesex, NJ) was added to the chamber at 20 μg/ml to inhibit $\alpha_{IIb}\beta_3$ bindings.

2.3 GPIb-IX expressing CHO cell lines (CHOαβ9)

Chinese Hamster Ovary (CHO) cells expressing GPIb-IX (CHOαβ9) as well as a control cell line without expressing GPIbα (termed "CHOβ9") were gifts from Dr. Larry McIntire. The CHOαβ9 cell with the WT and mutant (G233V) of GPIbα were

produced as previously described (Dong et al., 2000). These stable cell lines are excellent (with natural molecular orientation and essential complex composition) for studying the roles of VWF–GPIbα interaction, because these cells do not express all integrin as found in platelets. CHO cells were cultured in α-MEM (Mediatech Inc., Manassas, VA) containing 10% FBS (Hyclone, Logan, UT) and penicillin (5,000 units/mL)/streptomyocin (5,000 μg/mL) (Cellgro, Manassas, VA). The medium for all CHO cell lines was supplemented with the selection agents G418 (400 μg/m) (Invitrogen), methotrexate (80 μM) (Sigma-Aldrich) or Hygromyocin B (400 μg/mL) (Invitrogen). These cells were maintained at an incubator (37°C in 5% CO_2, 95% air).

2.4 GPIbα from Platelet and CHOαβ9 cell lysates

Platelets (2×10^9) or CHOαβ9 (1×10^6) were pelleted and resuspended in a 5 ml of lysis buffer (125 mM NaCl, 50 mM Tris pH 8.0, 1% Triton X) at 4 °C for 30 min with stirring. To avoid the unwanted shedding of GPIbα, the final medium included 5 mM EDTA, 2 mM PMSF and 1× protease inhibitor (#78437; Pierce). After 16,000 g centrifugation at 4 °C for 20 min, the supernatant was collected through a filter (50 K; Millipore, Billerica, MA). These lysates contain the full-length GPIbα, which can be captured to beads for single-molecule experiments.

2.5 Single-bond experiments

2.5.1 *System setup*

The BFP instrumentation is described in detail in chapter 3. In brief, my new BFP system is based on the classic BFP scheme (Figure 2-1, *bottom*) (Evans et al., 1995; Heinrich et al., 2005) and it was built upon a Nikon inverted microscope (TiE) with 40X/0.75 objective lens. The BFP uses swollen biotinylated human RBC as a force

transducer (Figure 2-1, *left*). A probe bead coated with streptavidin and ligand proteins can be glued onto the apex of an aspirated RBC by a micropipette (probe, Figure 2-1, *left*). The adhesion force was determined by multiplying the RBC deformation and the spring constant. The RBC deformation can be regarded as the axial movement of the probe bead tracked by a high-speed camera. The RBC spring constant was estimated by Evans' spring constant model (Evans et al., 1995). The receptor coated bead or cell was aspirated by another micropipette (target, Figure 2-1, *right*). This target micropipette's the steady-and-accurate movement was driven by a computer-controlled piezoelectric translator (PZT).
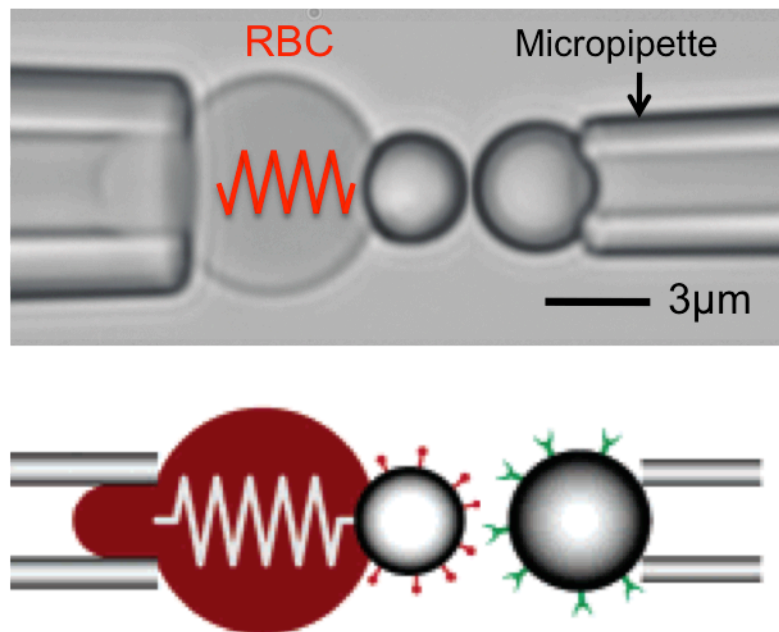
Figure 2-1. The scheme of a biomembrane force probe (BFP). Video-micrograph (*top*) and sketch (*bottom*) depicting a BFP (*left*) and a test receptor-coated bead held in a facing micropipette (*right*). The stationary BFP consists of a swollen micropipette-aspirated RBC and a ligand-bearing (pin-shaped symbols in the sketch) bead (probe) that is chemically glued to the RBC. The receptor-bearing (fork-shaped symbols in the sketch) bead (target) is mounted to a computer-controlled piezo translator opposing the probe. The diameter of the spherical part of the

RBC on the left is ∼6 μm and the diameters of the beads are ~3.5 μm. The sketch was adapted and modified from (Heinrich et al., 2005).

2.5.2 Protein functionalization

All A1s, pVWF, glycocalicin and all kinds of antibodies (i.e. WM23) were pre-coupled covalently with maleimide-PEG3500-N-Hydroxysuccinimide (MW ~3500; JenKem, TX). As previously described (Chen et al., 2008a), modified proteins were mixed with streptavidin (SA)-maleimide (Sigma-Aldrich) in carbonate/bicarbonate buffer (pH 8.5) and then together linked to 3.5-μm (diameter) silanized borosilicate beads (Duke Scientific, Palo Alto, CA) in phosphate buffer (pH 6.8) (Figure 2-2 A and B, *left* and *right* for VWF-A1 and glycocalicin or WM23, respectively). To immobilize full-length GPIbα on surfaces, beads precoated with WM23 were incubated with platelet lysates (see section 2.4) in a rotor for 2-h at room temperature and washed (Figure 2-2B, *right*). After resuspending in phosphate buffered saline (PBS) with 1% BSA, beads were ready for immediate use in BFP experiments. To coat biotin-tagged dVWF, Lp, Sp and $FN_{III7-10}$ on beads, SA alone pre-coupled beads were prepared as above. Subsaturating biotin-tagged protein was coupled to SA beads by a 2-h incubation at room temperature (Figure 2-2B, *right*). After that, the same resuspending steps were used before BFP experiments.
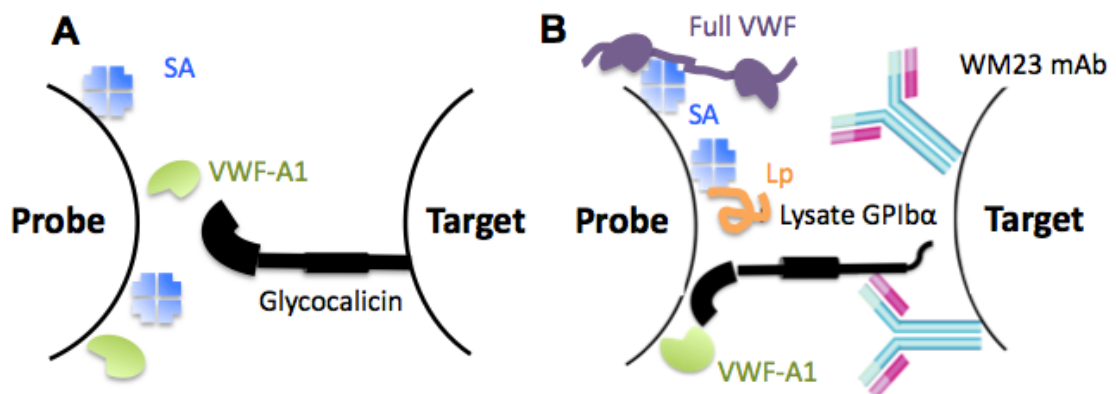
Figure 2-2. BFP functionalization with purified molecules. VWF-A1 was covalently coupled to the probe bead (*left*). Glycocalicin was covalently coupled to the target bead (A, *right*). GPIbα was captured from platelet lysates by antibody WM23 covalently precoated on the target bead (B, *right*). Streptavidin was also covalently coupled to probe beads for attachment to biotinylated RBCs. A1 (green), GPIbα (black), steptavidin (blue), Lp (orange), WM23 (cyan) and pVWF (purple) are depicted.

2.5.3 *Force spectroscopy*

With the in-house built BFP described above, a personal computer installed with custom-written Labview™ (National Instruments) programs were used for PZT control and image analysis, which ran in repeated cycles to measure adhesion frequency as well as bond lifetime under force-clamp and thermal fluctuation. In each cycle, the target was driven to approach and contact the probe with a 20-pN compressive force for a certain contact time (t_c) (0.5-s for glycocalicin, 0.2-s for GPIbα from platelet lysates and for platelet GPIbα and 2-s for platelet fBFP assays) that allowed for bond formation and then retracted for adhesion detection. During the retraction phase, an adhesion event was signified by a tensile force (Figure 2-3 B), but no tensile force was detected in the no-adhesion event (Figure 2-3 A).

For the adhesion frequency assay, adhesion and no-adhesion events were enumerated to calculate an adhesion frequency in 50 repeated cycles for each probe and target (or platelet) pair. Since the adhesion frequency P_a depends on the site densities of receptors (i.e. GPIbα and $\alpha_{IIb}\beta_3$) (m_r) and ligands (i.e. A1 and FNIII$_{7\text{-}10}$) (m_l) on the contact area, in order to compare the binding affinity of Lp to different receptor candidates, the effective affinities were derived via formula $-\ln(1-P_a)/m_r$. Moreover, the adhesion frequency P_a depends on the t_c. To derive 2D kinetic parameters at the force-free condition, P_a was measured at multiple t_c (0.1-5 s). The cellular affinity ($m_r m_l A_c K_a$)

was derived by fitting the P_a vs. t_c curve with the model (Chesla et al., 1998; Huang et al., 2010):

$$P_a = 1 - \exp\{1 - m_r m_l A_c K_a[\,(-k_{off} t_c)]\}, \qquad \text{(Equation 2-1)}$$

at least 3 probe–target pairs were measured at each t_c.

In the force-clamp assay, the target was held at a desired force (0-80 pN were used for all BFP experiments and specific force values 10, 25, 40 and 60 pN were used for fBFP experiments) to wait for bond dissociation and returned to the original position to complete the cycle. Lifetime was measured from the instant when the force reached the desired level to the instant of bond dissociation (Figure 2-3 B, red trace) (Chen et al., 2008a; 2010; 2012). In the thermal fluctuation assay, the target was held at zero force to allow contact with the probe via thermal fluctuation. Bond formation and dissociation were identified from the respective reduction and resumption of the probe bead thermal fluctuations (Figure 2-3 C). Lifetime was measured from the moment of bond formation to the moment of bond dissociation as previously described (Chen et al., 2008a).
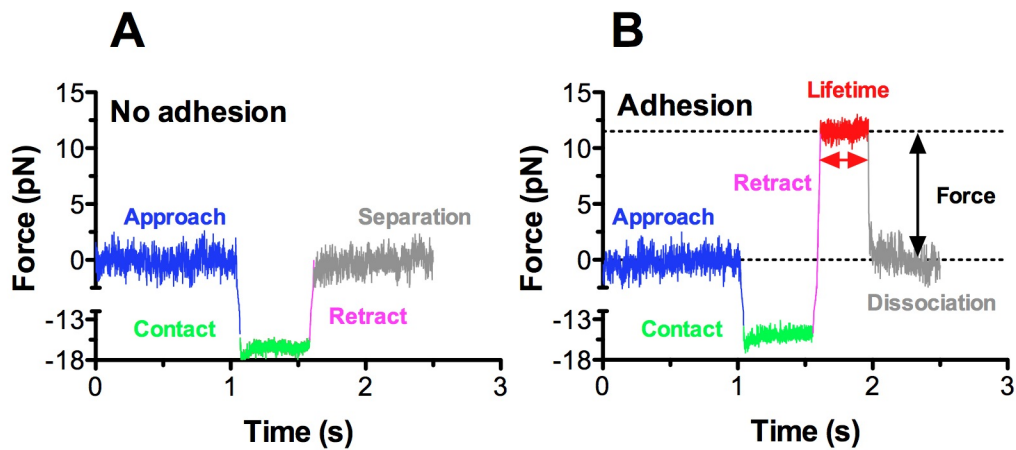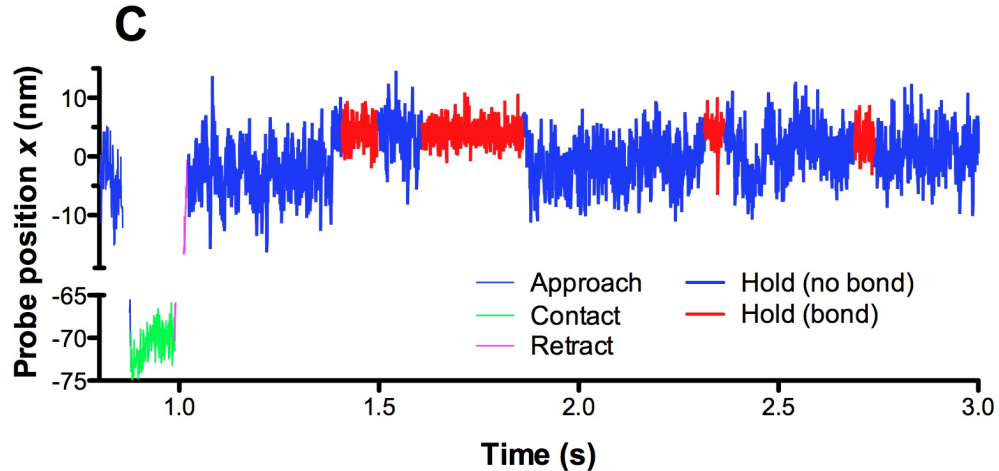
Figure 2-3. Sample raw data of BFP assays. (A and B) Force-clamp assay: force vs. time traces (force spectroscopy) from two representative test cycles. A target bead was driven to approach a probe bead (~0 pN, $t < 1$ s, blue), contacted for certain duration (~15 pN, 1-1.6 s, green), retracted (magenta) and ended the cycle if no adhesion (~0 pN, $t > 1.6$ s, gray) (A) or held at a preset force, termed clamped force, until dissociation if adhesion was detected (~12 pN, 1.6-2 s, indicated in red), after which the target bead was retracted to the starting position (~0 pN, $t > 2$ s) (B). Lifetime was measured from the point when the clamped force (12 pN) was reached (1.6 s) to the point when then bond dissociated (2 s, gray), signified by a force drop to zero. C. Thermal fluctuation assay: probe bead position vs. time traces. Experiment cycle is similar to force-clamp assay, the target bead approaches the probe bead (blue), contact for 0.1 s (green), retract (magenta), and hold (bold blue/red). Representative data points in bound and unbound state are indicated in red and blue, respectively. Bond periods (red) are discriminated as the traces with reduced thermal fluctuation.

"BFP switch assay" was designed to investigate the sequential bindings from dual species of platelet receptors: GPIbα and $\alpha_{IIb}\beta_3$ integrin. In the "switch" experiment, two beads were attached to one RBC: one was coated with a VWF ligand (i.e. A1) for GPIbα, the other was coated with an ligand (i.e. FNIII$_{7-10}$) for $\alpha_{IIb}\beta_3$ (Figure 6-6 A, *upper row*). The first stage of the experiment is the Ca^{2+} triggering assay by engaging a platelet to an VWF ligand-coated probe bead in the force-clamp mode as above (Figures 2-3 and 6-3). After observing the Ca^{2+} mobilization, the RBC was manually rotated to orient the integrin ligand bearing bead against the same triggered platelet. The bead switch was done as quickly as possible (<2 min) so that we could observe the upregulation of

25

integrin binding in time (Figure 6-6 A, *lower row*). The second stage of the experiment after the switch is simply an adhesion frequency assay to derive the binding affinity of the upregulated integrin as above (Figure 6-6 B and D).

2.5.4 *Experiments under 37°C*

This piece of work involves contributions from multiple people: Haiwei Qiu provided the initial idea, I conducted the prototyping and Yunfeng Chen built the current model and made it work.

In order to mimic physiological conditions, especially for platelet signaling study, we developed a temperature control unit to conduct BFP experiment under 37°C. It consists of three modules: a Temperature Controller (PXR3-NAY1-4V0A1; Fuji Electric), a heating circuit and a controlling circuit. For the heating circuit, a conductive ITO-coated coverslip (120Ω) is used to heat chamber area evenly and in compatible with the widefield microscopy. For the controlling circuit, a reed relay is used to link the heating circuit (powered by an 18V DC power supply) and the controller (powered by the conventional 220V AC). A thermocouple (Omega Engineering Inc., Stamford, Connecticut) is used to sense the chamber temperature and wired to the Fuji controller. With the PID loop control by the controller, the temperature of the chamber area will be heated from room temperature (25°C) to the physiological temperature (37°C) gradually and maintained there with a precision of 0.1°C.

To adapt the ITO conductive cover slip, we redesigned the BFP chamber only for 37°C experiment. Like the classic BFP chamber, the new chamber still keeps the "handle bridge" concept, bridging two solid spacers with a handle bar so that two glass cover slips

can be glued on top and bottom of spacers in parallel with a gap distance. For this case, we use ITO cover slip on top and a normal cover slip at bottom. The probe tip of the thermocouple sticks inside the buffer to sense the local temperature. To prevent the electric kill to cells in the chamber, whole chamber material uses acrylic plastics instead of metals.

2.6 Kinetics analysis

2.6.1 *Analyze first-order kinetics from single bond measurements*

Similar to the previously described thermal fluctuation method (Chen et al., 2008a), bond association and dissociation were detected from the abrupt reduction and resumption of thermal fluctuations of the probe beads, respectively (Figure 2-2 C and 5-1 A). The ensemble standard deviation of the horizontal positions, denoted as σ, was employed to quantify the amplitude of thermal fluctuations. Thus, the decrease in σ indicates bond association while the increase in σ indicates bond dissociation, in the view that bond formation equivalently adds more constraint to the motion of probe beads.

We computed the ensemble standard deviation σ by a sliding standard deviation of 90 consecutive data points, σ_{90}, from the *x-t* trajectory and plotted it against *t* (Figure 5-1 D). We chose 90 points by balancing the competing needs between accurate representation of σ value and temporal resolution. Two horizontal lines could therefore be drawn to serve as the thresholds to distinguish bound (solid line in Figure 5-1 D) and unbound (dashed line) states between the opposing beads. The abrupt changes in σ_{90} pinpoint the events of bond formation and dissociation. The period from the instant of dissociation of the existing bond to the instant of formation of the next bond is termed

"waiting time", t_w (Figure 5-1 C), and the period from the instant of bond formation to the instant of bond dissociation is termed "bond lifetime", t_b (Figure 5-1 C).

A pooled collection of waiting times should follow the distribution of the first-order kinetics of irreversible association of single bonds:

$$P_w = 1 - \exp(- k_{on}^c t_w), \qquad \text{(Equation 2-2)}$$

where the cellular on-rate $<k_{on}^c> = m_r m_l <A_c k_{on}>$ is a product of four parameters: A_c is the contact area (considered as a constant for all experiments), m_r and m_l are the respective receptor (i.e. GPIbα) and ligand (i.e. A1) densities measured by flow cytometry (Yago *et al.*, 2004), and k_{on} is the molecular on-rate. P_w is the probability for a bond to form after waiting time t_w. P_w can be estimated by survival frequency as the fraction of events with waiting time $\geq t_w$. Thus, the cellular on-rate can be estimated from the negative slope of the $\ln(1 - P_w)$ vs. t_w plot (Figure 5-2 A).

Similarly, a pooled collection of bond lifetimes should follow the distribution of the first-order kinetics of irreversible dissociation of single bonds:

$$P_b = \exp(- k_{off} t_b), \qquad \text{(Equation 2-4)}$$

P_b is the probability for a bond formed at $t = 0$ to survive at t_b and can be estimated by survival frequency with bond lifetime $\geq t_b$. The negative slope of the $\ln(P_b)$ vs. t_b plot provides an estimate for the off-rate k_{off}.

2.6.2   Analyze lifetime distributions with a two-state model

At each force bin, the survival frequency as a function of bond lifetime t_b was calculated as the fraction of events with lifetime $>t_b$. In our previous study (Yago et al., 2008), 1238-A1–GPIbα bonds were assumed to dissociate from a single state so that the pooled bond lifetimes were analyzed by a single exponential distribution (Equation 2-4) after treating a small fraction (<10%) of long lifetimes (>2 s) as outliers. Taking the log linearizes the right-hand side of Equation 2-4, the semi-log survival frequency vs. bond lifetime plot is predicted to appear linear. The negative slope of the line would be used as an estimate for off-rate k_{off}. However, if long lifetime events were included, the ln(survival frequency) vs. t_b plots were no longer linear (Figure 4-6). To analyze such data, we extended the single-state model to a two-state model that assumes a slow dissociation state coexisting with a fast dissociation state (Chen et al., 2010). The survival frequency data for each force bin were fitted by Equation 2-4, which superimposes two exponential decays.

$$\text{Survival frequency} = \omega_1 \exp(-k_1 t_b) + \omega_2 \exp(-k_2 t_b), \qquad \text{(Equation 2-4)}$$

where k_i and ω_i are off-rate and the associated fraction of the ith state ($i = 1, 2$), which satisfy the constraints $\omega_1 + \omega_2 = 1$ and $k_1 < k_2$, respectively.

2.7 Platelet calcium imaging

With the BFP setup, the A1–GPIbα bond lifetimes were measured in a range of constant forces using a force-clamp assay with a platelet target (Figure 6-1). Concurrently, platelet intracellular Ca^{2+} was measured with fura-2 ratiometric imaging using a fluorescence optical path added to the BFP. The fluorescence BFP (fBFP) instrumentation will be described in details in Chapter 3. Each platelet was tested in repetitive force-clamp cycles for 5 min during which a stochastic sequence of bond

formation/dissociation and the resulting Ca^{2+} flux were recorded. We calculated two groups of kinetic-associated statistics from a timeframe window of a defined length and starting time within each 5-min experimental period and performed correlative analysis with the Ca^{2+} flux.

2.7.1 Ca^{2+} ratio analysis

Fluorescence images recorded by the μManager software (Vale lab, UCSF, CA) from an fBFP experiment were input into a customized imaging analysis Matlab program (The MathWorks) for Ca^{2+} ratio analysis. Due to time-delay-caused misalignment of cell positions from the 340 nm channel and the 380 nm channel, two consecutive images recorded from these two channels at a same preset time point for ratio calculation were firstly aligned. Briefly, the cell was first located and masked in the images of 340/380 channel through a thresholding method (Otsu, 1975). Two masked cells images were aligned using a tracking algorithm with nanometer resolution that is based on cross-correlation analysis of the intensity profiles of these two images (Gelles et al., 1988). After the alignment, a fura-2 ratio was simply calculated via dividing 340 channel intensity by 380 channel intensity pixel by pixel over the whole cell area. The fura-2 ratio of each cell was calculated by averaging fura-2 ratios of all pixels inside that cell. For each individual cell, all 340/380 images over the 5 minutes experimental time were analyzed this way. The peak value of relative ratio increase (in reference with the value at the beginning of the experiment) was taken as the indicator of the Ca^{2+} signal strength.

To correlate bond lifetime with triggered Ca^{2+}, lifetime events were categorized according to the chosen clamp force. The longest lifetime (t_{max}) priori to each successful Ca^{2+} onset was measured. We plotted the percent increase of fura-2 ratio against t_{max} as a

scattergram and analyzed their correlation with linear regression (Figures 6-5 A and B). The goodness-of-fit was accessed with the Pearson coefficient R.

2.8 Measurement of molecular site density

2.8.1 *Fluorescence staining*

To measure the site densities of platelet receptors, fresh platelets were incubated with PE-conjugated anti-human GPIbα mAb (AK2 or HIP1; Abcam, Cambridge, MA) for GPIbα; FITC-conjugated anti-β_3 mAb (HIP8; BD Biosciences) for the total of $\alpha_{IIb}\beta_3$; a FITC-conjugated anti-$\alpha_{IIb}\beta_3$ mAb (PAC-1; BD Biosciences) for the activated fraction of $\alpha_{IIb}\beta_3$ at 10 μg/ml each in the PBS at room temperature for 30 minutes. To measure the site densities of ligands, probe beads were stained with anti-A1 mAb (5D2 or 6G1, gifts from Dr. Michael Berndt (Curtin University, Bentley, Australia)) for all VWF ligands (WT and all mutant mA1, dA1 and VWF) and anti-FN mAb (HFN7.1; Abcam, Cambridge, MA) for $FN_{III7-10}$ as above. Then the beads were stained with a PE-conjugated secondary Ab (Abcam, Cambridge, MA) with the similar procedure. For an isotype control, irrelevant mouse IgG1 (eBiosciences, San Diego, CA) was used.

2.8.2 *Data acquisition*

Site densities of samples were acquired by a BD LSR flowcytometer with FACS DiVa 3.1 software (BD Biosciences). Before running samples, standard beads were prepared and run through firstly for quantification of MESF (molecules of equivalent soluble fluorophore). To obtain the mean intensities of calibrated microbeads with four different molecular site densities, four gates were created to gate on the histogram plot of fluorescene intensities vs. # of events (Figure 2-4). After completing the calibration procedure, the samples were run through the flow cytometer to measure the mean values

of fluorescence (geometric mean). Generally, 5,000 events per sample were recorded. The gating, calculating the means and plotting were done with the FlowJo software (Tree Star, OR).

2.8.3   *Site density determination*

To determine the site densities of samples, the measured fluorescence intensities were compared to standard calibration beads (BD QuantibriteTM PE Beads, BD Biosciences). The recorded four intensities of fluorescence of calibration beads were plotted as a function of numbers of PE fluorofore from BD biosciences. Linear fitting this plot generated the value of the slope, which was used to calculate the numbers of the molecules on samples. The sample site density was derived from interpolating the sample's measured intensity into a linear equation, which was fitted from calibration bead results (Figure 2-4). The natural log plot was used to derive parameters for linear fitting according to the BD manufacturer's instruction (Figure 2-5). The # per bead was converted into the physical site density ($\#/\mu m^2$) by dividing with the estimated bead or cell surface area (μm^2) (Yago et al., 2004). The cell or bead surface area was estimated from platelets and beads geometry (The diameter for an aspired platelet is ~1.5 μm and that for a bead is ~ 3.5μm).
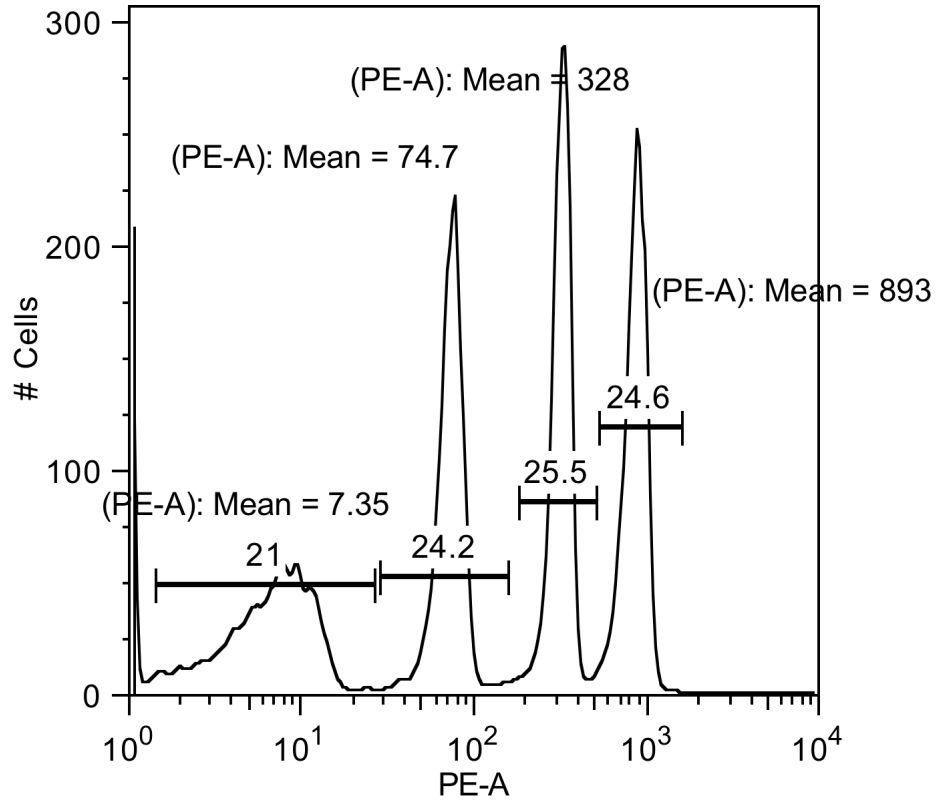
Figure 2-4. Sample flow cytometry data. The data was acquired from using BD QuantibriteTM PE Beads. The FACS laser was set to PE channel. The PE intensity histogram was plotted. 4 different populations (4 peaks) were identified with percentage of each. The geometric mean for each populations was calculated and indicated. The data was analyzed using the FlowJo software.
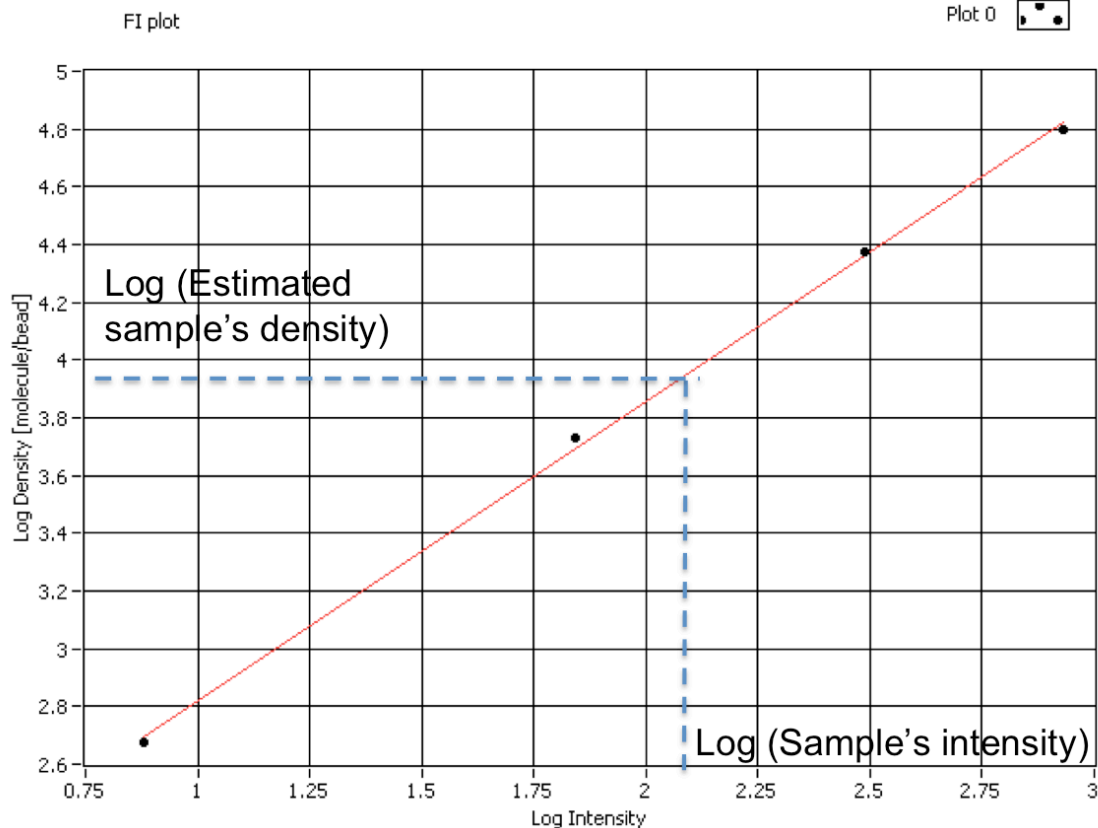
Figure 2-5. Site density calculation from fitting with calibration bead results. The density-intensity relation was fitted into a line with the four calibration bead populations (dots). The natural log of sample's intensity (geometric mean) was interpolated with the fitted line and derived the estimated sample's density (#/bead). The fitting and site density calculation was pipelined into a Labview program.

2.9 Parallel flow chamber assays

A parallel plate flow chambers is a classic in vitro method for studying platelet adhesion under the influence of laminar fluid shear stress (Savage et al., 1996; 1998; Doggett et al., 2002; Mazzucato et al., 2002; Kumar et al., 2003; Ruggeri et al., 2006; Yago et al., 2008; Coburn et al., 2011). In my study, I used the flow chamber as a complementary approach to corroborate single-molecule results and considered this as a functional study for the biological significance. In flow chamber experiments, different

VWF constructs are coated on non-treated plastic petri dishes (#430588; Corning) by physical absorption. The reason I used the non-treated dishes over treated ones is because the former allow much stronger physical absorption than the later so that protein coating is more resistant against the shear flow. Platelets and CHOαβ9cells are typically perfused through a parallel plate flow chamber (Glycotech, Gaithersburg, MD) over the VWF coated surface. In these experiments, measurements included rolling velocities, tether pause times and tether rate.

Our in-house flow chamber setup was a revised based on the one used in McEver lab. Dr. Tadayuki Yago trained me on mastering this technique when I was visiting Oklahoma Medican Research Foundatoin (OMRF) in 2011. Platelet tetherings were visualized using an inverted-stage phase-contrast microscope (DIAPHOT-TMD) with either 20x (for platelet) or 10x (for CHOαβ9) phase objective (Nikon). The magnification calibration has to be carefully done with a micro-ruler (purchased from Amazon.com). Images were captured at 30 fps directly to a computer using a video microscopy camera (Photometrics, Tucson, AZ).

Images were analyzed post-experiment using the NIS-Elements software (Nikon). The slow-speed playback was used to carefully track to discriminate platelet status such as transiently tethered, rolling and firmly attached. For this analysis, the position for each frame was determined during data collection when cells were tracked. This position was used directly to determine velocity for each frame as distance per time. For rolling parameter analysis, position and time data for each frame were used as inputs into the stop-go model described previously (Yago et al., 2004; 2008).

2.9.1   *Rolling velocity*

Rolling velocity assay can complement the bond lifetime data by single-molecule measurements (Yago et al., 2004; 2008; Ju et al., 2013b). The basis for this argument is a causal relationship between the bond lifetime of an interaction and the cell rolling velocity mediated by the interaction (Zhu et al., 2008; Ju et al., 2013b), i.e., the shorter the lifetimes, the faster the rolling velocity. In this assay, platelets were perfused at various wall shear stresses over VWF-A1 or other ligand proteins (coated at 50 μg/ml) in a parallel-plate flow chamber. Mean rolling velocities were measured over a 0.1s interval by video microscopy with frame-by-frame analysis by Nikon NIS Elements software as previously described method (Yago et al., 2008). At each wall shear stress, approximately 20 events of platelets rolling were measured and averaged. Data are presented as mean ± S.E.M.

2.9.2   *Tether pause time*

Pause time analysis is also used to complement bond lifetime results and determine off-rates. When the ligand coating density is controlled as a low level (<2μg/ml), these techniques can be used to approximate the single-molecule kinetics (Yago et al., 2004; 2008). A transiently tethered platelet was identified when stop time > 0.1s and it could move or travel a total distance afterwards. A pause time was determined by the amount of time a platelet stayed around the same position within the noise. Pause times for all platelet tracks are reported as the mean ± S.E.M for approximately 20 events of platelets transiently tethered.

2.9.3   *Tether rate*

Tether rate assay is designed to complement the waiting time data by single-molecule measurements that can relate with the on-rate kinetics (Yago et al., 2007). The

flow chamber setup and the protein coating are the same. The only thing distinct for this assay is we look at the freshly tethered platelets within the field of view and certain time range. The freshly-tethered refer to those events of freely-flowing platelets that tethered to VWF-A1 for the first time, excluding those that roll in. As long as a platelet tethers, we count, regardless of its status afterwards, such as activated, firmly attached and flow-away. Tethering events were identified by observing the sudden stops directly from the videos played back in slow motion (30 fps). The tether rate was calculated by normalizing the number of observed tethering events in 1 min by the total number of cells delivered to the field of view in the same focal plane (the bottom surface) in the same period of time.

2.9.4 *Whole blood functional assay*

45 ml Whole blood was collected from healthy donors and mixed with 5 ml citrate buffer for anti-coagulation (see section 2.2). As described previously (Cruz et al., 2005; Martin et al., 2007), citrated whole blood mixed with 0.5 mM of Lp or Sp was perfused in the parallel plate flow chamber at a fixed shear rate (i.e. arterial flow rate 1,500 s^{-1}) over the chamber floor coated with collagen (100 µg/ml) or VWF (100 µg/ml) by physical absorption. After a 2-min perfusion, the surface was washed with PBS, and several frames of attached platelets were recorded. Tethered platelets were observed with a phase contrast objective (40x) and snapshoted by video microscopy.

2.10 Direct binding assay by ELISA

This assay was performed as described previously (Auton et al., 2010a; 2012). Microtiter wells were coated with GPIbα from platelet lysates, A1 or A2. Biotin-labeled Lp or Sp peptides (0.5 mM) were incubated with receptors-coated wells for 1 h at 37°C.

After washing, these wells were incubated with neutravidin-horseradish peroxidase conjugate (1:200; Pierce) 1 h at 37°C. The wells were again washed, and the substrate (o-phenylenediamine; Sigma-Aldrich) was added. The reaction was stopped with 0.025 ml of 2 N H_2SO_4, and the plates were read at 490 nm absorbance. Net binding was determined by subtracting absorbance values from wells added only BSA from the total bindings. The isotype control VWF-A2 in this assay has been described previously (Martin et al., 2007).

2.11   Statistical testing

All data for group comparisons in this study were analyzed by two-tailed Students' t-test (analyzed with GraphPad Prism). They are deemed significant for p values below 0.05. All correlative analyses were evaluated with Pearson correlation coefficient (or Pearson's R), which is a measure of linear dependence between two variables (Ca^{2+} and kinetic statistics in this study). R squared (R^2) is the widely used coefficient of determination in linear regression.

CHAPTER 3: BUILD A BIOMEMBRANE FORCE PROBE (BFP)

3.1 Introduction

Since Dr. Evans et al. pioneered the biomembrane force probe (BFP) technique in 1995 (Evans et al., 1995), this single-molecule tool has been well developed in our lab to measure the interactions of proteins immobilized on surfaces. It was used to analyze two-dimensional kinetics of adhesion molecules interacting with their ligands (Chen et al., 2008a; Sun et al., 2009; Chen et al., 2010; Huang et al., 2010), to measure molecular elasticity (Chen et al., 2012) and to determine protein conformational changes (Chen et al., 2012). Compared with other single-molecule techniques such as optical tweezers (OT) (Molloy et al., 1995; Mehta et al., 1997; Veigel et al., 1999; Sun et al., 2009) and atomic force microscope (AFM) (Marshall et al., 2006; Sarangapani et al., 2011) that are commercially available in many laboratories, the BFP is very unique as it uses a red blood cell aspirated by micropipette as a very soft force transducer. Thanks to the RBC's soft stiffness, the BFP can probe very weak biomolecular interactions with the pico-newton (pN,10^{-12} Newton) force resolution. In addition, the new system that I built for this thesis (2nd generation BFP) can probe molecular distance change with sub-nano (nm, 10^{-9} meter) spatial resolution and sub-millisecond (ms, 10^{-3} second) temporal resolution due to the new design of microscopy, optics hardware and tracking algorithm. All above in this new BFP system enables us to investigate mechanical regulation of platelet adhesion with better details on cellular and molecular levels.

3.2 The second generation BFP system (BFP-2)

Based on Dr. (Jack) Wei Chen's design of the 1st generation BFP in the lab, I built a 2nd generation BFP system, called BFP-2. It consisted of a hardware system (optical, mechanical and electrical components) and a software system developed with Labview. The optical system provides excellent imaging of a magnified sample target i.e. a platelet (by ~200X). The mechanical hardware system provides steadily manipulation of the targets with holding micropipettes. The electrical system was the most important part of the BFP. It consists of one high speed camera for tracking probe bead's position in real time, one normal speed camera for measuring required dimensions and monitoring experiment chamber conditions, four piezos and their controllers, and two fast computers that run control program. Software program mainly analyzes the grabbed images from the high speed camera, store and analyze the data, and feedback control the piezo movement.

3.2.1   *The hardware system*

Like the old BFP, the hardware system of the BFP-2 consisted of optical, mechanical and electrical components (Figure 3-1). Optical components were based on an inverted microscope (TiE; Nikon) with a numerical aperture (NA) 0.85 condenser with a top lens and 40X objective lens (NA 0.75 WD 0.72mm for dry lens and NA 1.30 WD 0.20mm for oil lens). The reason to use such a high NA condenser is to better focus illumination light to show clear bead diffraction pattern. Two video tubes were used to mount high-speed camera (GE680; Prosilica, Newburyport, MA) and normal speed camera (GC1290; Prosilica, Newburyport, MA) onto the camera ports on the microscope and provided 4X and 2.5X magnifications respectively. The magnifications of these two

video tubes were from the combination of a 0.25X tube lens with 15X eyepieces. The light source was a mercury lamp with a focus tunable lamphouse (HMX-4; Nikon), which can show a clear diffraction pattern of a glass bead and provides strong light and for high-speed camera's grabbing. Due to the protection for human eyes and camera CCD, different neutral density filters (45mm ND 8 or 16 A) were placed on the light path from the lamp to the camera to reduce the brightness. To keep the glass bead edge sharp, a diffuser was also used. To reduce chromatic abbreviation of RBC, a green light filter (560nm±20nm) was mounted on the top of the condenser.
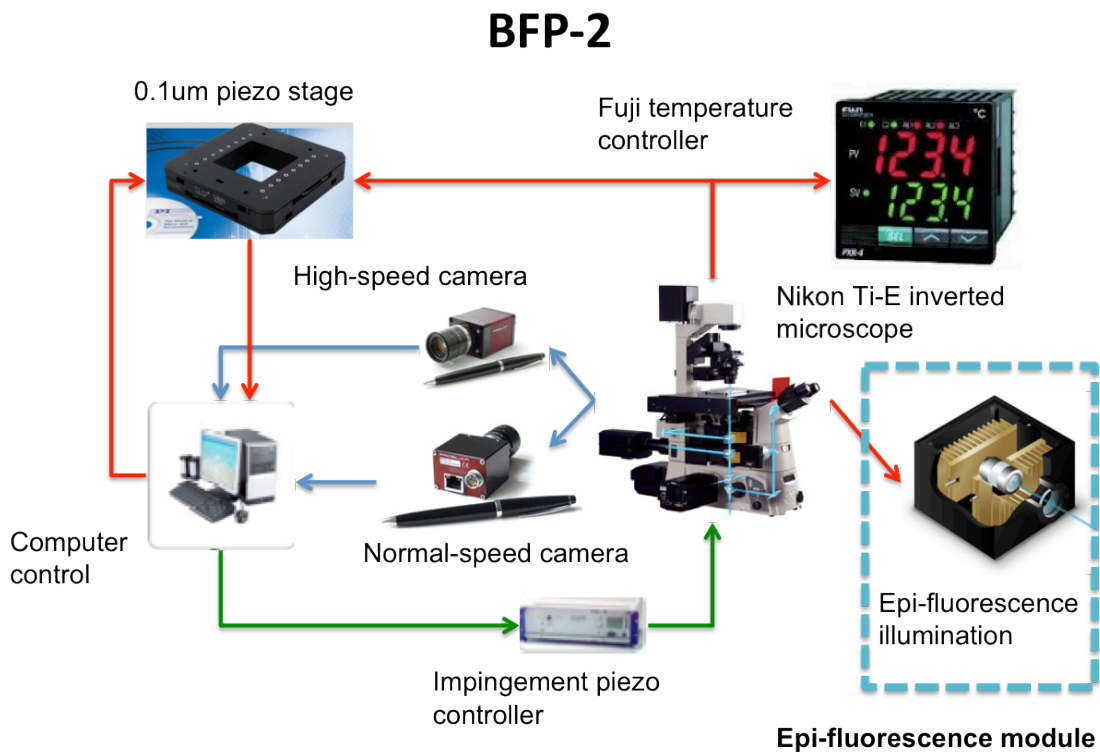
Figure 3-1. The scheme of BFP-2 instrumentation

The mechanical system included several components: 1) an air anti-vibration table (#77049089, 5' x 3'; TMC, Peabody, MA) the whole microscope and isolating the mechanical vibrations from the environment (Figure 3-2 A); 2) two 3D X-Y-Z mechanical stages holding and positioning micropipettes (Figure 3-2 B and E). The 3D stage on the left side (probe) only use micrometers to position the micropipette coarsely (462-XYZ-M, Newport, CA), but the other one could adjust the right pipette (target)'s positions finely with three piezos of nanometer precision (M-105.3P, PI, Germany) (Figure 3-2 A). The assembly of 3 piezos together uses a home made adapter; 3) a one-dimension freedom piezo stage (P-753.1CD; Physik Instrumente) with capacitive feedback control and sub nanometer precision, driving the target pipette to move along the axial direction; 4) a hydraulic micromanipulator with a remote fine control to position the probe bead onto the apex of the red cell (PH400, Karl Suss, Germany); 5) a customized microscope steel stage, built with steal so that this stage was heavy enough to reduce the mechanical noise (vibration) transmission to the chamber in which the experiment runs; 6) a programmable piezo stage mounted on top of the microscope stage that provides the movement freedom in X and Y axes with nanometer precision (M-686.XYD, Physik Instrumente). The control of this piezo stage is hooked up with a gaming joystick for experimental convenience. The fine controllable movement by this stage provides an easy hand to manipulate a single platelet in an experiment chamber; 7) three customized sets of manometers for micropipette aspiration and pressure control. The one connecting to the probe pipette has a pressure sensor to accurately measure and indicated the pressure difference to determine the RBC's spring constant.

The electrical system consisted of an imaging grabbing module and a piezo control module. The imaging grabbing module was composed of a high-speed camera (~2000 fps, GE680; Prosilica, Germany) for tracking the probe bead position and a normal speed camera (GC1290; Prosilica Germany) for measuring the dimension and monitoring the experiments process. Both cameras' images were transmitted via ethernet cables (Figure 3-2 A and F). The images from each camera were processed by an adapter card (pro 1000; Intel) installed in a PC respectively. The frame grabber for the high-speed camera was much more powerful than the one for the normal-speed camera, since it had to handle much large amount of image data. The piezo control module included piezo stages, controllers. The piezo controller amplifies the signal and output voltage signals (0-100V) to control the PZT's steady movement. The output signals were transferred via controllers to the computers (RS-232).
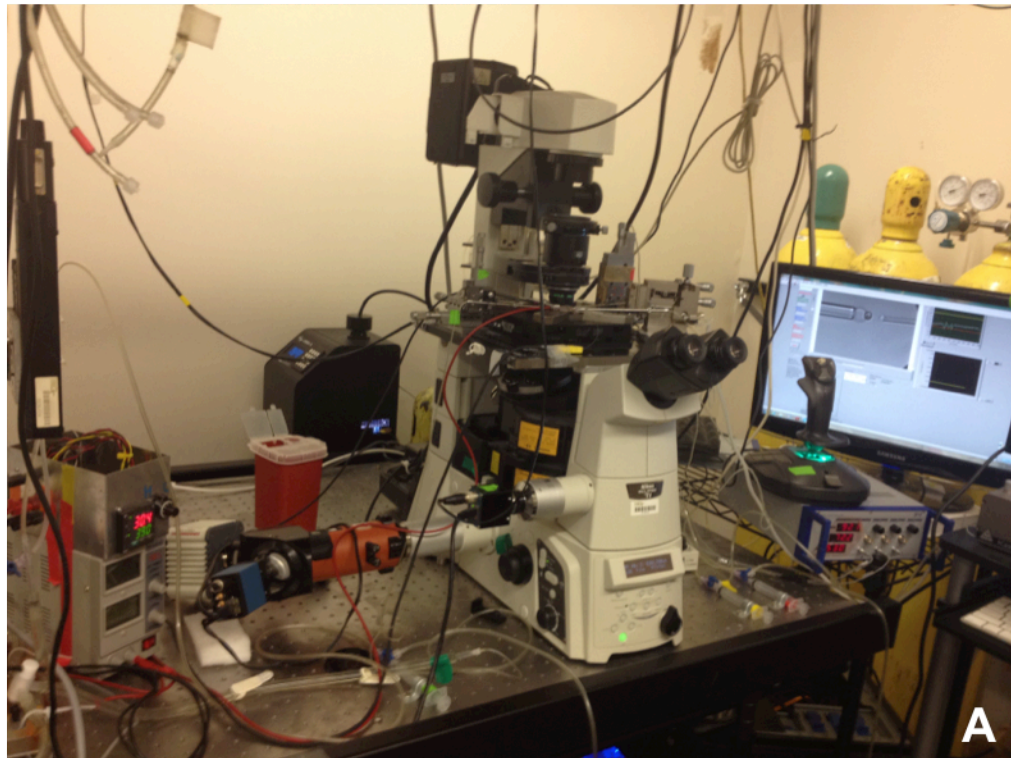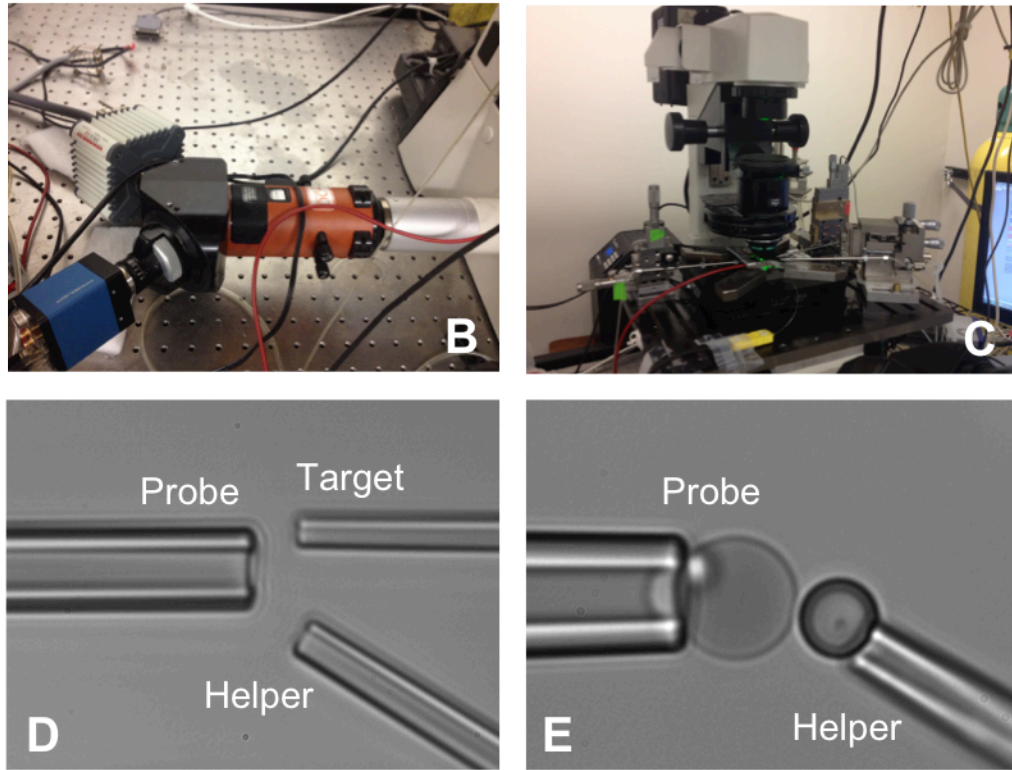
Figure 3-2. Photographs of BFP-2 assembly. (A) Nikon TiE inverted microscope with optical components enabling wide field microscopy and epifluorescence microscopy. This microscope can also be connected to an imaging splitter (DC2). (B) A dual-cam system called "DC2" (orange) onto which the high-speed camera (blue) and a fluorescence camera (white) were mounted. (C) Home build microscope stage that adapts an experiment chamber and three micropipette manipulation sets. (D and E) Micrographs of BFP setting in an experimental chamber. (D) Micropipettes assembly: probe pipette (*left*), target pipette (*upper right*) and helper pipette (*lower right*). (E) Probe bead placement. A probe bead was manipulated by a helper pipette and attached to a RBC apex as a force probe. Note: For better visualization of the BFP-2 assembly, the microscope-heating unit and manometers have been omitted from these photographs.

3.2.2   *The software system*

The software system for the BFP consisted of an experiment module and a post-experiment data analysis module. The experiment module mainly handles image acquisition from the high-speed camera and pre-processes BFP status, such as extracting the position information of the edge between the probe beads and RBC as shown in (Figure 3-3) from grabbed images for post-experiment analysis. The data analysis module

44

was used to analyze the molecular interaction, i.e. bond lifetime, kinetics, from the extracted data.

In the experiment module, the home-made BFP-2 Labview program pinpoints the relative probe bead position by edge detection, which has been described as the line-tracking algorithm used in old BFP system (Chen, 2009). In brief, the line-tracking algorithm allows the computer to automatically detect the darkest point over a glass bead diffraction pattern (Figure 3-3). In experiment, a tracker line (green, Figure 3-3, *upper panel*) is manually drawn to provide a region of interest to the program. I further improved the algorithm with a smart ROI selection function, whicn means the system will automatically expand the ROI (width of 30 pixels x length of the tracker line, red area in Figure 3-3, *upper panel*) around the tracker line to speed up the process of the image acquisition and increase the frame rates. The ROI of 30 pixels in width (y-axis, Figure 3-3) will be analyzed by binning into one line of 1 pixel, the intensities along this line are averaged and plotted (Figure 3-3, *lower panel*). To obtain the edge position, the intensity profile is fit by Gaussian distribution. The peak of fitting curve provides the *x*-position of the edge (Figure 3-3, *lower panel*), which is considered as the relative position of the probe bead. To determine the spring constant of the BFP, the radius of probe pipette, RBC and contact area were measured by the software program customizedly written by Labview. The tracking data were stored in the hard disk during the experiment. Next, all the stored data were analyzed by the data analysis program that is customizedly written with Labview 2009.
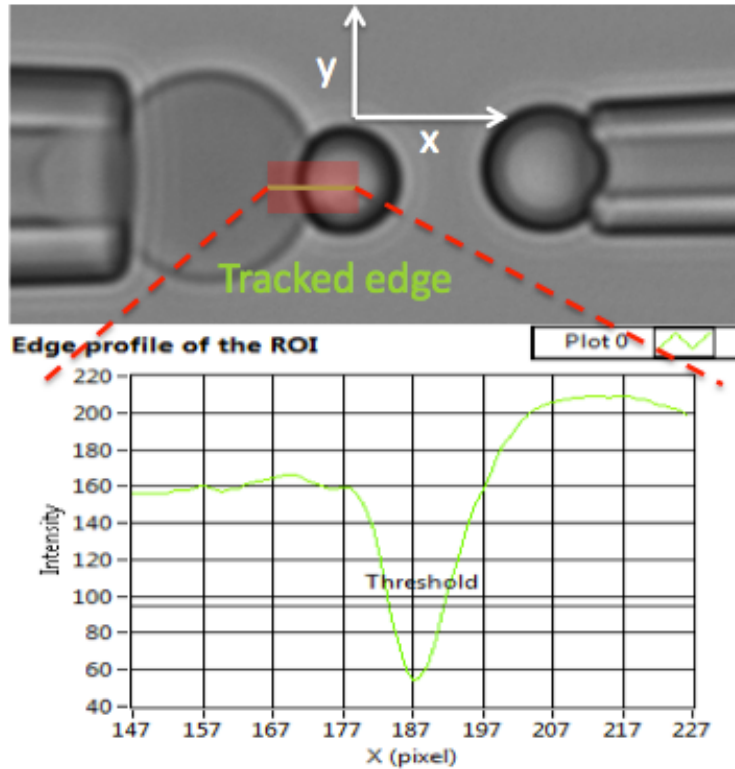
Figure 3-3. Imaging tracking region and intensity profile for the BFP. The upper panel shows the BFP photograph. The smart region of interest (ROI) for position tracking is indicated in red, while the rest area is blocked out not for image acquisition and analysis. The line edge tracker, indicated in green, is manually drawn before starting the experiment. The lower panel shows the intensity profile of the bead's edge in the upper panel. The *x*-region corresponds to the *x*-direction length of ROI while intensity corresponds to the average of *y*-intensity by binning of 30 pixels in width. The intensity curve is fitted by Gaussian distribution to determine the peak position in *x*-axis.

3.3 BFP experiment procedures

The BFP experiment preparation consists three steps: 1) Assembly three micropipette in the microscopic filed of view; 2) Stick the bead to the RBC probe with the helper pipette; 3) Grab the target bead. Here in my thesis, I used three different types of targets: GPIbα coated bead, CHOαβ9 and platelet. After the probe and target are aligned, we will measure the spring constant of the BFP, which is estimated by Evans's model(Evans et al., 1995):

$$\kappa = \frac{\pi R_{\mathrm{p}} \Delta p}{(1 - R_{\mathrm{p}}/R_{0})\ln[4R_{0}^{2}/(R_{\mathrm{p}}R_{\mathrm{c}})]},$$ Equation 3-1

where the spring constant κ depends on radii of the probe pipette (R_p), RBC (R_0) and the

contact area (R_c) between the probe bead and the RBC and pressure difference aspired at

probe pipette tip (Δp). Based on Hooke's law, a binding force, F, can be quantified by the

product of spring constant and displacement of the probe bead (Δd), i.e., $F = \kappa \times \Delta d$

(Figure 3-4). Since the we can adjust κ from 0.1 pN/nm~1 pN/nm, BFP can probe a very

wide range of force from 1 pN to 1000 pN as well as a very wide range of force loading

rates from 10 pN/s to 10^4 pN/s. These two force-related features are very useful to study

various receptor-ligand interactions, κ is set as 0.25~0.3 pN/nm for force-clamp assays on

the A1-GPIbα system. Moreover, with an even lower κ, i.e. 0.15 pN/nm, we can utilize

BFP's thermal fluctuation to study molecular association and dissociation and to measure

the kinetic parameters at zero force (see Chapter 5). As the amplitude of the fluctuation

reduces much more than stiffer sensor, such as AFM, the BFP is more competent to

detect molecular bond formation in thermal fluctuation.

Get edge reference
at time zero

Probe bead

κ

Probe pipette

Target pipette

RBC intact

Target bead

Δd Edge 1 for tracking

RBC under deformation
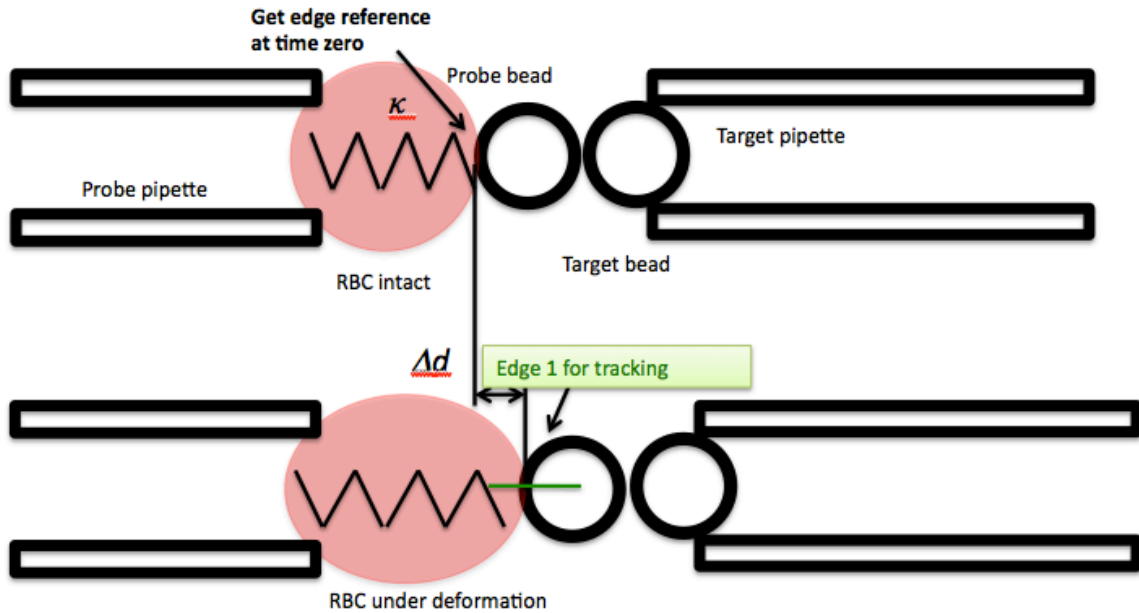
Figure 3-4. The rationale of BFP force calculation. The upper panel shows the BFP at time zero. The probe is not in contact with the target. The RBC is force-free. The lower panel shows the force-clamp phase of a BFP experiment. The pulling force is applied through the receptor-ligand bond so that the RBC is deformed by Δd, which is measured by tracking the position change of the probe bead (green line). The pulling force is calculated as the multiple of RBC spring constant κ and RBC deformation Δd.

Basically for all BFP experiment, the following testing cycles will be run: the target bead will be brought to approach to and then contact with the probe bead by the program-controlled piezo actuator. The contact will be signified by the impingement of the RBC. The computer will control the compressive force and contact duration. At the end of the contact duration, the piezo actuator will retract the target away from the probe to a preset position in terms of clamp force or separation distance. The computer with feedback control will clamp this position until the bond dissociates. An axial deformation of the RBC toward the target will signify an adhesion. The high-speed camera with the real-time-tracking program will detect this deformation. In the absence of an adhesion (Figure 2-3 A), this retract of the target does not generate a binding force on the

molecular bond. While in the presence of an adhesion (Figure 2-3 B), the clamped force will be exerted on single molecular bond. The bond lifetime measurement will be recorded from the moment of the stop of the retraction to the moment of the target dissociates from the probe. This approach-push-retract-hold-return test cycle (Figure 3-5) will be repeated many times to acquire an ensemble of data for statistical analysis (Chen et al., 2008a).
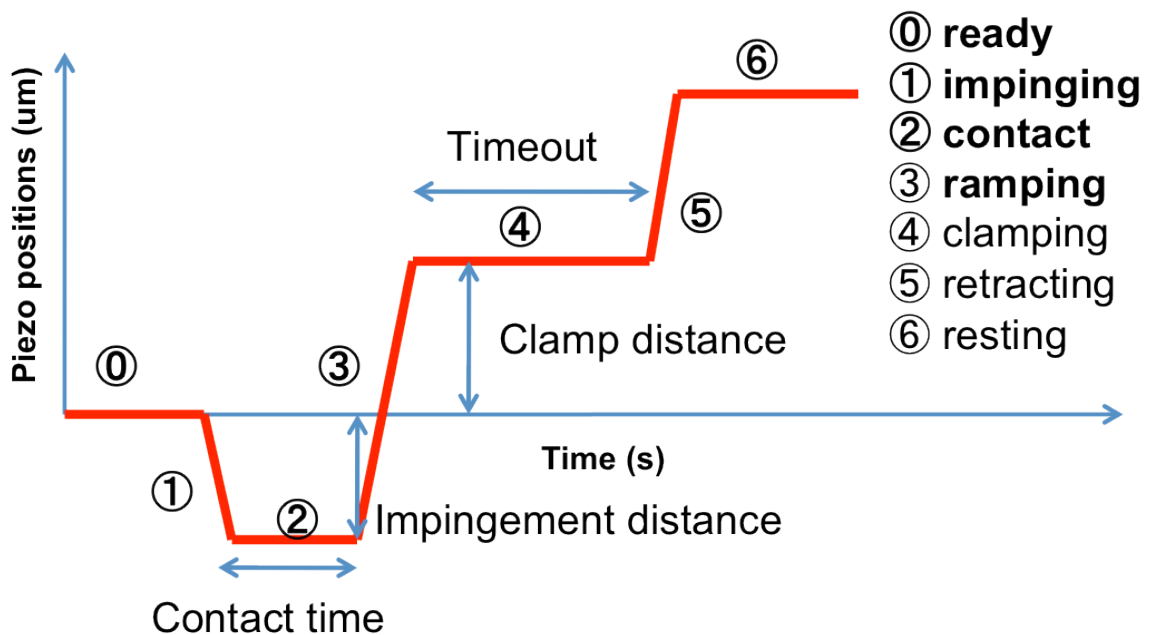
Figure 3-5. The BFP-2 test cycle. The approach-push-retract-hold-return test cycle driven by piezo.

3.4 Fluorescence BFP (fBFP)

This piece of work involves collaborations with other lab members: Jin-sung Hong provided the initial light path design, Jack Wei Chen and Baoyu Liu pioneered the fBFP experiments on studying T-cell calcium triggering and data analysis and Qinghua Ji manufactured the experiment chamber for fBFP.
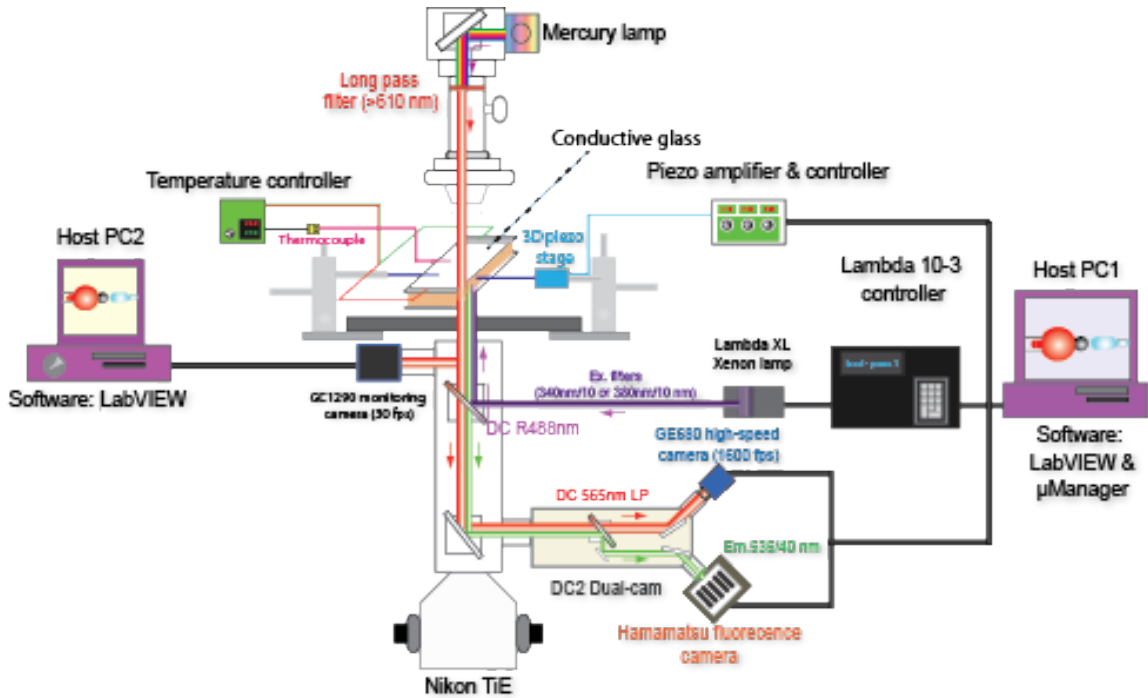
Figure 3-6. Schematic of home-built fluorescence biomembrane force probe (fBFP). The fBFP was built to enable simultaneous *in situ* measurement of single-bond kinetics and the Ca^{2+} signaling triggered by the controlled VWF–GPIbα interaction on a platelet. The fBFP is the upgraded based on the BFP-2 (see 3.1). A Photometrics DC2 Dual-cam system separates the light paths for simultaneously tracking the probe bead position by red light (>605 nm) and Ca^{2+} signal by green (510 nm) fluorescence. To record the ratiometric image from the platelet, excitation lights (purple pathway, 340 and 380 nm filters) from a Xenon lamp are guided to the sample via a dichroic mirror (DC R488 nm) that reflects the light with wavelengths <488 nm. The emission lights (green and red pathways) are both guided into the DC2 Dual-cam system. Another dichroic mirror (DC 565 LP) passes lights with wavelengths >565 nm to the high-speed camera but reflects those with wavelengths <565 nm into the fluorescence camera. The Lambda XL lamp controller and fluorescence camera are controlled by µManager software. The initial design was contributed by Jin-sung Hong and further customized by Jack Wei Chen and Baoyu Liu. The illustration was drawn by Yunfeng Chen.

To simultaneously record the fluorescent images (i.e. fluorescence from fura-2 dye) while tracking the bead position from the widefield view, light path was redesigned to integrate the epi-fluorescence imaging together with widefield microscopy on one microscope (Figure 3-6). Firstly, a fluorescent excitation light source (Xenon lamp, Lambda XL, Sutter Instrument) was added. To get the ratiometric fura-2 imaging, light

excitations of two wavelengths, 340 nm and 380 nm, were alternated via shutter control and a filter wheel in the light source. Secondly, a Dual-cam system (DC2, Photometrics, AZ) was used to adapt a fluorescence camera (ORCA, Hamamatsu, NJ) for fluorescence together with the high-speed camera used for normal BFP (Figure 3-2A and C). Thirdly, emitted lights whose wavelength was longer than 605nm was guided to the high-speed camera and that shorter than 605nm to the fluorescence camera following two steps: 1) a red filter (high pass 605nm, Chroma Technology, VT) was added in front of the bright field light source (mercury lamp) on the top of the microscope; 2) a dichroic mirror (DC R488 nm) was put in a filter wheel of the microscope to reflect the excitation light with wavelength shorter than 488nm to the sample and to pass through all lights with wavelength longer than 488nm from the sample to another dichroic mirror inside of the Dual-cam system (Figure 3-6). The dichroic mirror (DC 565 LP) inside the DC2 Dual-cam system splits the light so that the light of wavelength longer than 565 nm to the high-speed camera and that shorter than 565 nm to the fluorescence camera respectively (Figure 3-6). Our customized Labview program controls the high-speed camera (see section 3.2.2 and Figure 3-2 A), while μManager controls the fluorescence camera. The μManager also controls all light source shutters and the filter wheels that hold two excitation filters (340nm ± 10nm and 380nm ± 10nm) inside the light source (Lambda XL; Sutter Instrument) for fura-2 ratiometric imaging.

CHAPTER 4: THE INTERPLAY OF FORCE AND THE A1 DOMAIN N-TERMINAL FLANKING REGION ON REGULATING THE VWF– GPIB-ALPHA CATCH BOND

4.1 Introduction

During the early stage of hemostatic and thrombotic processes, platelets tether to and translocate or roll on von Willebrand factor (VWF) immobilized on disrupted subendothelium. This adhesive interaction is primarily mediated by the binding of the 45 kDa N-terminal domain of the α subunit of the platelet glycoprotein (GP) Ib-IX-V complex (GPIbα) to the A1 domain of VWF (Ruggeri, 2003; Andrews and Berndt, 2004; Ruggeri and Mendolicchio, 2007). This VWF–GPIbα interaction needs to be delicately balanced because insufficient adhesion may not achieve hemostasis while excessive adhesion may result in thrombosis (Lenting et al., 2010). Since such binding occurs under arterial blood flow, the VWF–GPIbα interaction is regulated by rheological force (Mazzucato et al., 2007; Yago et al., 2008; Jackson et al., 2009). Circulating platelets do not bind to VWF unless putative conformational changes occur around its A1 domain (VWF activation) as a result of exposing to high hydrodynamic forces (Shankaran et al., 2003). Recent findings on the force-dependent VWF activation mechanism can be summarized into two steps: 1) the breakdown of the auto-inhibitory mechanism involving interdomain associations within A1A2A3 tri-domain (Martin et al., 2007; Auton et al., 2010a) and between A1 and D'D3 domains (Ulrichts et al., 2006) and 2) the regulation of A1 binding affinity to platelet GPIbα (Yago et al., 2008; Auton et al., 2009; 2010b;

Coburn et al., 2011). However, the molecular mechanism to upregulate the VWF–GPIbα interaction as the hemostatic functions are most needed remains unclear.

To elucidate the molecular mechanism regulating VWF–GPIbα interaction, we previously used atomic force microscopy and a flow chamber to show that the VWF-A1–GPIbα interaction behaved as catch-slip bonds such that increasing force initially prolonged and then shortened bond lifetime (Yago et al., 2008). However, another recent study using optical tweezers observed a different phenomenon at forces lower than those examined by us, reporting an A1–GPIbα bond that could flex between two slip-bond states at ~10 pN (Kim et al., 2010). Note that in past studies on functional binding of A1 to GPIbα, different groups used recombinant sequences with different lengths of the N and C termini outside of the major disulfide loop (C1272-C1458) that comprises the A1 domain. These sequences can be categorized into two groups in general: most studies of flow effects on platelet adhesion used A1 constructs starting around 1238 (1238-A1) or beyond 1238 to the N terminus (N-longer A1)(Cruz and Handin, 1993; Miyata and Ruggeri, 1999; Celikel et al., 2000; Cruz et al., 2000; Arya et al., 2002; Doggett et al., 2002; Yago et al., 2008; Coburn et al., 2011); whereas most structural and kinetic studies used A1 constructs starting around 1261 (1261-A1) or shorter than 1261 at N-terminus (N-shorter A1) (Celikel et al., 1998; Emsley et al., 1998; Miura et al., 2000; Clemetson and Uff, 2002; Huizinga et al., 2002; Kim et al., 2010). In addition, many evidences infer that the discrepant N-terminal flanking sequence between the 1238- and 1261-A1 constructs (Q1238-E1260) may play an important role in the VWF activation and be responsible for discrepant observations from different studies. It has been shown that a N-shorter A1 domain (1271-1467) spanning the structurally resolved residues can bind to

GPIbα, but not support platelet adhesion as efficiently as the domain containing the N-terminal flanking sequence at high shear rates (Miyata and Ruggeri, 1999). Furthermore, it has been known that 15 residue peptides (1232-1261) completely inhibited the binding of VWF to platelet GPIbα (Mohri et al., 1988). Recently, the Q1238-E1260 sequence was suggested as a part of auto-inhibitory mechanism by stabilizing the A1A2A3 interdomain associations (Auton et al., 2012). Still, how this short N-terminal flanking sequence regulates the VWF–GPIbα interaction under force remains unclear.

To gain mechanistic insights into the regulatory effects of VWF regions surrounding A1, especially its N-terminal flanking region, on the force-dependent VWF–GPIbα interaction, we used a BFP to analyze the single-bond dissociation of GPIbα from VWF, 1238-A1 and 1261-A1 under forces lower than those previously used in the absence and presence of a Q1238-E1260 peptide in the solution. We showed that GPIbα formed catch-slip bonds with VWF and slip-catch-slip bonds with 1238-A1, which govern platelet rolling on these substrates; but slip-only bonds with 1261-A1. Soluble Q1238-E1260 inhibited platelet attachment, suppressed the respective GPIbα catch bonds with VWF and 1238-A1, but rescued that with 1261-A1. The 1238-A1 mutation R1450E that exhibits the gain-of-function (GOF) phenotype of the type 2B VWD prolonged bond lifetime at zero force whereas the 1238-A1 mutation G1324S that exhibits the loss-of-function (LOF) phenotype of the type 2M VWD shifted the respective slip-catch and catch-slip transition points to higher forces. The GPIbα mutation G233V that exhibits GOF phenotype of platelet-type VWD (ptVWD) retained the slip-catch-slip bond feature, but greatly prolonged the bond lifetime in the entire force regime.

4.2 Results

We used a BFP (Figure 2-1) to measure adhesion frequency and bond lifetime between recombinant VWF-A1 domains, pVWF, and polypeptides coated on a glass bead attached to the apex of an RBC (Figures 2-1 and 2-2, *left*) and GPIbα or glycocalicin immobilized on a target bead (Figure 2-1 and 2-2, *right*). We also measured the interaction of A1-coated probe bead with single platelet (Figure 6-1, *right*). For better molecular orientation with purified proteins, GPIbα was captured from platelet lysates by WM23 (Figure 2-2 B), a mAb with the epitope in the macroglycopeptide and does not interfere with VWF interactions region (Figure 1-2). The BFP detected the absence (Figure 2-3 A) or the presence (Figure 2-3 B) of adhesion from the force signal upon target retraction, calculated adhesion frequency from repeated tests (Figure 4-1) and measured the bond lifetime under constant forces (Figure 2-3 B).

The binding specificity was established as GPIbα-bearing targets (lysate GPIbα, glycocalicin or platelet GPIbα) adhered at significantly higher frequencies to probes coated with VWF ligands (1238-A1, 1261-A1 or VWF) than those coated without VWF ligands. Addition of anti-A1 or anti-GPIbα mAb abrogated the adhesion (Figure 4-1). The severely shortened lifetimes of the rare adhesions in the presence of an anti-GPIbα (triangle) mAb suggest the remaining adhesion events after mAb blocking are mostly nonspecific (Figure 4-4A and B).
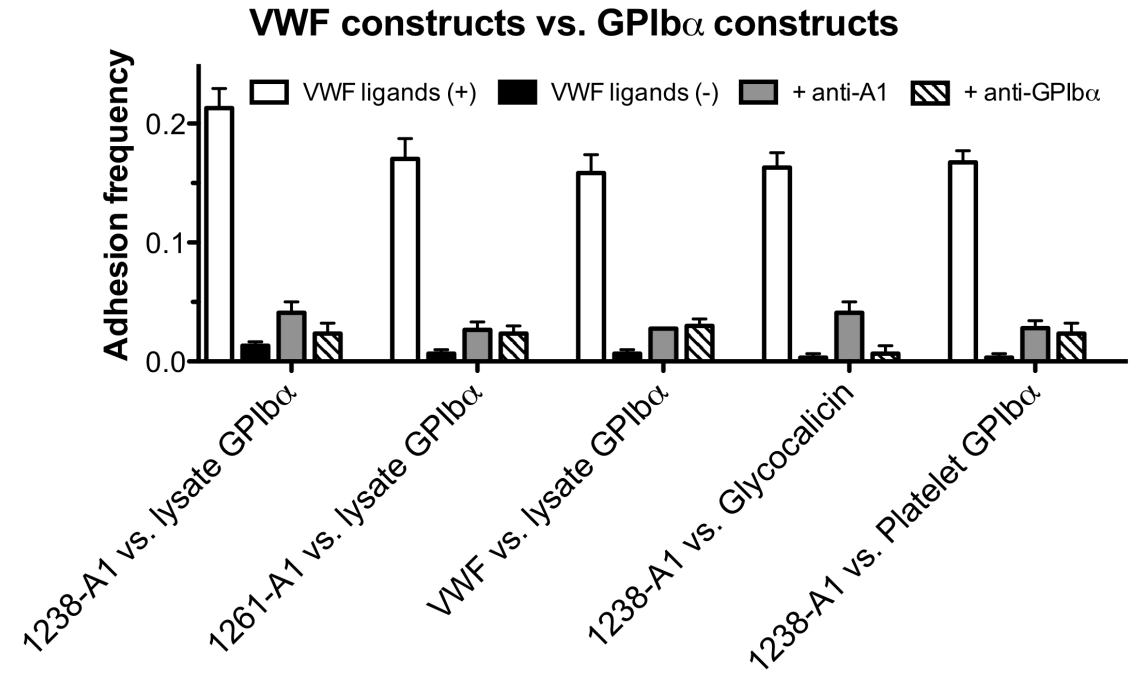
Figure 4-1. Binding specificity. Adhesion frequencies between targets coated with GPIbα constructs (platelet lysate GPIbα, glycocalicin and platelet GPIbα) and probes coated with (VWF ligands (+), white) and without (VWF ligands (-), black) VWF constructs (1238-A1, 1261-A1 and full-length VWF), in the absence or presence of 50 μg/ml anti-A1 blocking mAb (5D2, gray) and 50 μg/ml anti-GPIbα blocking mAb (AK2, hatched) in solution. Each probe–target pair was tested repeatedly for 100 approach-contact-retract cycles to estimate an adhesion frequency. Five probe–target pairs were tested to obtain mean ± S.E.M.

4.2.1   *GPIbα dissociates from 1238-A1 as a triphasic slip-catch-slip bond, 1261-A1 as a*

   monophasic slip-only bond, and full-length VWF as a biphasic catch-slip bond

Using AFM in a previous study (Yago et al., 2008), we observed that 1238-A1–glycocalicin dissociated as a biphasic catch-slip bond at forces >15 pN. A recent study using OT reported that the 1261-A1–GPIbα dissociation behaved as a "flex bond" at forces <20 pN that switched between two slip-bonds with 20-fold different off-rates (Kim et al., 2010). To investigate this apparent discrepancy, we measured single-bond lifetimes in the full force regime by BFP using both 1238- and 1261-A1 domains. The former

56

includes the Q1238-E1260 sequence whereas the latter excludes it. We observed a very similar catch-slip bond for 1238-A1 dissociation from GPIbα (captured from platelet lysates by WM23) in the same force regime to that of the previous AFM study (Yago et al., 2008) (Figure 4-2 A, ○). At forces <15 pN, however, an additional slip bond was observed, qualitatively similar to the slip bond observed in the OT study (Kim et al., 2010). In addition to force-clamp experiments, we used a thermal fluctuation assay (Chen et al., 2008a) to directly measure the bond lifetime at zero force (Figure 2-3 C). The value of 5.4 ± 1.6 s so measured matched the zero-force extrapolation of the slip bond trend in the low force regime (Figure 4-2 A, ●). Thus, the force-dependent single 1238-A1–GPIbα bond lifetime exhibits a triphasic pattern transitioning from a slip bond at 0-16 pN to a catch bond at 16-25 pN, followed by another slip bond at >25 pN.

In sharp contrast, the 1261-A1–GPIbα interaction was a slip-only bond whose lifetime decreased monotonically with increasing force (Figure 4-2 A, △). Below 15 pN, the lifetime vs. force curves of the two A1s coincided. Between 16 and 25 pN, however, the lifetime curve for 1238-A1 increased, whereas that for 1261-A1 decreased. Beyond 25 pN, the lifetimes of GPIbα bonds with both A1 domains decreased with increasing force but the bond lifetimes were significantly shorter for 1261- than 1238-A1. In addition, without force-induced bond strengthening, few 1261-A1 bonds survived the target retraction to reach >40 pN forces for lifetime measurement (Figure 4-2 A). These results indicate that the Q1238-E1260 sequence *in cis* may stabilize the A1–GPIbα interaction under force, as truncating this sequence eliminated the A1 catch bond with GPIbα.

To determine how well the GPIbα binding properties of the A1 domain represent those of VWF, we measured the force-dependent lifetime of single GPIbα bond with full-length VWF using BFP thermal fluctuation and force-clamp assays. The lifetime vs. force curve of the VWF–GPIbα bond (Figure 4-2 A, ◇) was very similar to that of the 1238-A1–GPIbα bond (Figure 4-2 A, ○) at the catch-slip bond force regime. At lower forces (<16 pN), however, the GPIbα bond with VWF continued to behave as catch bond, sharply contrasting to those with both A1s. At zero force, the GPIbα bond lifetime was ~80-fold lower with VWF than A1 (0.067 vs. 5.4 s). These data suggest an auto-inhibitory mechanism involving a sequence surrounding the A1 domain that reduced the bond stability with GPIbα. However, this inhibition can be relieved as VWF was progressively activated by increasing force such that GPIbα bond with 1238-A1 achieved its full stability as that with VWF, giving rise to the VWF–GPIbα catch bond at forces <16 pN. These data also caution us not to over-interpret and generalize binding results obtained using A1 domains before confirmation with full-length VWF.
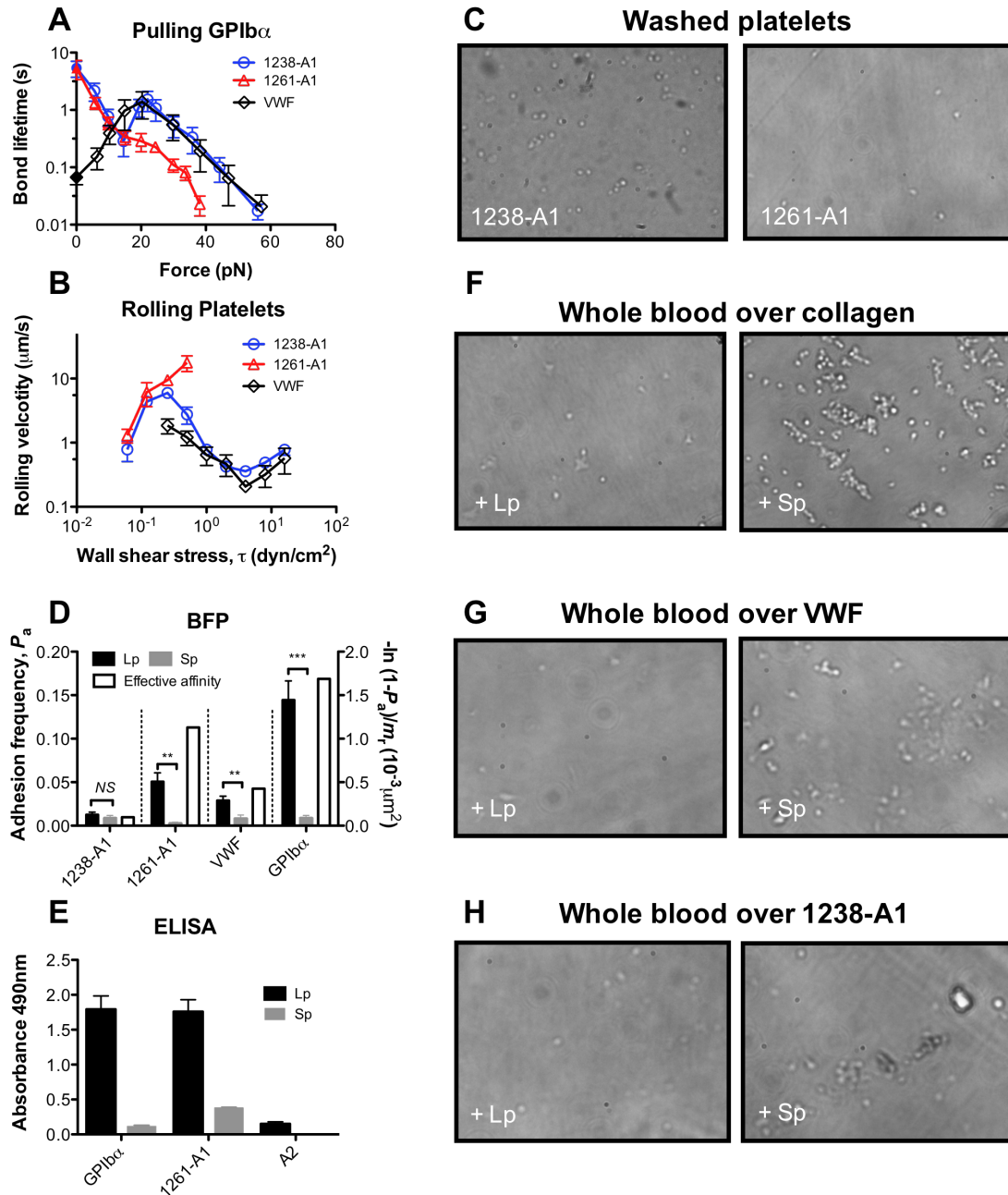
Figure 4-2. The role of Q1238-E1260 *in cis* on GPIbα interactions with VWF and 1238-A1.
(A) Force-dependent of lifetime of platelet lysate GPIbα bonds with the VWF and two forms of A1. Lifetimes (mean ± S.E.M. of >20 measurements per point) were measured by the thermal fluctuation assay (closed symbols) at zero force and by the force-clamp assay at nonzero forces (open symbols). (B) Wall shear stress-dependent rolling velocity (mean ± S.E.M. of ~20 platelets per point) on VWF and two forms of A1. (C) Platelets attach differently to 1238- and 1261-A1 coated surfaces. Washed platelets were perfused over a surface coated with 1238- or 1261-A1 at 8 dyn/cm² wall shear stress. Representative snapshots were shown. (D) Adhesion frequency P_a (left *y*-axis, closed bars, mean ± S.E.M. of >3 probe–target pairs each contacting 100 times per

bar) between targets bearing 1238-A1, 1261-A1, VWF or platelet lysate GPIbα and probes bearing Q1238-E1260 (Lp, black) or a control scramble peptide (Sp, gray). NS = not significant; ** = p < 0.01; *** = p < 0.001, assessed by unpaired, two-tailed Student's t-test. The right y-axis variable (open bars) represents a metric of the propensity of Lp binding to its counter-molecule whose variable site density (m_r, measured separately by flow cytometry) has been accounted for via the formula $-\ln(1 - P_a)/m_r$ to allow for comparison of Lp binding to 1238-A1, 1261-A1, VWF and GPIbα (Chesla et al., 1998). (E) ELISA showing specific binding of polypeptide Lp in a purified system. Data (mean ± S.E.M. of triplicates, two separate experiments) showing binding of lysate GPIbα, 1261-A1, and VWF-A2 (as a negative control) to immobilized polypeptide Lp (black columns) or Sp (gray columns) (0.5 mM). (F-H) Effect of Q1238-E1260 on platelet adhesion under shear. Whole blood mixed with 0.5 mM Lp (left column) or Sp (right column) was perfused over a surface coated with collagen (F), VWF (G), or 1238-A1 (H) at 1,500 s^{-1} wall shear rate. After a 2-min perfusion, the platelets were washed with PBS and observed microscopically. All photomicrographs are representatives of separate experiments using the same blood donor.

4.2.2 *Platelet rolling velocities on 1238-A1, 1261-A1, and VWF were governed by their respective slip-catch-slip, slip-only, and catch-slip bonds with GPIbα*

Previously, we demonstrated an inverse relationship between rolling velocity and bond lifetime – the longer the bond lifetime, the slower the rolling velocity (Yago et al., 2004; 2008) – which provided definitive evidence that flow-enhanced rolling is caused by catch bonds (Zhu et al., 2008). To corroborate the single-bond lifetime results in Figure 4-2 A, we measured platelet rolling on surfaces coated with either of the two A1 domains or VWF over a range of wall shear stresses in a flow chamber. The velocities of washed platelets rolling on these substrates showed stress-dependent patterns mirroring the corresponding patterns of bond lifetimes: triphasic for 1238-A1, monophasic for 1261-A1, and biphasic for VWF (Figure 4-2 B). At shear stress >1 dyn/cm^2, 1261-A1 no longer supported platelet rolling, preventing measurements beyond that point. This is evident from the snapshots taken at 8 dyn/cm^2 that show 1238-A1 supported platelet tethering and rolling at high shear whereas 1261-A1 did not (Figure 4-2 C).

4.2.3 Polypeptide Q1238-E1260 binds GPIbα and 1261-A1 and inhibits platelet adhesion

It has been reported that a VWF-derived polypeptide L1232-D1261 acts as a putative GPIbα binding site and can inhibit VWF binding to platelet (Mohri et al., 1988). In addition, it was recently suggested that this A1 N-terminal sequence may bind A1 noncovalently (Auton et al., 2012). We therefore measured direct binding of BFP probes bearing a similar polypeptide Q1238-E1260 (Lp) to BFP targets coated with GPIbα, VWF, 1238-A1, or 1261-A1. Specific binding of Lp to GPIbα, VWF, and 1261-A1, but not 1238-A1, was observed as the adhesion frequencies to the former three molecules (but not the last molecule) were abrogated when Lp was replaced by a control scramble polypeptide (Sp) (Figure 4-2 D, closed bars). To compare the propensies of Lp binding to these molecules, the specific adhesion frequencies (P_a, obtained by subtracting the adhesion frequency of Sp from that of Lp) were converted to effective binding affinities per unit receptor site density [$-\ln(1 - P_a)/m_r$] by normalizing the average number of adhesion bonds [$-\ln(1 - P_a)$] by the respective site densities of 1238-A1, 1261-A1, VWF, and GPIbα (m_r). Although we did not measure the site density of Lp, the same batch of Lp-bearing beads were used to analyze binding of all four receptors. Hence the respective effective affinities per unit receptor density should equal to the effective 2D affinities of Lp for 1238-A1, 1261-A1, VWF, and GPIbα multiplied by the same constant of Lp site density. The values for the latter three molecules were ~11-, 4.7-, and 17-fold higher than that for 1238-A1, respectively (Figure 4-2 D, open bars). Compared to 1261-A1 and GPIbα, the VWF binding to Lp was much weaker, possibly because this binding was mediated by the VWF structure outside 1238-A1. Additional population experiments by

ELISA (Figure 4-2 E) confirmed the direct interactions of Lp to GPIbα and 1261-A1 by single-bond experiments. Thus, VWF has at least two binding sites for GPIbα, one resides within 1261-A1 and the other involves Q1238-E1260. This sequence also binds noncovalently to 1261-A1 and other VWF domains in addition to forming a covalent peptide bond with 1261-A1 in the full-length VWF structure.

To investigate the functional role of Lp in platelet adhesion under shear, we perfused whole blood mixed with soluble Lp or Sp over a collagen-coated (Figure 4-2 F), VWF-coated (Figure 4-2 G), or 1238-A1-coated (Figure 4-2 H) surface in a flow chamber. These experiments mimic the hemostatic scenario at disrupted vascular sites where plasma VWF deposits on exposed subendothelum to capture circulating platelets (Ruggeri et al., 2006). Many more attached platelets were observed when whole blood was mixed with Sp (Figure 4-2 F-H, right panels) than with Lp (Figure 4-2 F-H, left panels), confirming the role of Q1238-E1260 to inhibit the binding between platelet and VWF (Mohri et al., 1988).

4.2.4 *Soluble Q1238-E1260 reduces GPIbα bond lifetimes with VWF and 1238-A1 but rescues the catch bond with 1261-A1*

Since Lp binds GPIbα much better than VWF (Figure 4-2 D), its inhibitory effect on platelet adhesion (Figure 4-2 F-H) may be explained by its binding to GPIbα (Figure 4-2 D and E), which may interfere, at least in part, the VWF–GPIbα interaction that mediates platelet adhesion. To test this hypothesis, we used BFP to directly measure the effect of Lp on force-dependent VWF–GPIbα bond lifetime. Supporting our hypothesis, VWF–GPIbα bond lifetime was shortened by the addition of soluble Lp (Figure 4-3 A), but not Sp (compare Figures 4-2 A and 4-3 A), over the full force regime.

To further elucidate the mechanism for the A1 N-terminal flanking region to regulate platelet binding, we measured lifetimes of GPIbα bonds with 1238-A1 and 1261-A1 in the presence of soluble Lp or Sp. As expected, the respective lifetime vs. force curves of GPIbα interactions with 1238-A1 and 1261-A1 were indistinguishable in the absence (Figure 4-2 A) and presence (Figure 4-3 B and C) of Sp, for the control sequence should have no effect. In the presence of Lp, however, the lifetime curves of the 1238-A1 (Figure 4-2 B) downshifted but still retained its triphasic profile. More interestingly, the monophasic lifetime curve of 1261-A1 became triphasic, first decreasing, then increasing, and again decreasing with increasing force (Figure 4-3 C). In fact, in the presence of Lp, the 1261-A1 and 1238-A1 curves were close to each other but distinct from the VWF curve. Thus, soluble Q1238-E1260 suppresses GPIbα binding to VWF and 1238-A1, but rescues the GPIbα catch bond with 1261-A1. The former suggests that Lp competes for GPIbα binding with VWF and 1238-A1 while the latter suggests that a possible 1261-A1–Lp–GPIbα sandwich bond may restore the catch bond behavior. These data show that the Q1238-E1260 sequence plays a similar role *in trans* as it does *in cis* in stabilizing the A1–GPIbα bond against increasing force. The inability for the recent OT study (Kim et al., 2010) to observe GPIbα catch bond may be explained by their use of 1261-A1 in the fusion construct.
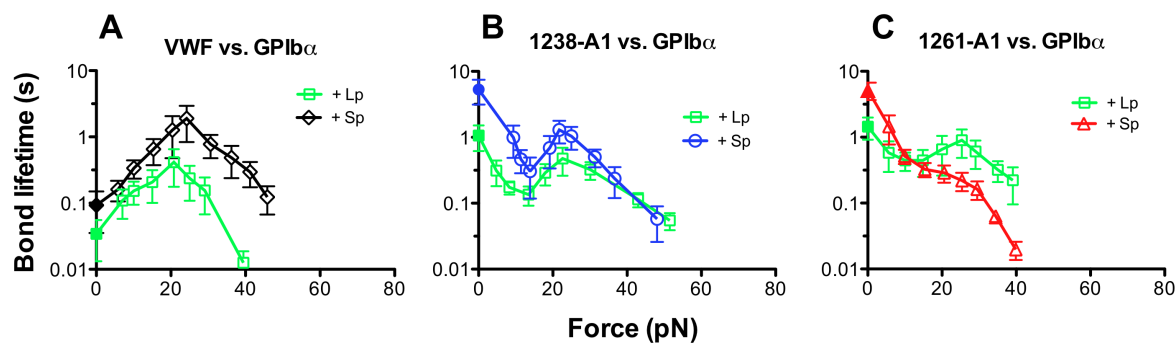
Figure 4-3. The effect of Q1238-E1260 on GPIbα interactions with VWF and two forms of A1 when it is in solution. (A-C) Plots of lifetime of vs. force of lysate GPIbα bonds with VWF (A), 1238-A1 (B) and 1261-A1 (C) in the presence of Lp or Sp in solution (10 μg/ml or 4.2 μM). Lifetimes (mean ± S.E.M. of >20 measurements per point) were measured by the thermal fluctuation assay (closed symbols) at zero force and by the force-clamp assay at nonzero forces (open symbols).

4.2.5 *Effects of different forms of WT GPIbα*

In addition to studying different force regimes and using different VWF A1 domains, another possible cause of the discrepancies between our previous AFM data (Yago et al., 2008) and the OT data from another study (Kim et al., 2010) may be the use of different forms of GPIbα. To test this possibility we compared GPIbα captured from platelet lysates by WM23 mAb on target beads (Figure 2-2 B) with native GPIbα expressed on platelets (cf. Figure 6-1 A) and glycocalicin covalently linked to target beads (Figure 2-2 A). The dissociation of 1238-A1 from glycocalicin (Figure 4-4A, black square) and GPIbα either captured from platelet lysates (Figure 4-4, □) or expressed on platelets (Figure 4-4 B, □) display overlapping triphasic force-dependent lifetime curves. In addition, to study the ptVWD with mutations on GPIbα, we used the CHO cell system in which GPIb-IX was transfected (CHOαβ9) (Dong et al., 2000). The GPIbα was captured to the BFP from lysates of CHOαβ9 cells as it was from platelet lysates. The lifetime curves for WT GPIbα from the two sources, CHOαβ9 and platelet lysates (Figure

4-4 C), are indistinguishable. These data indicate that the 1238-A1–GPIbα bond dissociation characteristic is determined by the extracellular domain of GPIbα and not affected by how it is immobilized on surfaces and validated the consistency among three GPIbα sources we discussed in this paper: glycocalicin, CHOαβ9 and platelet.
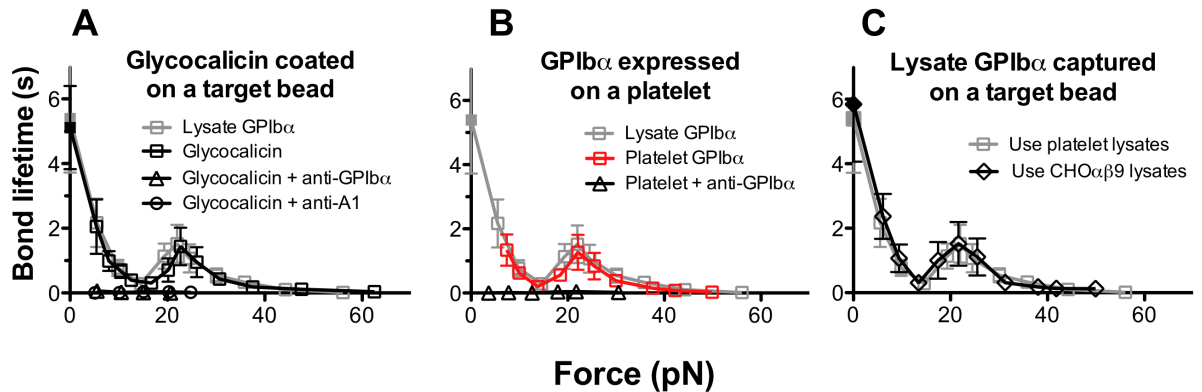
Figure 4-4. Force-dependent lifetimes of WT A1 bonds with different GPIbα preparations. Plots of lifetime vs. force of 1238-A1 bonds with glycocalicin (A, □) coated on a target, GPIbα expressed on a platelet (B, □) in the absence (open square) and presence of 50 μg/ml anti-A1 (5D2, O) or anti-GPIbα (AK2, △) and lysate GPIbα from CHOαβ9 cells (C, ◇). The previous data from Figure 4-2 A of 1238-A1 interaction with lysate GPIbα from platelets were replotted for comparison in each panel (□). Lifetimes (mean ± S.E.M. of >20 measurements per point) of these bonds were measured by the thermal fluctuation assay (closed symbols) at zero force and by the force-clamp assay at nonzero forces (open symbols).

4.2.6 *Effects of VWD mutants*

The putative conformational change resulting in VWF activation may be induced or affected by VWF or GPIbα mutations naturally occurring in patients with VWD. Our previous AFM study demonstrated that a type 2B VWD mutation 1238-A1R1450E eliminated the catch bond found in the 1238-A1-glycocalicin interaction by prolonging the lifetimes at low forces, resulting in an up- and left-shift of the lifetime vs. force curve relative to the WT curve (Yago et al., 2008). In contrast, a type 2M VWD mutant 1238-A1G1324S shortened lifetimes at low forces and right-shifted the biphasic catch-slip bond

curve towards higher forces (Auton et al., 2009). The present BFP study extended the lifetime vs. force curves for these mutants to lower forces. We found that glycocalicin dissociated from 1238-A1R1450E as a monophasic slip-only bond (Figure 4-5 A, ☐) but from 1238-A1G1324S as a right-shifted triphasic slip-catch-slip bond (Figure 4-5 B, ☐), qualitatively similar to the WT 1238-A1 (Figure 4-5, ☐). These data confirm the previous AFM results at forces >20 pN and add a new slip-bond regime at low forces for 1238-A1G1324S. The extended results also included lifetimes at zero force measured via the thermal fluctuation assay, which are 13.9 ± 2.7 s and 4 ± 1.1 s for R1450E (Figure 4-5A, ■) and G1324S (Figure 4-5B, ■), respectively. The former value is much longer while the latter value is slightly shorter than the zero-force lifetime of 5.1 ± 1.2 s for the WT 1238-A1 (Figure 4-5, ■), explaining the GOF phenotype for R1450E and the LOF phenotype for G1324S. We also studied a ptVWD mutant GPIbα (G233V) with our CHOαβ9 system (Figure 4-5 C). Consistent with its GOF phenotype in other assays (Marchese et al., 1999; Doggett, 2003; Kumar et al., 2003), the lifetime vs. force curve of 1238-A1 bonds with GPIbαG233V (Figure 4-5 C, ☐) was significantly upshifted relative to that with WT GPIbα (Figure 4-5 C, ☐). The zero force lifetime measured by the thermal fluctuation assay was 20.5 ± 7.4 s, ~4-folds longer than the WT value of 5.8 ± 1.8 s.
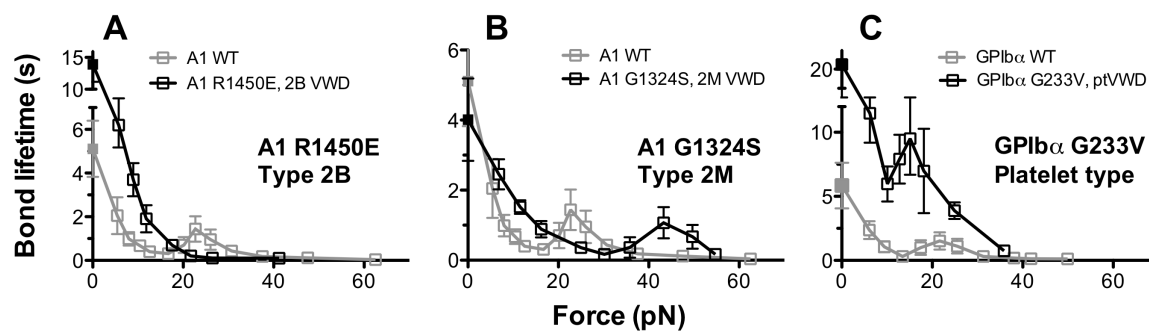
Figure 4-5. Force-dependent lifetimes of A1–GPIbα bonds with VWD mutantations. (A and B) Plots of lifetime vs. force of glycocalicin bonds with type 2B VWD mutant R1450E (A) and type 2M VWD mutant G1324S (B) 1238-A1s (□) The previous data from Figure 4 of WT 1238-A1 interaction with glycocalicin were replotted for comparison (□). C. Plots of lifetime vs. force of WT (□) and G233V (□) lysate GPIbα bonds with 1238-A1. Lysates used for this panel are from CHOαβ9 cell lines expressing WT and G233V GPIbα. The GPIbα were captured from the lysate by WM23 mAbs. Lifetimes (mean ± S.E.M. of >20 measurements per point) of these bonds were measured by the thermal fluctuation assay (closed symbols) at zero force and by the force-clamp assay at nonzero forces (open symbols).

4.2.7   *Characterization of A1–GPIbα dissociation by a two-state model*

In addition to the force-dependent average of lifetimes, their distributions also demonstrated that GPIbα dissociated from 1238-A1 (Figure 4-6 A-C) as slip-catch-slip bonds, but from 1261-A1 (Figure 4-6 D-F) as slip-only bonds. For the first-order irreversible dissociation of a single monomeric bond from a single state along a single pathway in a single step, lifetime at each force bin should follow a single-exponential distribution, appearing linearly in the semi-log survival frequency vs. lifetime plot, with the negative slope equal to the off-rate. However, the semi-log lifetime distributions at many force bins (Figure 4-6) appear as two line segments connected at ~2 s, invalidating the assumption underlying the simple kinetics model that predicts a single exponential decay (Equation 2-3; see section 2.6.1). We found that such multi-exponentially distributed lifetimes are similar to those of the bonds between $\alpha_5\beta_1$ integrin and fibronectin (Kong et al., 2009; 2013) and between $\alpha_L\beta_2$ integrin and intercellular adhesion

67

molecule 1 (Chen et al., 2010; 2012), but distinct from those of the bonds between P- or L-selectin and P-selectin glycoprotein ligand 1 or other ligands, whose lifetimes are distributed as single exponentials (Marshall et al., 2003; Sarangapani et al., 2004).
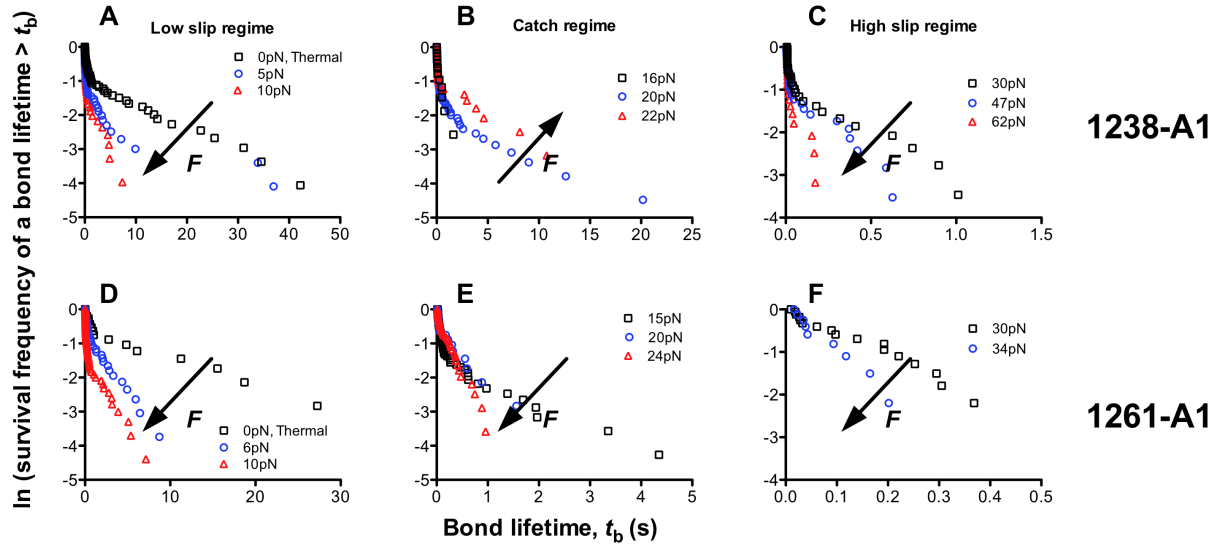
Figure 4-6. Bond lifetime distributions. Survival frequencies, calculated as the fraction of measurements (including both short and long lifetime events) with a bond lifetime $>t_b$, were plotted vs. t_b for each force bin in each of three regimes – low (A, D), intermediate (B, E), and high (C, F) forces – for GPIbα dissociation from 1238-A1 (A-C) and 1261-A1 (D-F). These forces corresponded to the low slip bond, the catch bond, and the high slip bond regime for 1238-A1 interactions, but 1261-A1 interactions only showed slip bonds in entire force regimes. The arrows indicate the directions of force increase.

Assuming that two subpopulations of A1–GPIbα bonds coexist and dissociate at a slow (k_1) and a fast (k_2) off-rate, respectively, we analyzed the lifetime distributions using a two-state model (Equation 2-4, see section 2.6.2) to obtain the best-fit force-dependent off-rates and their associated fractions of these subpopulations of bonds of GPIbα with 1238-A1 (Figure 4-7 A and B) and with 1261-A1 (Figure 4-7 C and D). For GPIbα dissociation from 1238-A1, the off-rate of the long-lived bond (k_1) is one order of magnitude smaller than that of the short-lived bond (k_2) at zero force (Figure 4-7 A).

68

Since the fractions of the long-lived (ω_1) and short-lived (ω_2) bonds are similar (Figure 4-7 B), the long-lived bonds dominate the average lifetime. Although the relative fractions are stable around the catch bond force regime, overall, force gradually increases the fraction of short-lived bonds at the expense of the long-lived bonds. The fast off-rate k_2 increases monotonically as the force increases. By comparison, the slow off-rate k_1 first increases, then decreases, and again increases with force, accounting for the triphasic slip-catch-slip bond behavior. Surprisingly, two states merge at force above 60pN (Figure 4-7 A), only one state remains (Figure 4-7 B).
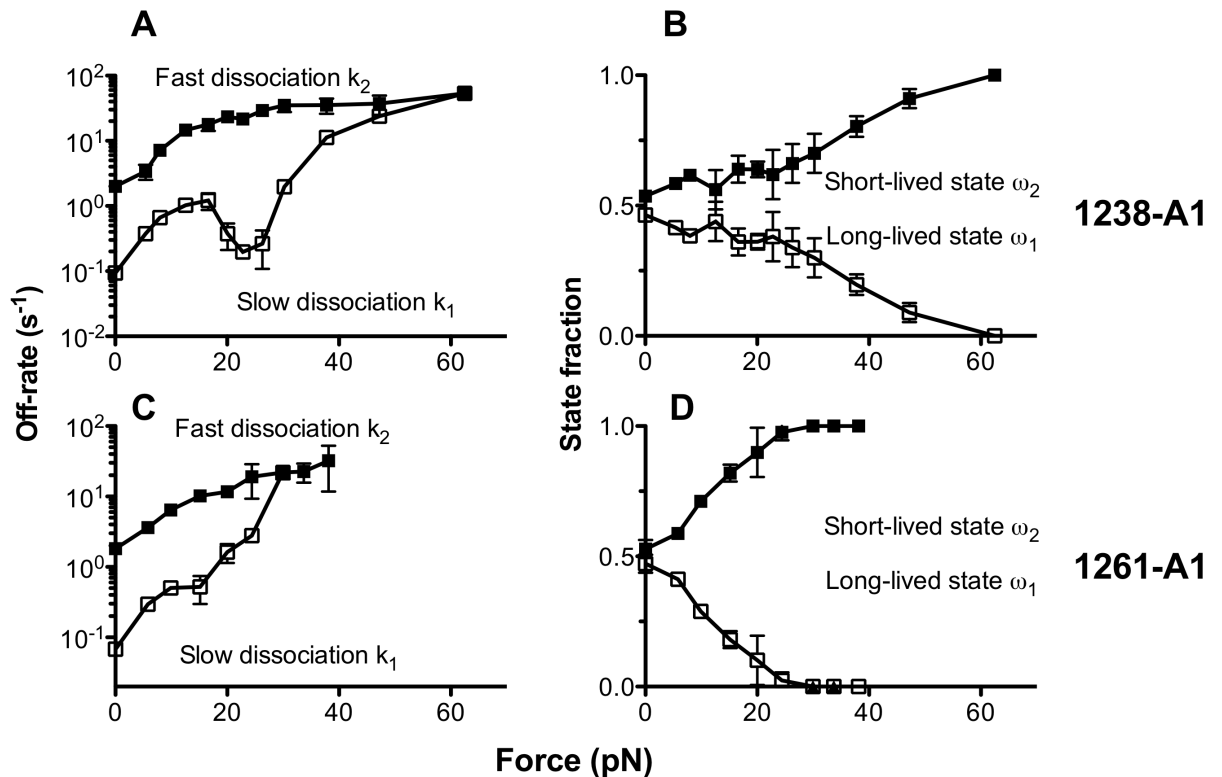
Figure 4-7. Analysis of two-state kinetics. A two-state model was fit to the bond lifetime distribution at each force bin (Figure 4-2A) of GPIbα dissociation from 1238-A1 (A and B) or 1261-A1 (C and D) to evaluate three model parameters at that force, which are plotted vs. force. The kinetic parameters are: a slow (k_1) and a fast (k_2) off-rate of dissociation from the two states of different stabilities (A and C) and the fractions (ω_1 and ω_2, $\omega_1 + \omega_2 = 1$) of bonds associated with the corresponding short-lived (high off-rate) and long-lived (low off-rate) states (B and D). Error bars represent ± 95% confident interval of the best-fit value.

For the dissociation of GPIbα from 1261-A1, the two off-rates differ by one order of magnitude at zero force (Figure 4-7 C), which is consistent with the results obtained by the recent optical tweezers study at low forces.(Kim et al., 2010) Although the initial relative fractions are similar to those of 1238-A1 bond, two states of 1261-A1 bond merge at much lower force ~30 pN than those of 1238-A1 bond do. The long-lived state disappears while the k_1 rapidly increased from 0.07 to 21.9 s^{-1} joining the monotonic trend of k_2. Concurrently, ω_1 rapidly decreases from 0.5 to 0, whereas ω_2 rapidly increases from 0.7 to 1.0, resulting in dissociation from a single state (Figure 4-7 D). This analysis confirms that losing the Q1238-E1260 sequence makes force dissociates 1261-A1 much faster than 1238-A1 from GPIbα.

4.2.8   *Comparison with previous measurements by different methods*

We replotted the lifetime vs. force curves in Figure 4-2 A to compare with previous data obtained by a AFM with 1238-A1(Yago et al., 2008) and a optical tweezers with 1261-A1 (Kim et al., 2010). At low forces, the optical tweezers measurements determined two states that dissociated at distinct rates (Figure 4-8 A, ○ and △): one state at low forces and the other engaging at ~10 pN with a 20-fold longer lifetime and a greater force resistance. The authors termed this behavior "flex bond" (Kim et al., 2010). For a direct comparison, we overlaid the 1261-A1 lifetime distributions measured by the BFP (Figure 4-8 B, black) on those measured the optical tweezers at ~10 pN (Figure 4-8 B, blue). The BFP measurement at ~10 pN also shows two states, although only the long-lived state is consistent with the optical tweezers measurements. However, we observed two states at forces between 0 and 60 pN for 1238-A1 (Figure 4-8 B) and between 0 and

30 pN for 1261-A1 (Figure 4-8 D) instead of just a single state below 9.55 pN that flexed to another state above 10.05 pN (Kim et al., 2010). The effect of force measured by the BFP was gradual; 1-pN force change around 10 pN did not drastically change two-state characteristics the A1-GPIbα bond (Figure 4-8 B, black).
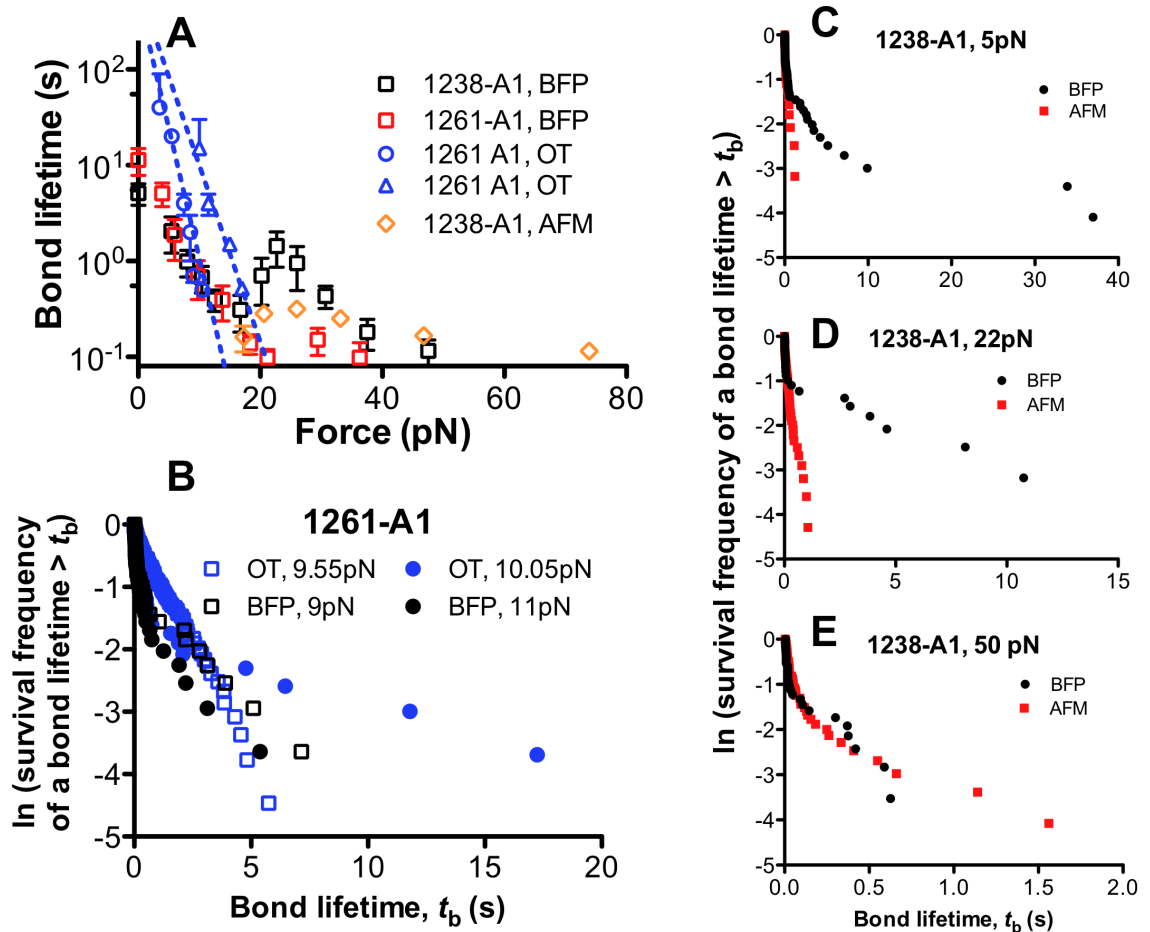
Figure 4-8. Comparison with previous results. A. Plots of lifetime (mean ± S.E.M. of >20 measurements) vs. force of GPIbα bonds with 1238-A1 (□) or 1261-A1 (□) measured by BFP in this study, with 1238-A1 measured by AFM in our previous study(Yago et al., 2008) (◇), and with 1261-A1 measured by OT in a previous study(Kim et al., 2010) (○ and △). B. Comparison of 1261-A1 lifetime distributions measured by BFP in this study (black symbols) and by OT in the previous study(Kim et al., 2010) (blue symbols) at two very close force bins (square and circle). C-E. Lifetime distributions measured by BFP in this study (black) and those measured by AFM in our previous study (red) were compared at three representative forces: 5 pN for the low-force regime where the low slip bond was observed in this study but not in our previous study (C), 22 pN for the intermediate-force regime where the catch bond was observed in both of our studies (D), and 50 pN for high-force regime where the high slip bond was observed (E) in both of our studies.

The second and third phases of the triphasic bond lifetime vs. force curve in the present BFP study are qualitatively similar to the biphasic lifetime curve observed in our previous AFM study in the same force range and with the same 1238-A1 construct, but have quantitatively longer lifetimes (Yago et al., 2008). This is due to an improvement − a counter-drifting system − to the BFP used in the present study, which enabled us to measure longer bond lifetimes. By comparison, bond lifetimes >2 s were excluded as possible outliers in our previous AFM experiments (Yago et al., 2008), for they might be affected by instrument drifting and/or resulted from multiple bonds. This can be seen by overlaying the lifetime distributions of the present BFP study with those of the previous AFM study measured at three representative force bins. Due to the 2-s cut-off in the lifetime measurement, the AFM data only match the short-lived state portion of the BFP data in the first slip regime (5 pN, Figure 4-8 C) and the catch regime (22 pN, Figure 4-8 D) but miss the long-lived state of the BFP data, explaining the shorter average lifetimes of the AFM data than the BFP data (Figure 4-8 A). By comparison, the AFM and BFP data match well in the second slip bond regime (55 pN, Figure 4-8 E) where the short-lived state dominates over the long-lived state (Figure 4-7 B), thus preventing the 2-s cut-off used in the AFM study from biasing the data.

4.3 Discussion

The results presented demonstrate following properties of the final step of VWF activation process, the regulation of A1 binding affinity to GPIbα, on the single-bond level.

1) Increasing force within a certain range strengthens the binding between GPIbα and 1238-A1 or pVWF (A catch-bond effect). The truncation of the N-terminal flanking region Q1238-E1260 abolishes the catch bond. The present work has thus characterized of the force-dependent dissociation kinetics of GPIbα interaction with both 1238-A1 and 1261-A1, triphasic slip-catch-slip for the former and monophasic slip-only bond for the latter (Figure 4-2 A and B). Note that similar triphasic force-dependent kinetics has been observed by us in the dissociations of sLe^x-bearing microspheres and carbohydrate ligand-expressing cells from E-selectin (Wayman et al., 2010).

2) The N-terminal sequence balances the A1 binding strength to GPIbα. Addition of this sequence in a peptide form (Lp) to solution weakens the catch bond for VWF and 1238-A1 by downshifting their lifetime curves (Figure 4-3 A and B) while rescues the catch bond for 1261-A1 by prolonging lifetime of its bond with GPIbα at intermediate forces (Figure 4-3 C). The former can be explained by an inhibitory role of Lp which was suggested previously (Mohri et al., 1988) and confirmed in this study: addition of Lp to whole blood suppressed platelet attachment to immobilized collagen (Figure 4-2 F), VWF (Figure 4-2 G), and 1238-A1 (Figure 4-2 H) under flow, which may be explained, at least in part, by the competitive binding of this polypeptide to GPIbα (Figure 4-2, D and E). This

may reduce the VWF–GPIbα complex interface, thereby shortening bond lifetime (Figure 4-3 A). Note that the zero force lifetimes for VWF and both 1238- and 1261-A1s are dropped by solution Lp (Figure 4-3), this suggests the inhibitory effect of Lp sequence is sound at the low force regime; The latter suggests the similar function of Q1238-E1260 in stabilizing the A1–GPIbα interaction against the increasing force when it exists *in cis* (Figure 4-2 A, 1238-A1) and *in trans* (Figure 4-3 C, 1261-A1 + Lp) to A1. A possible physiological significance of this N-terminal sequence is to delicately balance the platelet adhesion: inhibits the A1 binding to GPIbα at low force (Inactivate VWF at physiological shear) but enhances it as force increases (Activate VWF at pathological shear).

3) VWD mutations within A1 domain alter the force threshold of conformational transition. We extended our previous results on two 1238-A1 mutations, R1450E and G1324S. We showed that R1450E eliminates the catch bond by prolonging bond lifetime at low forces (Figure 4-5 A) and G1324S right-shifts the bond lifetime vs. force curve (Figure 4-5 B). Importantly we used the thermal fluctuation assay to show that the bond lifetime at zero force for R1450E is ~2-fold longer than WT while that for G1324S is shorter than WT. The bond lifetimes of the ptVWD mutant GPIbαG233V are longer than WT globally. These results are consistent with their respective GOF and LOF phenotypes found in other assays (Marchese et al., 1999; Doggett, 2003; Kumar et al., 2003; Auton et al., 2007; Coburn et al., 2011). Moreover, the increasing force mediated by the A1–GPIbα bond was proposed to transitions A1 conformation from native state (low affinity) to intermediate state (high affinity) (Auton et al., 2010b). Therefore,

our data clearly show that type 2B mutations at zero force is closer to a high-affinity state while type 2M mutation is in opposite. This explains the spontaneous binding of VWF to platelet for type 2B (Matsushita and Sadler, 1995; Ruggeri, 2004) and platelet-type (Marchese et al., 1999; Doggett, 2003; Kumar et al., 2003) VWDs while the ineffective binding of VWF to platelets for type 2M VWD (Rabinowitz et al., 1992; Morales et al., 2006) observed *in vitro*.

In contrast to our observed VWF–GPIbα catch bond by measuring a bond lifetime and rolling velocity with BFP (or AFM previously(Yago et al., 2008)) and flow chamber respectively using glycocalicin-coated microspheres or platelets to interact with surfaces coated with 1238-A1 or full-length VWF. Another study reported a flex bond at forces <20 pN transitioning from one slip bond with a fast off-rate at forces <8 pN to another slip bond with a slow off-rate at forces >12 pN. This was measured by optical tweezers using a molecular construct that links the GPIbαN and the 1261-A1 together by a 43-residue polypeptide (Kim et al., 2010). Besides the different force regimes used in the two studies, the present work has identified different A1 constructs used as the cause for the discrepancies (Figures 4-2 A and 4-8 A). Interestingly, considerable variations in their ability to support platelet attachment between the N-longer and N-shorter A1 was reported a long time ago. It showed that a N-longer A1 interacted with platelets at all shear rates tested (from 50 to 6000 s^{-1}) in a manner indistinguishable from full-length VWF while a N-shorter A1 exhibited progressive loss of function with increasing shear above 1500 s^{-1} and was essentially inactive at 6000 s^{-1}. Here we confirmed this observation by flowing washed platelets over the 1238- and 1261- A1 coated surfaces and showed that 1261-A1 did not support platelet tethering and rolling well as shear

increases (Figure 4-2 C). Overall, our data indicate that the 1238-A1 (N-longer) is a better model for studying the VWF–GPIbα interaction because it captures the catch-bond behavior observed with both a A1A2A3 construct and full-length VWF (Yago et al., 2008; Wu et al., 2010). By comparison, the 1261-A1 (N-shorter) loses the catch bond behavior at higher forces shown to be important to flow-enhanced platelet adhesion to VWF (Yago et al., 2008) and can not support platelet adhesion well as N-longer A1 can in flow assays.

Furthermore, the AN51 mAb was found to be unable to recognize glycocalicin when it was directly coated on the plastic surface but able to recognize GPIbα purified from platelet lysates and reconstituted in a nanodisc (Yan et al., 2011). Here we showed that the dissociation of GPIbα from plasma pVWF similar to that from the 1238-A1 at catch-bond force regime (Figure 4-2 A) suggesting the isolated A1 domain can recapitulate the VWF binding under shear forces. By comparison, the dissociations of surface-bound 1238-A1 from immobilized glycocalicin and lysate GPIbα as well as from platelet GPIbα follow the same force-regulated kinetics (Figure 4-4).

Note that the current crystal structures of A1 complexed with(Huizinga et al., 2002; Dumas et al., 2004) and without(Emsley et al., 1998; Celikel et al., 2000) GPIbαN are all based on the 1261-A1 (Figure 4-9 A), therefore, the molecular insights of the A1 N-terminal sequence are still missing. Here we gave a try on the structure of 1238-A1 by docking the predicted Lp structure (Figure 4-9 B) onto the published 1261-A1 structures. The initial structures of 1261-A1 (1261-1467) were based on two Protein Data Bank (PDB) entries: 1SQ0 (Dumas et al., 2004) for sequence 1268-1467 and 1U0N (Fukuda et al., 2005) for 1261-1267. The structural prediction of the N-terminal polypeptide (Lp,

1238-1260) was obtained initially with molecular docking and optimized further with molecular dynamics simulations. The initial docking of Lp was performed using the flexible docking program AutoDock4 (Morris et al., 2009) and the protein structure modeling program Modeler (Sali and Blundell, 1993). Five docked models with lowest energies were retained for further energy miniminzation and molecular dynamics simulations. All energy minimization and molecular dynamics simulations were performed with NAMD (Phillips et al., 2005) and CHARMM22/CMAP (MacKerell et al., 1998). Solvated and neutralized system was simulated with the periodic boundary condition, a 12-Å cutoff, and particle mesh Ewald summation for the electrostatic interactions. Each docked model of Lp was simulated for 20 ns. Two models gave the same final conformation, which were used as the final structural model (Figure 4-9 B).

Consider that this N-terminal sequence is highly dynamic, we drew a model here to show a plausible 3D model of 1238-A1–GPIbαN complex (Figure 4-9 C). Because we showed that the Lp binds to both GPIbα and 1261-A1 (Figure 4-2 B). The former explains its inhibitory effect while the latter supports the hypothesis that this sequence may bind to A1 itself (Auton et al., 2012). In our model, N-terminal sequence locates between GPIbαN and 1261-A1 providing the access to both parts. On one side, it interacts with the boundary between the β-finger and the first leucine rich repeat of GPIbα (Figure 4-9 C).
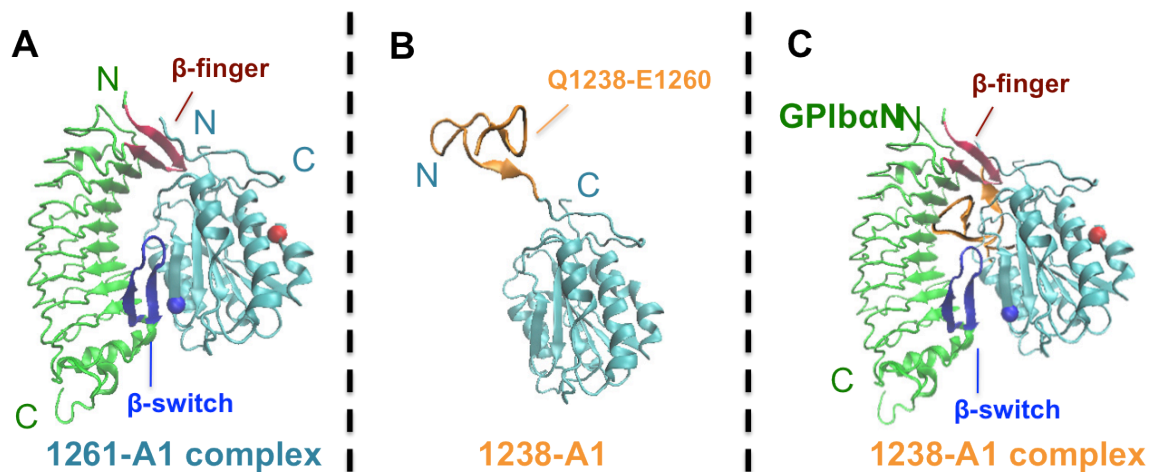
Figure 4-9. Model of 1238-A1–GPIbα complex. A. The co-crystal structure of 1261-A1–GPIbαN (PDB entry 1SQ0 (Dumas et al., 2004)). B. The 3D docking model of 1238-A1 by combining the predicted structure of Lp (Q1238-E1260, orange) and the crystal structure of 1261-A1 (cyan, PDB entries 1SQ0 (Dumas et al., 2004) and 1U0N (Fukuda et al., 2005)). C. Schematic of the 1238-A1–GPIbα complex. According to the co-crystal structure, 1261-A1 (cyan) binds to the GPIbαN (green) with two contact interfaces. The β-switch (blue) of GPIbα binds near the bottom of A1 and the β-finger (red) binds near the top. In this complex model, the predicted Lp wedges in between GPIbαN and 1261-A1. The Lp interacts with the boundary of the β-finger and the first leucine rich repeat of GPIbαN and folds back toward the A1, allowing possible binding to A1 or even D' (not shown). The R1450E (red dot) and G1324S (blue dot) mutations are indicated.

Previously, the A1–GPIbα catch bond was explained by a sliding-rebinding model: pulling force slides the GPIbαN β-finger over the 1261-A1, enabling the formation of a salt bridge between GPIbα E14 and A1 R1334 (Yago et al., 2008). If the docking model captures the essentials of the Lp, it indeed further supports the sliding possibility involving the 1238-1260 as a part of the sliding-rebinding interface. In another word, the new bonds may form between the Lp and β-finger when force slides over their relative positions. One thing to notice is that the catch bond is explained by using the 1261-A1 structure in the MD simulation (Yago et al., 2008). However, we did not observe the catch bond with the 1261-A1 in this study. A possible explanation is that the truncation of the N-terminal sequence may alter the A1 conformation or make the A1

structure unstable thereby easy to change. Previous experimental results suggest a N-longer A1 adopts a different conformation from a N-shorter A1 (Miyata and Ruggeri, 1999). Maybe the simulation captures the catch bond mechanism for 1238-A1 but the slip-bond 1261-A1 adopts a different conformation from the catch-bond conformation.

In addition, we have identified two states – one short-lived (<2 s) and the other long-lived (>2 s) – by fitting the lifetime distribution data (Figures 4-6 and 4-7). This is consistent with the previous optical tweezers study, although we observed the two-state dissociation in a much broader force range than the abrupt flex between the two states at 9-11 pN (Kim et al., 2010). Two types of structural models for catch bonds have been proposed, one based on allosteric mechanisms (Chen et al., 2010; Le Trong et al., 2010; Xiang et al., 2011) and the other based on a sliding-rebinding mechanism (Lou et al., 2006; Lou and Zhu, 2007; Yago et al., 2008), which are not mutually exclusive. The data of two-state dissociation are consistent with both. Note that the 1261-A1 complex structure (Huizinga et al., 2002; Dumas et al., 2004) shows that the concave face of GPIbαN grabs A1 in a pincher-like grip with two contact interfaces, one at the β-finger and the other at the β-switch (Figure 4-9). Our previous MD simulation shows that the β-switch dissociates from the A1 central β-sheet first, then the rupture of the E14:R1334 interaction led to complete dissociation of GPIbαN from A1 (Yago et al., 2008). Therefore, it suggests that long-lived bond state corresponds to the stronger interaction at the β-finger interface while the short-lived bond state corresponds to the weaker interaction at the β-switch interface.

In conclusion, for the very first time we demonstrated the interplay between a physical factor (rheological) force and a structural factor (biochemical) N-terminal sequence Q1238-E1260 on regulation of VWF–GPIbα interaction on a single-molecule level. Force-dependent conformational equilibria between the A1 domain and its N-terminal flanking sequence appear to regulate the final step of VWF activation. The early efforts to obtain a crystal structure of a N-longer A1 were unsuccessful until it was truncated into a N-shorter A1 (Emsley et al., 1998). Unfortunately, the N-terminal sequence, i.e. Q1238-E1260, inhibits the crystal growth and precludes an accurate structure-based mechanism of N-longer A1 binding to GPIbα. The regulatory role of N-terminal flanking region on the VWF–GPIbα interactions and its impact on hemostasis and thrombosis represent an important area of future studies.

CHAPTER 5: TRANSPORT REGULATION OF 2D KINETICS OF VWF–GPIB-ALPHA ASSOCIATION

5.1 Introduction

To initiate platelet binding to disrupted vascular surfaces under conditions of rapid blood flow, as occurs in arterioles and stenotic arteries, platelet GPIbα must associate with VWF-A1 at rapid on-rate under dynamic shear conditions (Savage et al., 1996; 1998; Ruggeri, 1999). Alteration in such unique biomechanical properties of VWF-GPIbα bonds by mutation will lead to the bleeding disorder, i.e. ptVWD (Doggett, 2003). A cardinal feature of GPIbα-mediated platelet adhesion to VWF is its dependence on blood flow (Mazzucato et al., 2007; Zhu et al., 2008). Similar to the flow-enhanced leukocyte tethering mediated by selectin–ligand interactions (Finger et al., 1996; Yago et al., 2007), increasing flow augments platelet adhesion despite higher dislodgment forces, until an optimal flow level is achieved. In fact, a minimal flow rate is required for platelets to successfully tether to and roll on VWF-bearing surfaces (Savage et al., 1996; Doggett et al., 2002). However, compared to the force-dependent VWF–GPIbα dissociation (Yago et al., 2008), our understanding of the biophysical regulation of the flow-imposed transport mechanisms on VWF–GPIbα association and its implications to platelet adhesion are rather limited.

During hemostasis or thrombosis, platelets are carried by the blood flow towards the affected vessel wall where VWF is immobilized. They also undergo translational Brownian diffusion as they are susceptible to thermal excitations from the environment.

81

Both modes of physical transport – convection and diffusion – drive platelets to collide with vascular surface, bringing interacting receptors and ligands to the close proximity. For VWF to successfully dock with GPIbα, the two molecules also have to properly orient their binding pockets through rotational diffusion, a transport mechanism at molecular scale in addition to platelet-level convection and diffusion. Thus, bond association should depend on the relative velocity and separation distance of the opposing protein-bearing surfaces, the Brownian motion of platelet as well as the rotational diffusivity of the molecules (Yago et al., 2007; Zhu et al., 2008). Based on the previous work on selectin–ligand interactions (Yago et al., 2007; Zhu et al., 2008), these three transport mechanisms have all been postulated to be responsible for flow-enhanced platelet association to VWF. We quantitatively tested the hypothesis by examining how various transport factors affect the formation of VWF–GPIbα bonds.

Single-bond analysis with a biomembrane force probe (BFP) has been employed to measure the two-dimensional (2D) binding kinetics of various receptor–ligand pairs residing on opposing surfaces (Zhu et al., 2002). The BFP thermal fluctuation assay provides a powerful tool for measuring 2D kinetics by pinpointing bond association and dissociation in a sequence of real-time fluctuations of an ultrasensitive probe (Chen et al., 2008a; 2008b). However, the waiting time from the previous bond dissociation to the next bond formation involves not only the intrinsic association rate constant but also transport factors from both cellular and molecular level. To extract the intrinsic kinetic on-rate from the apparent waiting time measurements requires a theoretical framework to account for these factors. In a set of experiments, we improved the BFP thermal fluctuation assay to allow more precise kinetic measurements under simultaneous

manipulation of several transport factors hypothesized to regulate VWF–GPIbα association: separation distance of protein-bearing surfaces, BFP spring constant, bead size and medium viscosity. The experimental data were well simulated by a receptor-coated bead diffusing towards and reacting with a ligand-bound surface. The combined experimental and theoretical results elucidate the transport mechanisms by which the 2D association kinetics of surface-bound receptors and ligands is regulated.

5.2 Results

With a similar BFP setup to what we described in the previous chapter (Figure 5-1 A), recombinant VWF-A1 and glycocalicin (GC) were coated on a probe bead attached to the apex of an RBC (Figure 5-1 A and B, *left*) and a target bead (Figure 5-1 A and B, *right*), respectively. Bond association and dissociation were detected by monitoring the real-time changes in thermal fluctuations of the probe bead. The assay stems from the idea that bond association results in adding a molecular spring to the probe bead in parallel to the RBC spring, thereby reducing the amplitude of its thermal fluctuations. Bond formation and bond dissociation can therefore be detected from the reduction and resumption in thermal fluctuations, which were measured by the sliding standard deviation of 90 data points from the time sequence. Our high-speed camera can acquire images at 1,500 Hz, sufficient to resolve fast kinetics. As exemplified in Figure 5-1 C and D, the smaller standard deviation indicates the bound state (*red* in Figure 5-1 C) while the larger one indicates the unbound state (*blue* in Figure 5-1 C). The period from the instant of dissociation of an existing bond to the instant of association of the next bond, termed waiting time t_w, contains cellular on-rate (k_{on}^c) information because the faster the on-rate, the shorter the expected waiting time. The binding specificity was confirmed as GC-

bearing target beads adhered at significantly higher frequencies to probe beads coated with A1 than those without A1 (Figure 5-1 E), and adding anti-A1 and anti-GPIbα mAbs was observed to abolish the adhesion (Figure 5-1 F) and reduced the cellular on-rate to negligible level (Figure 5-1 F).
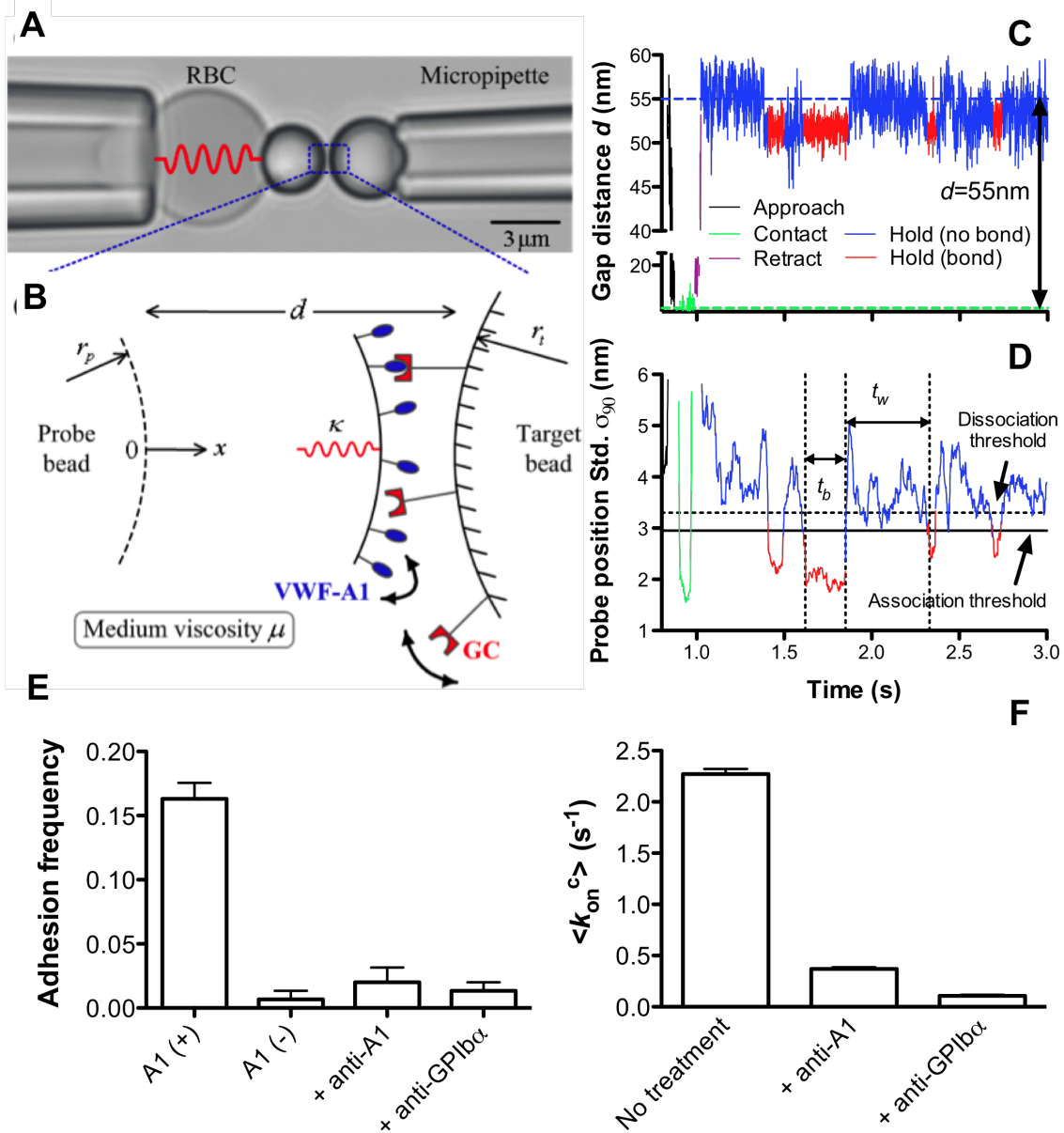
Figure 5-1. BFP thermal fluctuation assay with controlled separation. A, Photomicrograph

84

of a measurement. (A) micropipette-aspirated red blood cell (RBC), with a bead (*left*, termed "probe" in B, radius: r_p) attached to its apex, was aligned with an opposing bead (*right*, termed "target" in B, radius: r_t) aspirated by another micropipette. The target bead was precisely controlled by a piezoelectric translator to contact the probe bead, retract and be held stationary at a certain position. The gap distance between the two beads was tracked through image analysis software to derive the data in C and D. (B) Schematic of bond association process in the assay. VWF-A1 and glycocalicin (GC) were covalently coupled to the probe bead (*left*) and the target bead (*right*), respectively. The gap distance between the bead apices is d initially, and the combined molecular length l sets a contact threshold for possible bond formation. When d is larger than l, bond association has to involve probe bead diffusion under the constraint of RBC linkage (spring constant: κ) for a nonzero contact area. The process of bond formation is therefore modeled as two essential steps: one dimensional diffusion of receptor-bearing probe bead in the presence of a harmonic potential, and receptor-ligand reaction between the opposing surfaces in close proximity. Schematic is not drawn to scale. (C) A representative test cycle of gap distance d vs. time t from the thermal fluctuation assay measured at 1,500 Hz. In each cycle, the target bead first approached the probe bead (black), stayed in contact for 0.1 s (green), retracted (purple), and was held in space (blue/red). (D) Plot of sliding standard deviation (Std.) of 90 consecutive points (σ_{90}) of the probe position in (C) vs. time t. Horizontal lines represent the threshold values to identify bond association (solid line) and dissociation (dashed line) events. Bond and no-bond states were distinguished in red and blue segments, respectively. (E) Adhesion frequencies between target beads coated with GC and probe beads coated with A1 (A1(+), first column), without A1 (A1(-), second column), with A1 plus 50 μg/ml anti-A1 blocking mAb 5D2 (+anti-A1, third column), and with A1 plus 50 μg/ml anti-GPIbα blocking mAb AK2 (+anti- GPIbα, fourth column). Binding frequencies, presented as the means ± S.E.M., were measured from three probe-target pairs per condition and each probe-target pair was tested repeatedly for 50 contact-retract cycles. (F) Averages (± S.E.M.) of cellular on-rates $<k_{on}^c>$ under indicated conditions (see section 2.5.3).

5.2.1 *2D kinetics dependence of separation distance*

For bond formation to occur, a receptor and a ligand have to contact each other, requiring the separation distance between reactant-bearing beads to be sufficiently small. To quantify how the VWF–GPIbα binding kinetics depends on the separation distance, we varied the gap distance (d) between the opposing bead surfaces in the range 20-80 nm. At each fixed value of d, waiting times for bond association to occur were collected and analyzed by survival frequencies (Chen et al., 2010). The survival frequencies at different gap distances all distributed exponentially as they aligned well along straight lines in semi-log plots (Figure 5-2 A), suggesting that the A1–GC interactions in this BFP setup

85

can be modeled by the first-order kinetics of irreversible single-bond association (Equation 2-2 and 2-3), independent of the separation distance.

Figure 5-2. Dependence of 2D association kinetics on gap distance. (A) The natural log of survival frequency, calculated as the fraction of measurements with a waiting time $>t_w$, was plotted vs. t_w for the indicated values of gap distance and fitted by solid lines. (B) Estimated 2D effective on-rate $<A_c k_{on}>$, calculated from the negative slopes of the linear fits in (A), was plotted against the gap distance d. The effective on-rates were calculated by dividing the cellular on-rates by the product of the protein densities on the probe (A1, ligand) and target (GC, receptor) beads, i.e. $m_r m_l = 1.96 \times 10^5 \, \mu m^{-4}$ determined by flow cytometry (see section 2.8). (C and D) Plots of average waiting times $<t_w>$ (C) and bond lifetimes $<t_b>$ (D) vs. gap distance d (x-axis in converted force is also shown for D). The error bars represent S.E.M. All the data were obtained at a fixed value of BFP spring constant ($\kappa = 0.15$ pN/nm). For each given d, an ensemble of 20~40 waiting times or bond lifetimes were pooled.

The cellular on-rate (k_{on}^c) (Yago et al., 2007), defined as the probability for a target bead to adhere a probe bead per unit time, could be represented by fitting the waiting time distribution by a straight line (Chen et al., 2008a), whose negative slope

represents an estimate of k_{on}^c (Figure 5-2 A). According to the mass-action effect of receptors and ligands on the contact area (Yago et al., 2007), the cellular on-rate can be further depicted as $k_{on}^c = m_l m_r A_c k_{on}$, where k_{on} is the molecular on-rate of dimension [area][time]$^{-1}$ that characterizes the rate for a receptor to associate a ligand per molecular density; A_c is the contact area; m_l and m_r are the site densities of proteins on the probe bead (A1, ligand) and target bead (GC, receptor) respectively. For similar sizes of beads, A_c can be considered as a constant. Thus, we took out the mass action from cellular on-rate by dividing $m_r m_l$ and used the $A_c k_{on}$ as the effective 2D on-rate to reflect the kinetic properties of protein chemistry.

Because the longer the separation distance is, the fewer a chance for a receptor to find a ligand, we expected a lower on-rate and a longer waiting time. We found that as d increased from 30 nm to 80 nm, the effective on-rate estimate $<A_c k_{on}>$, the slopes of best-fits from the distributions (Figure 5-2 A), dropped 12 folds from 14.8 to 1.2×10^{-6} $\mu m^{-4} s^{-1}$ (Figure 5-2 B). The measured average waiting time $<t_w>$, the inverse metric of $<A_c k_{on}>$, increased from 0.3 s to 5.2 s (Figure 5-2 C). Note that as d continuously increased above 80 nm that exceeds the combined length of GC (Fox et al., 1988) and VWF-A1 (Varughese et al., 2002) (l in Figure 5-1 B), the binding was completely abolished: no bond events can be observed for the test cycles after a adhesion-free separation; for the test cycles in which bond forms during the contact phase, the waiting time to next bond formation was out of the measurable time window after the separation.

The average bond lifetime $<t_b>$, reciprocal of bond dissociation off-rate (k_{off}), also changed with d: $<t_b>$ decreased from 1.77 to 0.17 s as the gap distance d increased from 23.6 nm to 80.4 nm (Figure 5-2 D). Consider the estimated bond force $f = kd$, this suggests the force plays a major role in facilitating bond dissociation as the separation becomes significant. With d being converted into the force, the monotonic decreasing trend of d-t_b curve is consistent with our previously observed A1–GPIbα low slip-bond regime (<16pN, Figure 4-2 A) (Ju et al., 2013b), in which force accelerates bond dissociation. Thus, the lifetime data here suggested that lengthening the gap distance exerts more force on the A1–GC bond.

5.2.2   2D kinetics dependence of Brownian motion

Due to its small size, the BFP is susceptible to thermal excitations that cause Brownian motion, which contributes to the fluctuations of the probe bead. The Brownian motion determines the frequency of discontinuous contacts between different portions of the opposing surfaces. A more significant effect is expected when the separation distance gets bigger. Since the BFP spring constant defines the steepness of the harmonic energy well where the Brownian motion of the BFP probe bead is confined, we investigated how Brownian motion regulates the binding kinetics by tuning the BFP spring constant κ. According to the calibration method (Equation 2-1), we varied the κ by changing the RBC aspiration pressure. We found that at $d = 50$ nm, as κ increased from 0.15 pN/nm to 0.4 pN/nm, waiting time distribution rightshifted to the higher regime (Figure 5-3 A) and $<A_c k_{on}>$ decreased from 10.1 to 6.7×10^{-6} $\mu m^{-4}s^{-1}$ by 1.5 fold (Figure 5-3 B). With a larger separation, at $d = 75$ nm, $<A_c k_{on}>$ became more sensitive to κ, decreasing from 2.4 to 0.5 $\times 10^{-6}$ $\mu m^{-4}s^{-1}$ by 5 fold. It suggested that decreasing BFP spring constant strengthens the

confinement, making it easier for receptors on the BFP probe bead to bind ligands on the
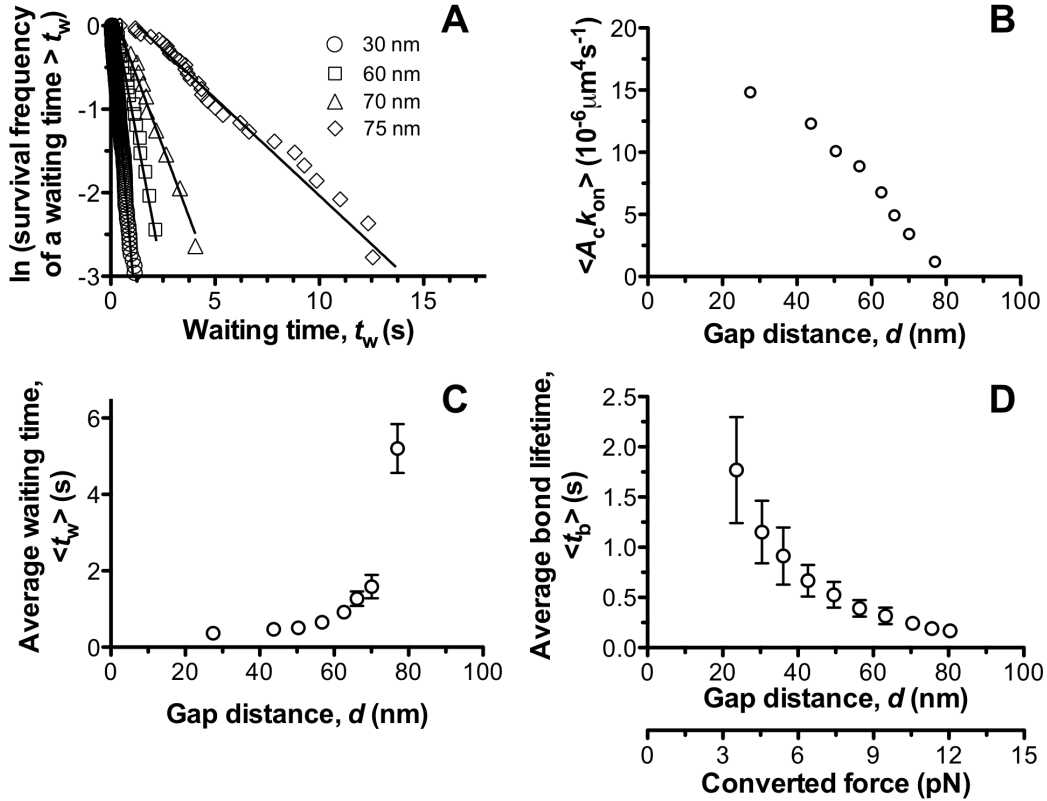
target bead.
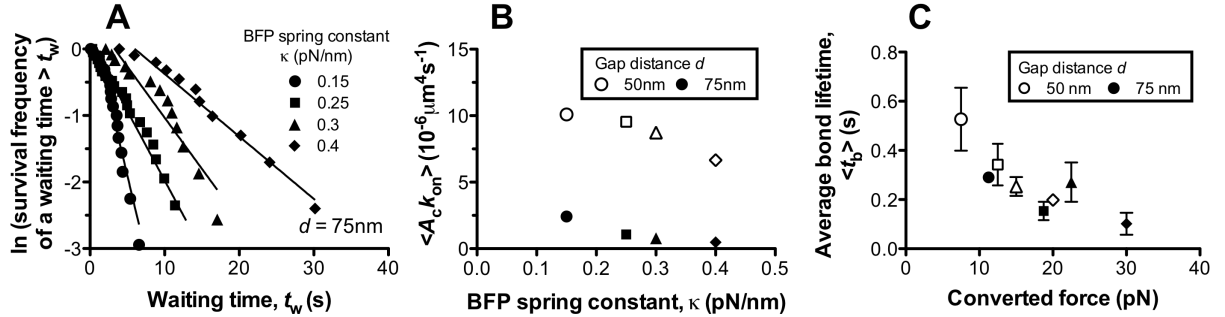
Figure 5-3. Dependence of 2D association kinetics on BFP stiffness. (A) The natural log of waiting time survival frequency, calculated as the fraction of measurements with a waiting time $>t_w$, was plotted vs. t_w for the indicated BFP spring constant κ and fitted by solid lines. (B) Estimated 2D effective on-rate $<A_c k_{on}>$, the negative slopes of the best-fits in (A), were plotted vs. κ. The data were obtained at two fixed gap distances, $d = 50$ and 75 nm respectively. The adjustment in κ was achieved by varying the aspiration pressure in the micropipette. (C) Plots of the average bond lifetimes $<t_b>$ vs. force. Solid or empty symbols of various types are used to represent conditions of different κ and d through A to C. The error bars represent S.E.M. For each κ group, an ensemble of 10~30 waiting times or bond lifetimes were pooled.

In contrast to the waiting time dependency, as κ increased from 0.15 to 0.4

pN/nm, the bond lifetime $<t_b>$ decreased from 0.52 to 0.19 s at $d = 50$nm; from 0.29 to

0.10 s at $d = 75$nm (Figure 5-3 C). Remember that the pulling force on bonds is exerted

via the stretched BFP, plotting the $<t_b>$ measured at different κ and d against the

converted force f showed the same slip-bond force dependency (Figure 5-3 C) as observed

in Figure 5-2 D. The only exception was made at $\kappa = 0.3$pN/nm, $d = 75$nm and $f = 22.5$

pN, which can be explained by the A1–GPIbα catch bond by which force prolongs the

bond lifetime at forces 16-25 pN (Figure 4-2 A) (Ju et al., 2013a).

5.2.3   2D kinetics dependence of diffusion

As schematically shown for the engagement of one receptor and one ligand (Figure 5-1 B), the binding sites of VWF-A1 and GC can undergo diffusions from two different sources: 1) Bead diffusion. Although portions of the molecules are anchored to the respective bead surfaces, the bead, especially the probe, is still subject to the diffusion in BFP chamber media, thereby the carried molecules also diffuse together. 2) Molecular diffusion. The receptor and ligand are also subjected to rotational diffusion, which orients their binding sites for molecular docking.
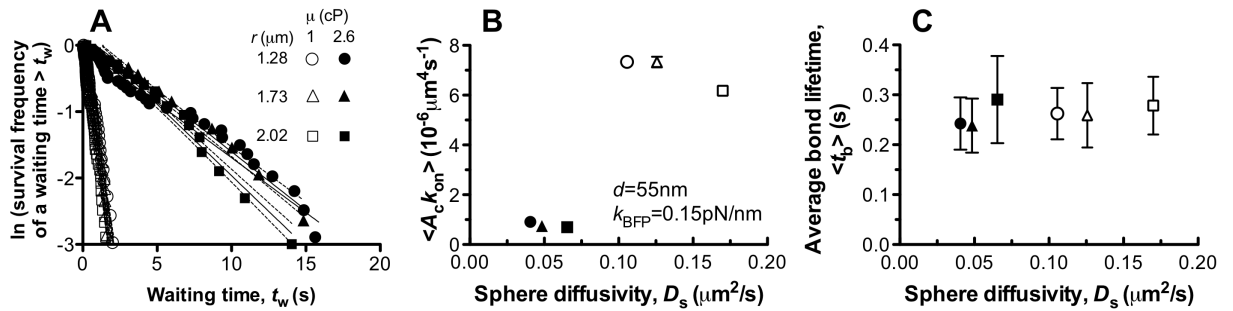
Figure 5-4. Dependence of 2D association kinetics on diffusivity. (A) The natural log of waiting time survival frequency, calculated as the fraction of measurements with a waiting time $>t_w$, was plotted vs. t_w for indicated microsphere diffusivity (D_s) and fitted by solid lines. The data were obtained at $d = 55$ nm, $\kappa = 0.15$ pN/nm, and different values of D_s by varying the probe bead radius (r_p) or medium viscosity (μ). To increase the medium viscosity in some experiments, 6% (w/v) of Ficoll were added to the media. The values of medium viscosity were independently measured as 1.0 and 2.6 cP at room temperature for 0 and 6% Ficoll, respectively. (B) Estimated 2D effective on-rate $<A_c k_{on}>$, calculated from the negative slopes of the fitting lines to data in (A), was plotted vs. D_s. D_s is defined by the Stokes-Einstein relationship. (C) Plots of average bond lifetimes $<t_b>$ vs. D_s. For each D_s group, an ensemble of 20~50 bond lifetimes were collected.

In light of the unconfined spherical diffusivity Stokes-Einstein definition (Eq. 4), we investigated the effects of diffusivity by varying the probe bead radius r_p or the buffer viscosity μ. We added 6% (w/v) of Ficoll to the media to increase the media viscosity (Yago et al., 2007) in some experiments while keeping $d = 55$ nm and $\kappa = 0.15$ pN/nm constant. The results showed that increasing μ from 1 to 2.6 cP significantly rightshifted

the waiting time distribution (Figure 5-4 A) and reduced $<A_c k_{on}>$ from 6.2 to 0.7 $\times$ 10^{-6} $\mu m^{-4} s^{-1}$ by ~9 fold (Figure 5-4 B). However, varying the bead parameter r_p had little impact on waiting time distributions (Figure 5-4 A) and $<A_c k_{on}>$ (Figure 5-4 B). This result may be explained by the cancellation of two opposite effects when r_p was increased: increase in contact area A_c but decrease in k_{on} by spherical diffusivity. This also suggested that the spherical diffusion is quite limited due to the BFP aspiration. Besides, we found that the media viscosity affected molecular diffusion much more than BFP probe bead Brownian motion, suggesting that rotational diffusion plays a major role to allow interacting molecules to properly orient their binding pockets for docking. By comparison, the diffusion parameters had no influence on the average bond lifetimes (Figure 5-4 C).

5.3 Discussion

The goal of the current study is to characterize the physical regulation of the 2D kinetics of receptor–ligand interactions quantitatively. We improved the BFP thermal fluctuation assay to visualize the bond formation of A1–GC interaction at controllable physical factors: d, κ, r_p and μ. Thanks to the soft stiffness of the RBC, the unbinding–binding transition can be observed for all used κ. At the experimental contact time setting (0.1s), the adhesion frequency of the non-specific binding was ~1% and much lower than that of the specific binding frequency around 16% (Figure 5-2), which guaranteed that most of the observed events were from single bond interactions (Zhu et al., 2002).

The transport mechanism was found to regulate the flow-induced selectin–ligand bond formation (Yago et al., 2007). In our BFP set-up, however, no shear flow is required, and A1–GC bond formation was governed by receptor–ligand separation

distance (Figure 5-2), Brownian motion of the carrier (Figure 5-3) and the molecular diffusion (Figure 5-4). This simplifies the bond association process by ignoring the transport mechanism of sliding velocity. More importantly, such the thermal fluctuation assay enables to dissect the competing regulatory mechanisms on association kinetics of surface-bound receptor–ligand interactions.

On the other hand, the dissociation of VWF–GPIbα bond has been intensively studied (Doggett, 2003; Kumar et al., 2003; Yago et al., 2008). Recently, using the force-clamp assay, we observed a triphasic force-dependent VWF–GPIbα dissociation kinetics: force first shortens (slip), then prolongs (catch), and finally shortens (slip) the bond lifetimes as force increases (Figure 4-2 A) (Ju et al., 2013b). The average bond lifetime measurements from the thermal fluctuation assay in present study showed a similar triphasic behavior (Figure 5-2 D). Considering the force exerted via the BFP is determined by κ, we also measured the dependence of $<t_b>$ on κ at fixed gap distances of the slip regimes. Plots of $<t_b>$ vs. κ showed that the increase of BFP spring constant decreased the bond lifetime, suggesting slip-bond force regulations. These data indicated that force induced by separation enlargement facilitates the short-lived dissociation state, which matched the results by the force-clamp assay. However, other than d and κ, all other physical factors of the transport mechanism have no effect on bond lifetimes. Our results suggested that the on-rate is regulated by transport and the off-rate is regulated by force.

In summary, we have studied the coupling process of physical transport and biochemical reaction that regulate bond association between VWF-A1 and glycocalicin, which mediates platelet tethering and rolling on vascular surfaces. We have tested three physical factors: surface separation d, tethering stiffness κ, and medium viscosity μ that regulate the receptor–ligand association and govern three distinct steps of transport mechanism: tethering of platelet to the vascular surface, Brownian motion of the platelet, and rotational diffusion of the interacting molecules. Together, the present single-bond level characterization of GPIbα-VWF association provides fundamental understanding of the physical regulation in platelets adhesion on vascular surfaces and reveals generic feature of transport-governed bond formation for other receptor–ligand interactions.

CHAPTER 6: VWF–GPIB-ALPHA CATCH BOND TRIGGERS PLATELET SIGNALING BY FORCE PROLONGED BOND LIFETIMES

This chapter of work was equally contributed by Yunfeng Chen.

6.1 Introduction

In current view, under conditions of rapid blood flow, as occurs in arterioles or atherosclerotic arteries with restricted lumen, the initiation of platelet adhesion following vascular injury features a two-step cascade: 1) Fast tethering of platelets to the site of vascular injury mediated by binding of GPIbα to the VWF-A1 immobilized on collagens. However, A1–GPIbα interaction can only support translocation (rolling) of platelets with stop-and-go motion due to its rapid on-/off-rate (Savage et al., 1996; Yago et al., 2008; Ju et al., 2013a). 2) Stable adhesion mediated by different integrins, including $\alpha_{IIb}\beta_3$ bound to the Arg-Gly-Asp (RGD) motif in the VWF-C1 domain (Savage et al., 1996; 1998; Keuren et al., 2004) or fibronectin (FN). Activated $\alpha_{IIb}\beta_3$ immobilizes the plasma proteins, mainly VWF and fibrinogen, on the surface of adherent platelets that propagate the thrombus formation through crosslinking (Ruggeri et al., 1999).

It has been well accepted that GPIbα transduces signals necessary for integrin $\alpha_{IIb}\beta_3$ upregulation independently (Kasirer-Friede et al., 2004; Ruggeri and Mendolicchio, 2007). In detail, VWF–GPIbα engagement leads to intracellular calcium (Ca^{2+}) elevations featured by a short-time Ca^{2+} peak (termed type α/β peak), which appears to have been initiated by mechanical stimulation via GPIbα and triggers reversible $\alpha_{IIb}\beta_3$ upregulation or called "low level activation" (Mazzucato et al., 2002; Nesbitt et al., 2002). The upregulation of $\alpha_{IIb}\beta_3$ primes its binding affinity to ligands (i.e. VWF), which facilitates

platelets firm adhesion and triggers a secondary stage of Ca^{2+} signal, featured by Ca^{2+} influx from extracellular environment and a more oscillated and sustained signal pattern, although specific pattern characterization and triggering pathway of which still remain controversial (Mazzucato et al., 2002; Nesbitt et al., 2002; 2003).

A body of evidences suggests that GPIbα is a mechanosensor, indicating a direct linkage between GPIbα adhesion function and its signaling function (Mazzucato et al., 2002; Nesbitt et al., 2002). However, it remains unknown on how a mechanical stimulus is translated to biochemical events that activate platelets through VWF–GPIbα axis. Moreover, a study on a A1 mutant of type 2B VWD, in which the VWF mutation causes an increased affinity for GPIbα but results in paradoxical bleeding disorder (Ruggeri, 2004), suggested the significance of understanding the relationship between GPIbα adhesion function and its signaling function. This shear-induced platelet aggregation study has shown that the binding of 2B VWF (V1316M) to GPIbα did not activate the $\alpha_{IIb}\beta_3$ and led to unstable thrombus formation compared with the binding of WT VWF (Mekrache et al., 2003). This raises the question whether GPIbα-mediated mechanotransduction can be altered by the single-residue VWD mutation? In other words, is VWD a signaling disease in addition to its deficiency in adhesion?

The biophysical mechanism by which GPIbα transduces signals still remains controversial. Three major limitations of widely used population approaches (such as cone-and-plate viscometers (Kuwahara et al., 1999), flow chambers (Mazzucato et al., 2002; Nesbitt et al., 2002) and microfludics devices (Nesbitt et al., 2009)) may explain the problem: 1) low temporal and spatial resolutions; 2) insufficient capabilities for direct

kinetic characterization of molecular interactions on the single-molecule level and 3) unable to sync the adhesion and signaling observations. To understand GPIbα signal triggering by force, we analyzed *in situ* force regulation of VWF–platelet GPIbα interactions using a BFP (Ju et al., 2013b). This new method provides a clean system to manipulate a single platelet with delicate control of the force and timing of ligand–platelet contact/separation. With concurrent Ca^{2+} imaging, we simultaneously observed Ca^{2+} signals in live platelet induced by force applied via VWF ligands or antibodies interacting with the platelet surface GPIbα. This allowed us to delineate the relationships among force attributes, bond characteristics and signaling outcomes, thereby defining the role of mechanical properties in the early-stage platelet adhesion to provide new insights on GPIbα signal transduction, VWF ligand discrimination, platelet activation, and thrombus formation.

6.2 Results

To expand the studies of the purified systems in Chapter 4 (Figure 4-4), here we measured GPIbα bond lifetimes on a fresh human platelet under a broader range of constant forces applied (Figure 6-1 A). To focus on the VWF–GPIbα interaction only, the recombinant A1 domains in monomer (mA1, the 1238-A1, see section 2.1 and Chapter 4) (Yago et al., 2008; Ju et al., 2013a) or dimer (dA1, the 1208-A1, see section 2.1) (Mazzucato et al., 2002; Kasirer-Friede et al., 2004) were used (Figure 6-1 B). Platelet BFP experiments were done in repetitive cycles similarly as before mentioned, except that 2 s contact time was used for the force-clamp assay (Figure 6-1 C and D) and 0.1-5 s was used for the adhesion frequency assay. To ensure that most binding events were mediated by single bonds, adhesion frequencies were kept low (<25%) by adjusting the

ligand density on the probe bead (Chesla et al., 1998; Zhu et al., 2002; Ju et al., 2013a)(Figure 6-1 E). Platelet adhesion was not detected when probe beads were coated with SA as an isotype control, demonstrating the binding specificity (Figure 6-1 E).
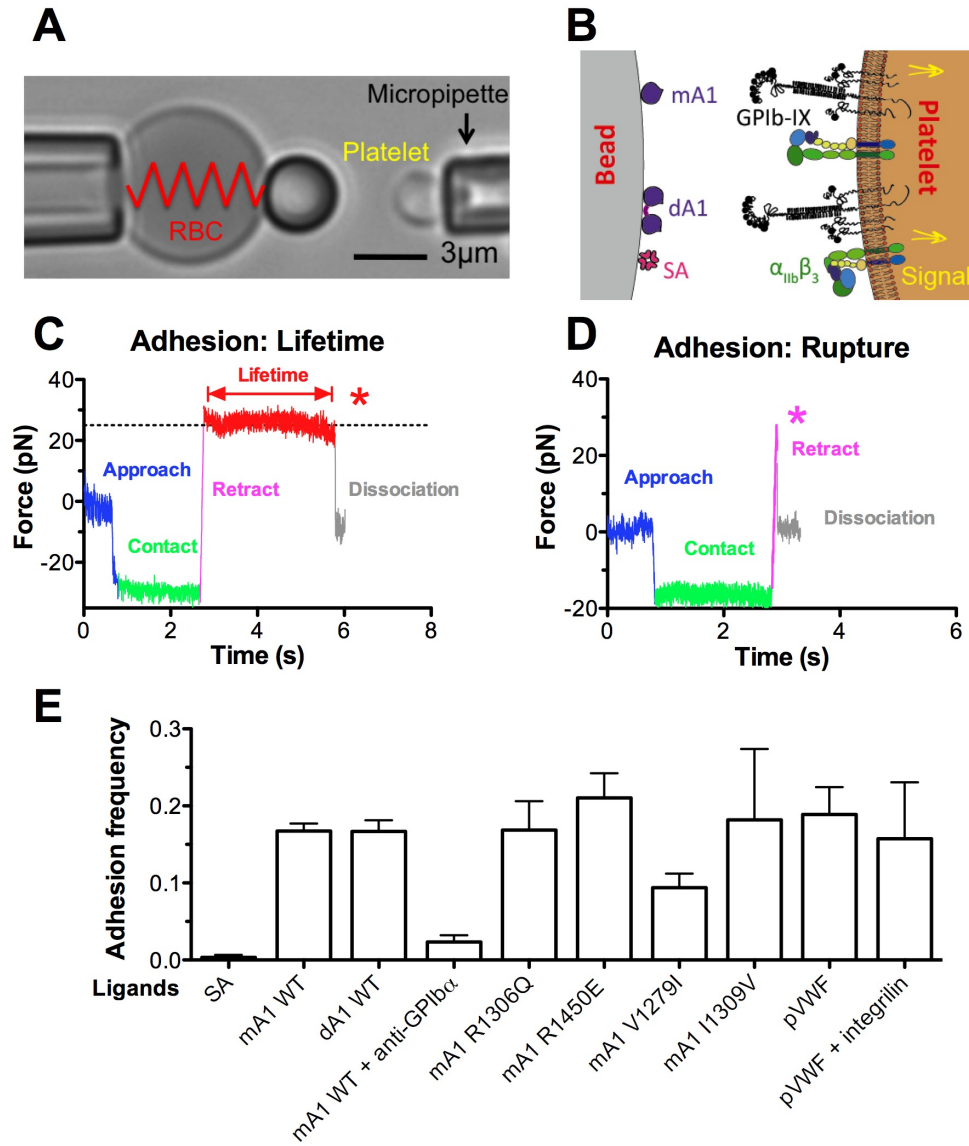
Figure 6-1. *In situ* **analysis of force-dependent VWF–platelet GPIbα bond kinetics by BFP.** (A) Platelet BFP micrograph. A micropipette-aspirated RBC with a probe bead attached to the apex (*left*) was aligned against a platelet held by an apposing micropipette (*right*). (B) Platelet BFP functionalization. The probe bead was covalently linked to streptavidin (SA) and VWF ligands: wild-type (WT) or mutant VWF-A1s in monomer (mA1) or dimer (dA1), or pVWF (*left*). SA is for attachment of the bead to biotinylated RBC, VWF ligand is the focus for interaction with platelet GPIbα (*right*). (C and D) Force *versus* time traces from three representative test cycles. A platelet was driven to approach a probe (blue), contacted (green) and

retracted (magenta). If adhesion was detected, the platelet was either survived ramping and held (red) at a preset force (marked by *) until dissociation (gray), enabling bond lifetime measurement (by force clamp assay, see section 2.5.3) (C), or was ruptured by a ramp force (marked by *) denying bond duration (D). (E) Binding specificity. Mean ± S.E.M. of adhesion frequencies of >3 bead–platelet pairs with 50 contacts for each. Platelet rarely adhere to beads coated with SA only but adhered to those coated with VWF ligands at densities adjusted to achieve <25% adhesion.

6.2.1 *Platelet GPIbα forms catch bonds with VWF–A1*

VWD mutations have been found to change the mechanical regulation of platelet adhesion, resulting in the bleeding (Ruggeri, 2007). From biological characterizations, a type 2B VWF mutant shows a GOF phenotype that binds to platelets instantaneously with lower ristocetin or shear requirement (Matsushita and Sadler, 1995); while a type 2M mutant shows a LOF phenotype that binds to platelet ineffectively with higher ristocetin or shear requirement (Rabinowitz et al., 1992; Morales et al., 2006). From a biophysical perspective, these mutations alter VWF–GPIbα binding kinetics. Off-rates of VWF–GPIbα dissociation can be estimated from the reciprocal average bond lifetimes (see section 4.2.1, (Ju et al., 2013a)). With the platelet BFP data, we found that at low force 10 pN, two 2B A1 mutants (R1450E and I1309V) showed longer bond lifetimes while a 2M mutant (V1279I) showed the shorter the bond lifetime (Figure 6-2 A, open bar), matching their biological phenotypes.

Previously, we used the both single-molecule (AFM and BFP) and population assays to show a counterintuitive phenomenon called catch bond, in which force may prolong A1–GPIbα bond lifetime (see section 4.2.1)(Yago et al., 2008; Ju et al., 2013a). Instead of using the GPIbα from purified systems: glycocalicin or GPIbα captured from platelet lysates (Figure 4-4), we systematically investigate the A1–GPIbα interaction with native GPIbα on a platelet. Again, we observed triphasic force-accelerated (slip), then force-decelerated (catch) and force-accelerated (slip) dissociation of platelet GPIbα from

wild-type (WT) mA1 (Figure 6-2 B, ○), which confirmed our previous results but with a native system and a bigger force measurement regime. Interestingly, the 2M mutant V1279I also showed the catch bond but with much globally lower lifetimes, which suggests the global binding defect as its LOF phenotype (Figure 6-2 B, △). By comparison, two 2B mutants R1450E (Figure 6-2 B, □) and I1309V (Figure 6-2 B, ◇) form slip bonds with monotonically decreased bond lifetimes as force increases, which also matches previous observations (Yago et al., 2008; Ju et al., 2013a). However, as force continues to increase above 10 pN, force resistance of R1450E rapidly drops and becomes much lower than WT at >25 pN while that of I1309V drops much slower and remains similar level to WT at >25 pN (Figure 6-2 A and B). The force-dependency differences among 2B mutants suggest different signal triggering and pathological function although they are all classified under the 2B category.
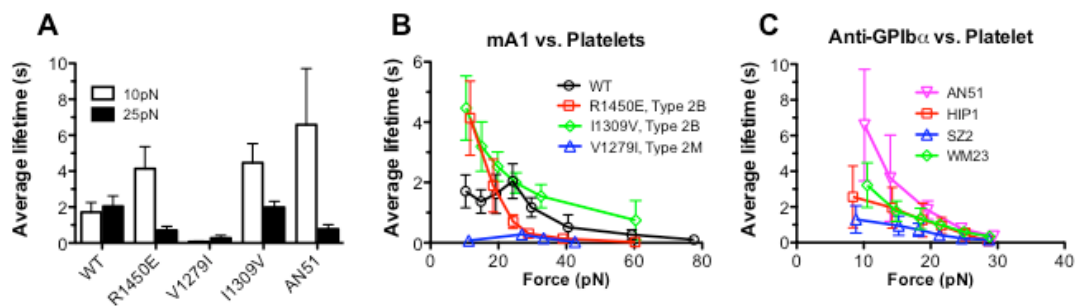
Figure 6-2. Platelet GPIbα forms ligand-specific catch-slip bond. (A) Lifetimes of bonds of platelet GPIbα with probe beads coated with indicated VWF-A1 or anti-GPIbα mAb ligands at 10 (white) and 25 (black) pN. (B and C) Lifetime vs. force curves showing that platelet GPIbα formed catch-slip bonds with WT (○) and 2M mutant V1279I (△) mA1s, but slip-only bonds with 2B mutant R1450E (□) and I1309V (◇) mA1s (B); also slip-only bonds with all used anti-GPIbα mAbs AN51 (▽), HIP1 (□), SZ2 (△) and WM23 (◇) (C).

Catch bonds are specific characteristics of the A1–GPIbα system; Pulling the GPIbα with anti-GPIbα mAb only shows slip bonds (Figure 6-2 C). Our results reaffirm

catch bonds as a mechanism for mechanical regulation of VWF activation by the GPIbα (Ju et al., 2013a). The A1–GPIbα bond lifetime depends on force biphasically, with maxima at 25 pN as the optimal force (Figure 6-2 B). At this force level, however, the 2B mutant R1450E and anti-GPIbα mAbs cannot stabilize the interaction with platelet GPIbα, which reversed the relative lifetime trend at lower force 10 pN (Figure 6-2 A). Thus, force delicately balanced the initial platelet adhesion through the A1–GPIbα catch bond mechanism.

6.2.2   *Optimal force triggers Ca^{2+} by prolonging A1–GPIbα lifetime via catch bond*

To evaluate how the force-regulated VWF dissociation from and ligand discrimination by the GPIbα relates to platelet signaling, we added a fluorescence optical path to our BFP (fBFP, Figure 3-6) and measured simultaneously bond lifetime and Ca^{2+} flux (Figure 6-3, see sections 2.7 and 3.4). In these experiments, the measurement cycle was repeated for 5 min for each pair of platelet and probe bead. Concurrently, intracellular Ca^{2+} concentration was continuously observed with fura-2 ratiometric imaging. Two types of Ca^{2+} signals were observed. Type α curves have an initial latent phase of 1-2 min before fura-2 ratio rapidly increased by >150% of initial baseline and then decayed (Figure 6-3 A and B). Type β curves stayed near the baseline or gradually increased to a modest level (Figure 6-3 B and D). To examine how various attributes of force impact platelet triggering, we analyzed their correlations with the maximal percent Ca^{2+} increase. Note that our experiments differ from previous studies (Kuwahara et al., 1999; Mazzucato et al., 2002; Nesbitt et al., 2002; 2003) in that Ca^{2+} was induced by intermittent single A1–GPIbα bonds formed infrequently and sequentially (Figure 6-3 B and D) in the absence of any other receptor–ligand engagement. While Ca^{2+} can certainly

be induced under more favorable conditions (Kuwahara et al., 1999; Mazzucato et al., 2002; Nesbitt et al., 2002; 2003; Mazzucato et al., 2009), our rigorous conditions allow determination of the minimum requirements for Ca^{2+} induction.
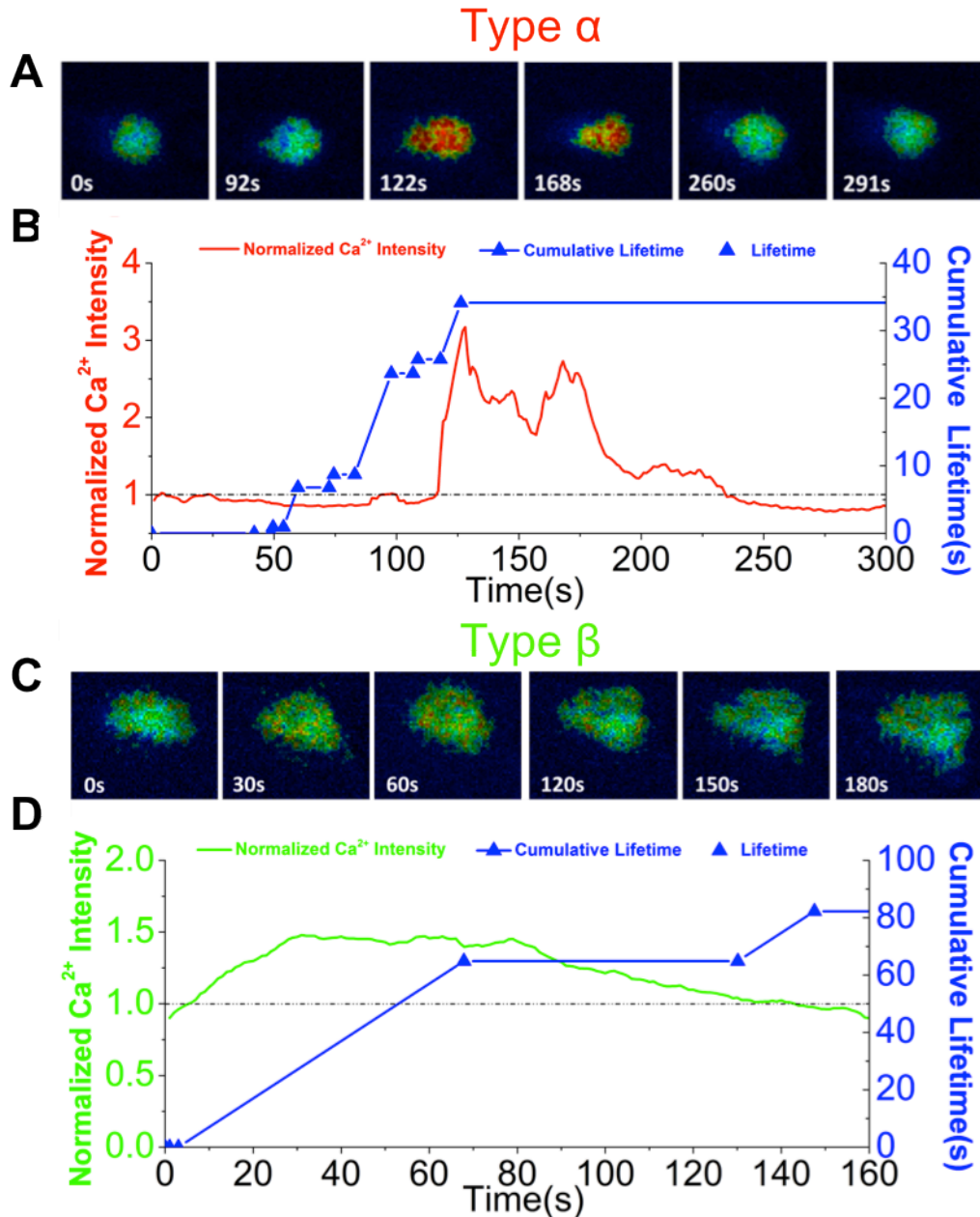
Figure 6-3. Single-platelet concurrent measurement of Ca^{2+} mobilization and *in situ* A1-platelet GPIbα adhesion history. (A and C) Representative widefield pseudo-colored images of

two types of intracellular Ca^{2+} signals in two platelets at indicated times. Type α has an initial latent phase followed by a >50% rapid increase at the peak. Type β has a <50% gradual increase. (B and D) Representative time courses of relative fura-2 ratio of type α (B, red curve, left ordinate) or type β (D, green curve, left ordinate) intracellular calcium signal synchronized with concurrent measurement of bond lifetime (▲) events and the cumulative lifetime (blue curve, right ordinate).

Force-clamp cycles that mimicked the scenario when a platelet translocates over the immobilized VWF and allowed measurable lifetimes of the A1–GPIbα bond lifetimes (Figure 6-1 C) resulted in robust Ca^{2+} (Figure 6-4 A, □). In contrast, force-ramp cycles that ruptured the bond without holding it for a defined lifetime (Figure 6-1 D) generated only baseline Ca^{2+} (Figure 6-4 A, ■) which is similar to the negative control using a SA-coated bead to touch the platelet (Figure 6-4 A, ◇) that produced little binding (Figure 6-1 E). The calcium triggering was ligand-dependent: pulling via a LOF A1 mutant V1279I (type 2M) using the same force-clamp cycles failed to induce Ca^{2+} (Figure 6-4 A, ▽). The triggering was also GPIbα-specific as pulling GPIbβ via an antibody did not trigger Ca^{2+} despite much longer bond lifetimes (Figure 6-4 A, ○). That calcium was triggered by A1WT but not LOF A1 (Figure 6-4 A) might be due to a longer lifetime of GPIbα bond with A1WT than with the LOF mutant under force (Figure 6-2 B). We therefore examined the correlation of, or the lack thereof, calcium signals and bond lifetimes by measuring Ca^{2+} at 10, 25, 40 and 60 pN with force-clamp cycles using either WT or GOF mutant (R1450E) mA1 to form serial bonds with GPIbα on platelets. The biphasic calcium vs. force pattern matched the catch-slip bond lifetime vs. force pattern for A1WT (Figure 6-4 B), showing a positive correlation between platelet signaling and A1–GPIbα bond lifetime; while the monotonic calcium vs. force pattern matched the slip-only bond lifetime vs. force pattern for R1450E A1 (Figure 6-4 C), suggesting that similar correlation between calcium and GPIbα bond lifetime is applied to both WT and mutant

A1s. Remarkably, at A1WT optimal force 25 pN, the maximal calcium was observed for A1WT while the low level calcium was observed for A1R1450E. This was probably due to the rapid dropping of A1R1450E bond lifetime to near zero level (much shorter than that for A1WT) as force increases from 10 to 25 pN (Figure 6-4 B and C). Taken together, these data demonstrated that force induces calcium signaling (triggering), which has an optimal magnitude for maximal triggering and has to be applied to the GPIbα for a sufficient duration. These results provide further support to the hypothesis that the ligand-specific catch bonds may provide a mechanism for ligand discrimination as A1WT allows optimal force to be exerted on the GPIbα for a prolonged period to trigger platelet signaling, while GOF or LOF A1 mutations did not.

A

B mA1 WT

C mA1 R1450E (GOF)

104
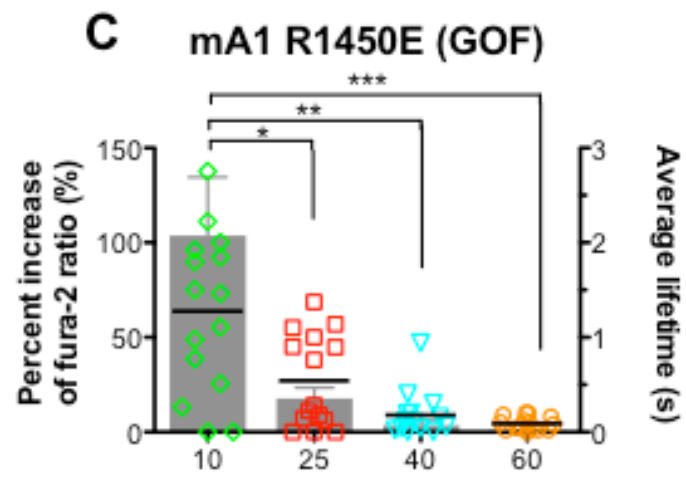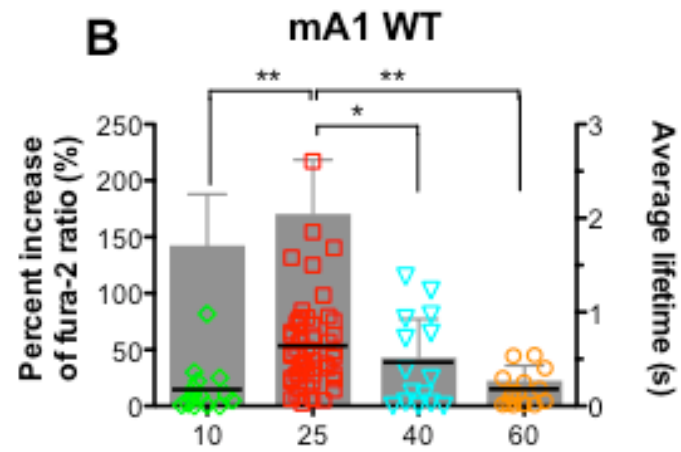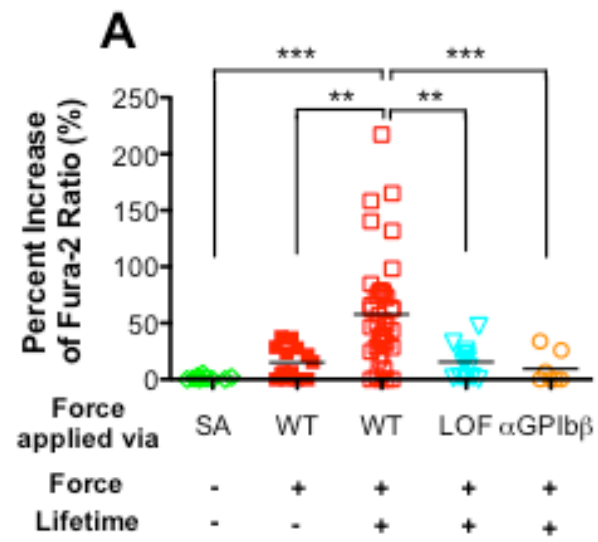
Figure 6-4. GPIbα- and A1-specific Ca^{2+} flux requires both force and lifetime. (A) Ca^{2+} flux requires durable force on GPIbα bond applied by VWF-A1. The Ca^{2+} flux is represented by the percent increase of fura-2 ratio (from the initial value to the maximum, Figure 6-3 B) and measured without force or lifetime via control ligand SA non-specific bond ($\diamondsuit$), with force but no lifetime via mA1 bond ($\blacksquare$, Figure 6-1 D), or with both force and lifetime (Figure 6-1 C) via platelet GPIbα engaged with mA1 WT ($\square$) or LOF mutant V1279I ($\triangledown$) or via GPIbβ–anti-GPIbβ bond ($\bigcirc$). (B–C) Ca^{2+} was triggered by an optimal force. Percent increase of fura-2 ratio (points, left ordinate) triggered by platelet GPIbα –mA1 WT (B) or GPIbα –mA1 R1450E (C) bond lifetimes (grey bars, mean ± S.E.M. of >30 measurements, right ordinate) were measured at 10 ($\diamondsuit$), 25 ($\square$), 40 ($\triangledown$), or 60 ($\bigcirc$) pN force. * = p < 0.05; ** = p < 0.01; *** = p < 0.001, assessed by unpaired, two-tailed Student's t-test.

6.2.3   *Ca^{2+} triggering amplitude correlates with duration of A1 binding events*

A close inverse correlation between the cytosolic Ca^{2+} level and the translocation velocity of individual platelets has been shown with single platelet analysis from a flow chamber study (Nesbitt et al., 2002). Consider the translocation velocity is an inverse metric of bond lifetime (Yago et al., 2008; Ju et al., 2013a), we thus hypothesized average bond lifetime (off-rate inverse) as an important determinant to triggered Ca^{2+}. In contrast to the A1WT, the 2B mutant A1R1450E and 2M mutant A1V1279I showed very different triggered Ca^{2+} level at the same forces (Figure 6-4), we therefore tested whether the differences were predominantly due to the changes of binding kinetics caused by the structural variation, as we already found that the early binding events likely contributed most to Ca^{2+} onset. We overlaid A1WT (Figure 6-5 A, $\bullet$), A1R1450E (Figure 6-5 A, $\bullet$) and A1V1279I (Figure 6-5 A, $\bullet$) data all together with on the same plot of average percent increase of fura-2 ratio vs. average bond lifetime, and we found that bond lifetime well correlated with the Ca^{2+} regardless of difference forces and structural variations (Pearson $R = 0.82$) (Figure 6-5 A). This supports our hypothesized GPIbα mechanosensor mechanism that force-dependent bond lifetime (off-rate kinetics) plays a major role in inducing calcium and the mutation affects the signal triggering phenotype through the binding kinetics. Interestingly, the lifetimes for A1WT (Figure 6-5 A, $\blacksquare$) and A1R1450E

(Figure 6-5 A, ■) at 10 pN deviated from and fell below the linear fit line (possible outliers). This suggests structural variation may directly affect the triggering at low forces.
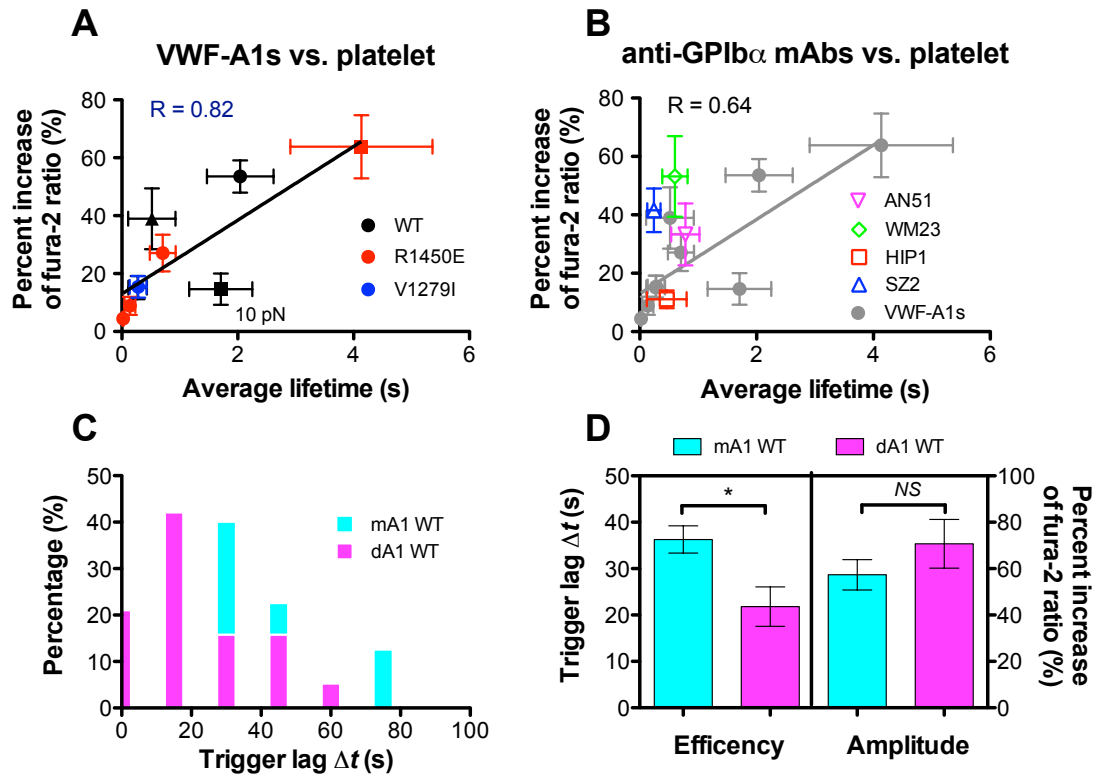
Figure 6-5. The biophysical mechanisms of GPIbα mediated Ca^{2+} triggering. (A) GPIbα triggered Ca^{2+} well correlates with A1–GPIbα bond lifetimes across different VWF-A1 ligands. Average percent increase of fura-2 ratio vs. average bond lifetime of platelet GPIbα bonds with mA1 WT (●), GOF 2B mutation R1450E (●) and LOF 2M mutation V1279I (●) at 10 (square), 25 (circle), 40 (triangle) and 60 (diamond) pN for each group. (B) GPIbα triggered Ca^{2+} well correlates with mAb–GPIbα bond lifetimes across different anti-GPIbα mAbs. Average percent increase of fura-2 ratio vs. average bond lifetime of platelet GPIbα bonds with mAbs AN51 (▽), HIP1 (□), SZ2 (△) and WM23 (◇) at 25 pN. The derived correlation with VWF-A1s in Panel A is grayed out as the overlay background. Dashed lines are linear fits to average values and the Pearson correlation coefficients (*R*) are indicated. (C) Histogram of triggering time lag (Δ*t*, calculated from the longest lifetime event to the Ca^{2+} elevation point) pooled from platelets triggered by monomer A1 (mA1, cyan) and dimer A1 (dA1, magenta) and normalized by the corresponding number of platelets in each group. (D) Ca^{2+} triggering efficiency (left ordinate, trigger lag) and amplitude (right ordinate, percent increase of fura-2 ratio) for mA1 (cyan) *versus* dA1 (magenta) (D and F). Data are presented as mean ± S.E.M. NS=not significant; * = p < 0.05, assessed by unpaired, two-tailed Student's t-test.

6.2.4 Ca²⁺ triggering amplitude is affected by GPIbα bonding location

Consider mechanosensor GPIbα as a nano machine, it is reasonable to hypothesize that applying forces to different locations of GPIbα via different ligands may induce different triggering effect. To test this hypothesis, a series of anti-GPIbα mAbs with known epitopes were coated on the probe bead (cf. Figure 6-1 A and B). Anti-GPIbα antibodies used in these studies include AN51, AK2, SZ2 and WM23 (Figure 1-2). In a top-down order from the N-terminus, AN51 binds to the N-terminal flank of GPIbα (residues H1-I35), HIP1 recognizes an epitope in the third leucine-rich repeats (residues Q59-D83), SZ2 binds to the anionic sulfated sequence (residues D269-Q282) whereas WM23 binds to an epitope in the macroglycopeptide mucin core (Shen et al., 2000; Dong et al., 2001; Peng et al., 2005). As expected, these mAbs showed different levels of Ca^{2+} triggering at 25 pN (Figure 6-5 B). However, when we correlated the calcium signals with their bond lifetime (Figure 6-2 C), we found that only two of them, AN51 and HIP1 (Figure 6-5 B, ▽ and □ respectively), fell into the previously figured correlation with VWF-A1 ligands (Figure 6-5 B, gray). Surprisingly, the epitopes of these two mAbs are located proximal to the VWF-A1 binding site in GPIbαN (Figure 1-2). On the other hand, SZ2 and WM23 (Figure 6-5 B, △ and ◇ respectively) fell above the linear fit line of the correlation of lifetime and Ca^{2+} (Figure 6-5 B, gray) as their epitopes are distal to the A1 binding site. Interestingly, the average lifetime at 25 pN for all four mAbs are similar, however the triggered Ca^{2+} was strongest for WM23 and followed by SZ2, AN51 and HIP1. These data suggested the closer the GPIbα bonding location is to membrane, the stronger Ca^{2+} might be triggered, which implied a mechano-transduction mechanism to be understood in future biophysical studies.

6.2.5 *Ca^{2+} triggering efficiency is affected by A1–GPIbα bonding valency*

Previous reports showed that conditional clustering of GPIb complex on platelets is sufficient to trigger internal Ca^{2+} and Src signal that activates platelet without external force and Ca^{2+} influx (Kasirer-Friede et al., 2002; Navdaev and Clemetson, 2002). This suggests the avidity modulation may play an additional role over the affinity modulation in triggering platelet signal. To investigate the potential contribution from the A1–GPIbα binding valency, we compared the Ca^{2+} triggering by mA1 (Ju et al., 2013a) and dA1 (Mazzucato et al., 2002). We found the lagging time (Δt), duration between the longest lifetime event and Ca^{2+} onset, was significantly shorter for dA1 engaging platelets (21.8 s) than mA1engaging platelets (36.3 s) (Figure 6-5 C and D). However, the triggered Ca^{2+} amplitudes by the two A1 constructs were not significantly different (Figure 6-5 D). Remember that the recombinant dA1 was made to mimic the least A1 repeat in natural VWF and it has the higher potential to induce GPIb clustering over the mA1 (Azuma et al., 1991; Kasirer-Friede et al., 2004). This result suggest the triggering is determined by the avidity modulation in which binding valency determines the Ca^{2+} triggering efficiency while binding affinity governs the Ca^{2+} triggering amplitude.

6.2.6 *Platelet GPIbα triggered signal primes β_3 integrin to an intermediate affinity state*

Recently, it has been shown that the initial phase of thrombus formation under pathological condition with a high shear rate ($> 1,000$ s^{-1}) principally involves discoid platelets and requires the cooperative function of both GPIbα and integrin $\alpha_{IIb}\beta_3$ (Maxwell et al., 2007; Nesbitt et al., 2009). The current opinion on the initial outside-in signaling events mediated by GPIbα is that platelet engagement of surface immobilized VWF triggers the initiation of an elementary calcium spike, leading to low level integrin $\alpha_{IIb}\beta_3$

activation (Nesbitt et al., 2002). At this stage, the integrin activation remains reversible and platelets have the discoid shape. The current knowledge on this GPIbα-mediated low level integrin activation and its significance is very limited.

The recent studies on discoid platelet aggregates suggested that the GPIbα triggered upregulation of integrin $\alpha_{IIb}\beta_3$ is priori to agonist induced platelet activation (Nesbitt et al., 2002; Maxwell et al., 2007; Nesbitt et al., 2009). The structure studies on β_3 integrin suggested that the shift from the low-affinity to the high-affinity structure may involve a number of intermediate conformational states such as the extended conformation with crossed headpiece (Takagi et al., 2002; Xiao et al., 2004; Springer and Dustin, 2012). Therefore, it is reasonable to hypothesize that GPIbα triggered calcium signal primes the β_3 integrin to the intermediate affinity state. Before we tested this hypothesis, we used the discoid platelet without any treatment and the activated platelet induced by ADP incubation to calibrate the low and high binding affinities of the β_3 integrin, because it was well accepted that $\alpha_{IIb}\beta_3$ has low binding affinity in a fresh discoid platelet while has high binding affinity in an agonist (i.e. ADP) activated platelet (Springer and Dustin, 2012; Ye et al., 2012).

To directly measure the 2D affinity, the platelet was repeatedly contacted with the FN probe for an adhesion frequency assay (see section 2.5.3) in which each contact resulted in a binary adhesion score (0 or 1) and its average over 50 contacts of the same duration t_c gives an adhesion frequency P_a. The 2D effective affinity (A_cK_a) was derived by fitting the curve of P_a vs. t_c, where m_r and m_l are the respective surface densities of the platelet receptor (i.e. $\alpha_{IIb}\beta_3$) and its ligand (i.e. $FNIII_{7-10}$) (Chesla et al., 1998; Huang et al.,

2010). Plots of P_a vs. t_c for discoid and activated platelets binding to $FNIII_{7-10}$ to exhibited two distinct adhesion levels: the discoid platelet curve takes up a low plateau (Figures 6-6 B, ●) while the activated platelet curve jumps to a high plateau (Figures 6-6 B, ●) at each equilibrium. The derived affinities indicated that β_3 integrin on an activated platelet has a ~25 fold higher 2D affinity than the counterpart on a fresh discoid platelet.
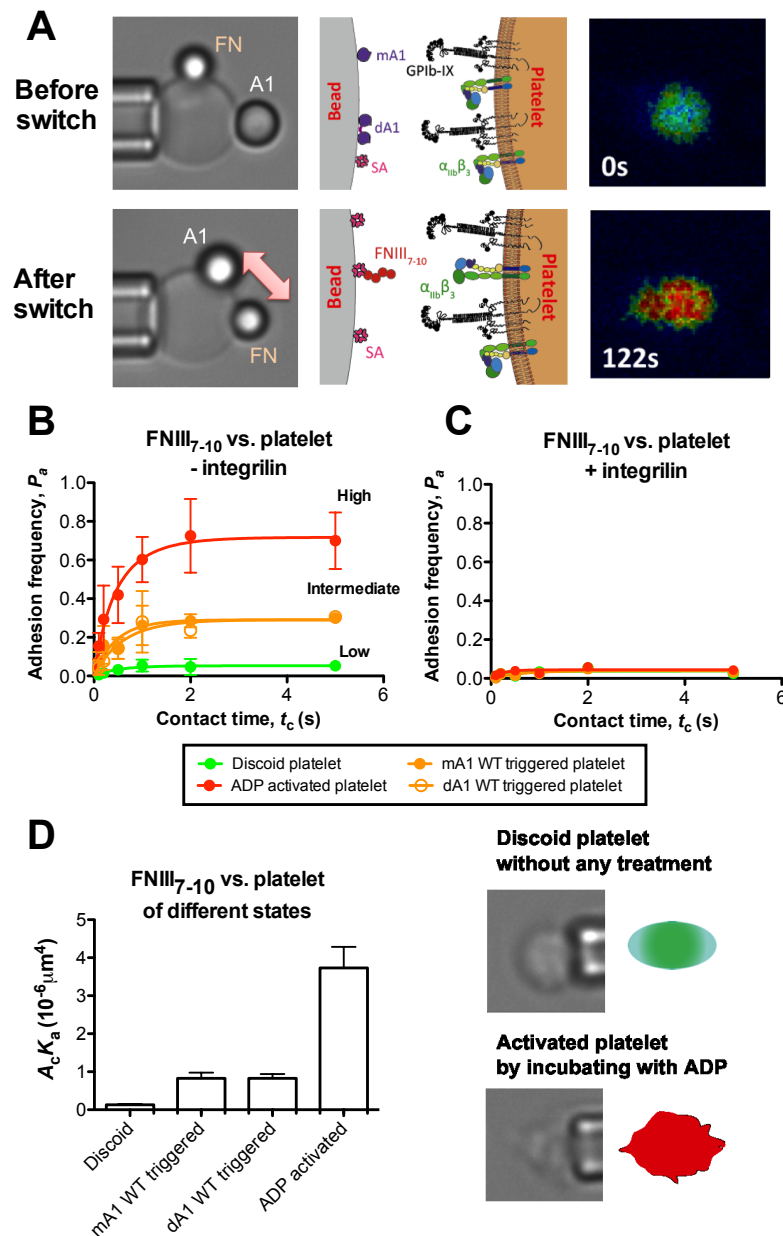
Figure 6-6. GPIbα-mediated Ca^{2+} triggering primes integrin α$_{IIb}$β$_3$ to the intermediate state. (A) Scheme of BFP switch experiment. Except that two beads, coated with mA1 and fibronectin fragment III 7~10 (FNIII$_{7-10}$) respectively, were attached to the RBC at the same time (*left columns*), all setups are similar to the normal BFP system (see section 2.5.3 and Figure 6-1 A). The experiment started with using A1 probe engaging the GPIbα on a platelet target (*upper middle*), the calcium was on the basal level at this moment (*upper right*); After the calcium was triggered (*lower right*) and observed, the probe was switched to the bead coated with FNIII$_{7-10}$ (*lower left*) and allowed to engage α$_{IIb}$β$_3$ on the same platelet target (*lower middle*). The manual switch was done fastly within 1~2 min in order to capture integrin priming in time. (B-D) Charaterize integrin α$_{IIb}$β$_3$ upregulation following triggered calcium signal by the adhesion frequency assay. The adhesion frequency assay was used to measure binding probability between FNIII$_{7-10}$ and α$_{IIb}$β$_3$ on platelets at a range of contact times in the absence (B) or presence (C) of 20 μg/ml β$_3$ inhibitor integrilin. Three experimental conditions were compared: intact platelet without any treatment (blue, micrograph showed the discoid shape), activated platelet by incubating with 10 μM ADP for 15 min (red, micrograph showed the irreversible morphological change) and mA1 (closed) or dA1 (open) triggered platelet from the first stage of BFP switch experiment (green). In the adhesion frequency assay, effective affinity A_cK_a (C) was derived by fitting the curve of adhesion frequency (P_a) vs. contact time (t_c) (B) with the model P_a=1 - exp{1 - $m_rm_lA_cK_a$[(- $k_{off}t_c$)]}, where m_r and m_l are the respective surface densities of α$_{IIb}$β$_3$ and FNIII$_{7-10}$. Error bars represent S.E.M. of >3 platelet–bead pairs.

To investigate the role of GPIbα mediated Ca^{2+} in upregulating platelet integrin, we designed a new method called "BFP switch assay" to decouple the bindings from GPIbα and β$_3$. In the "switch" experiment, two beads were attached to one RBC: one was coated with GPIbα ligand A1, the other was coated with α$_{IIb}$β$_3$ ligand fibronectin fragment FNIII$_{7-10}$ (Figure 6-6 A, *upper row*). In the first stage of the experiment, a platelet first repeatedly engaged with an A1-coated probe bead and enabled calcium triggering as the above fBFP force-clamp assay (Figure 6-3). After observing the Ca^{2+} mobilization, the RBC was manually rotated to orient FNIII$_{7-10}$ against the platelet. The bead switch from a A1 probe to a FN probe was done as quickly as possible (<2 min) so that we could observe the upregulation of integrin binding in time. In the second stage of the experiment after the switch (Figure 6-6, *lower row*), the A1-triggered platelet was repeatedly contacted with the FN probe bead for an adhesion frequency assay as

mentioned above (Figure 6-6 B-D). Remarkably, the plot of P_a vs. t_c for both mA1 and dA1 triggered platelets binding to FNIII$_{7-10}$ exhibited an intermediate adhesion levels between the calibrated curves of the low and high integrin affinity states (Figures 6-6 B, ●). The control experiments showed that integrilin, a clinical RGD mimetics known to efficiently block bindings of platelet $\alpha_{IIb}\beta_3$ and $\alpha_v\beta_3$ to fibrinogen (Okada et al., 2011), abrogated all FNIII$_{7-10}$ binding to each state of β_3 integrin (Figure 6-6 C) and confirmed that the binding upregulation was primarily from $\alpha_{IIb}\beta_3$ considering $\alpha_{IIb}\beta_3$ copy numbers on a platelet is predominant over $\alpha_v\beta_3$ (Lawler and Hynes, 1989). The calculated β_3 integrin 2D affinity from A1 triggered platelet was 7-fold higher than the low affinity but 3.5-fold lower than the high affinity (Figure 6-6 D), providing a direct evidence that following the A1-triggered Ca^{2+} signal, the β_3 integrin has an intermediate affinity.

6.3 Discussion

Our study has elucidated how force regulates VWF–GPIbα bond dissociation, determined the magnitude and duration of force necessary for platelet Ca^{2+} triggering, and revealed the best force-dependent A1–GPIbα kinetic parameter for platelet triggering. We have also shown that, by abolishing A1WT-specific catch bond, 2B mutation A1R1450E greatly reduces the GPIbα bond stability as force increases which results in a slip bond.

Our simultaneously *in situ* measurements of force-regulated A1–GPIbα binding kinetics and the resulting intracellular Ca^{2+} flux allowed us to analyze the kinetics requirements for signaling. Our analysis indicates that a common correlation relationship holds for all A1WT and VWD 2B mutant A1R1450E and 2M mutant A1V1279I suggesting that the GOF phenotype of the former is probably due to its small off-rate at

<10 pN, however, the rapidly increased off-rate by force resulted in its Ca^{2+} triggering deficiency at >25 pN; while the LOF phenotype of the latter can be explained by its globally reduced bond lifetime, thereby, it also showed the deficiency in Ca^{2+} triggering (Figures 6-4 and 6-5 A). These observations indicate that mechanical force and structural variation may all regulate the platelet signal transduction by regulating the receptor binding kinetics functions (Figure 6-5 B). On the other hand, pulling the GPIbα at different locations by mAbs induced different level of calcium signals with the similar amount of bond lifetime and at the same force. This suggested that GPIbα bonding location affects the mechanotransduction geometrically. Moreover, dimeric A1 triggered Ca^{2+} signal with a significantly shorter time lag than monomeric A1 did. This suggested the binding valency governs the triggering efficiency and it is probably due to the crosslinking of GPIbα and the induced GPIbα clustering downstream may enhance the signal transduction.

It has long been assumed that thrombus development in vivo involves the sequential accrual of individual platelets onto the thrombogenic surface, leading to platelet shape change, integrin $α_{IIb}β_3$ activation, and firm adhesion (Ruggeri et al., 1999; Ruggeri, 2002; Du, 2007). However, this concept has recently been challenged by the findings that discoid platelet can aggregate in a platelet activation independent manner under high shear conditions. At shear rate 1,000-10,000 s^{-1}, which are typically found in the arterial microcirculation or in regions of moderate arterial stenosis, GPIb cooperates with integrin $α_{IIb}β_3$ in promoting the initial formation of discoid platelet aggregates (Maxwell et al., 2007; Nesbitt et al., 2009); while at shear rate 1,000-10,000 s^{-1}, which occurs at sites of severe vessel narrowing, i.e. atherothrombosis site, discoid platelets

aggregate through a process mediated solely through VWF–GPIbα bonds (Ruggeri et al., 2006). However, the immediate signaling effect following the VWF–GPIbα engagement on integrin $\alpha_{IIb}\beta_3$ and its significance is still unknown. Several lines of evidences suggested an intermediate integrin $\alpha_{IIb}\beta_3$ affinity state may exist when a platelet still retains its discoid shape: 1) GPIbα triggered calcium signal leads to the increase in VWF–$\alpha_{IIb}\beta_3$ binding reversibly before the agonists release (Nesbitt et al., 2002); 2) The intermediate state of purified $\alpha_{IIb}\beta_3$ ectodomain has been observed with an extended-close conformation, however, no intermediate affinity has been measured and compared with other states yet (Springer and Dustin, 2012). In this study, we have demonstrated that the β_3 integrin binds to the $FNIII_{7-10}$ with an intermediate cellular affinity right after the GPIbα induced Ca^{2+} signal. This intermediate affinity state is 3.5-fold lower than the high affinity state calibrated by engaging the integrin on an ADP activated platelet. As to our knowledge, this is the first report observing the intermediate affinity of integrin on a live platelet. Note that the platelet shape remains discoid for the entire switch experiment suggesting this GPIbα induced integrin priming is activation independent (Figure 6-6). Besides, it has been shown that mice lacking both of VWF and fibrinogen, can still form occlusive thrombi in injured arterioles and the plasma fibronectins account for the residual effect (Ni et al., 2003; Matuskova et al., 2006). Consider the $\alpha_{IIb}\beta_3$ binds to the fibronectin and VWF via the RGD motif while it binds to the fibrinogen via QAGDV motif (Springer et al., 2008), and it is well known that high shear flow in arterioles does not favor $\alpha_{IIb}\beta_3$ binding to fibrinogen (Savage et al., 1998), thus it is very likely the FN–$\alpha_{IIb}\beta_3$ binding provides a reinforcement role to support initial GPIbα mediated tethering

under high shear condition, and such reinforcement requires the signal from GPIbα (Figure 6-7).

Under the high shear condition, platelet activation requires completion of a series of reaction steps that proceed only when the GPIbα is engaged by VWF but would be immediately and completely reversed upon bond dissociation (Nesbitt et al., 2002; Maxwell et al., 2007). Our data show that the longest lifetime well correlates Ca^{2+} event and suggest that a single long lifetime may play a dominant role in finishing the urgent platelet triggering mission to stop the bleeding. Force plays an important role through the catch bond mechanism to regulate the triggering. Based on the previous flow-dependent GPIbα signaling studies (Kasirer-Friede et al., 2002; Nesbitt et al., 2002; Kasirer-Friede et al., 2004), activation independent platelet aggregation model (Bergmeier et al., 2006; Ruggeri et al., 2006; Maxwell et al., 2007; Nesbitt et al., 2009) and the present work, we propose that mechanosensor GPIbα plays a pivotal role in tethering platelet under high shear condition and transducing the signal to cooperate with integrin $\alpha_{IIb}\beta_3$ to stabilize the thrombus in both scenarios of hemostatsis and thrombosis (Figure 6-7), the process can be summarized into three stages: 1) initial tethering, VWF–GPIbα binding with the fast on-rate pins down fast-circulating platelets onto the exposed subendothelium; 2) adhesion reinforcement, catch bond prolongs A1–GPIbα bond lifetime and triggers Ca^{2+} signal by which integrin $\alpha_{IIb}\beta_3$ is primed to the intermediate affinity to reinforce the platelet adhesion; 3) firm adhesion, the released agonist will quickly activate the decelerated platelet in an autocrine manner and maturate integrin $\alpha_{IIb}\beta_3$ to the high affinity state through the inside-out signaling pathway.

Moreover, it has long been recognized that VWD is due to the deficiency in platelet adhesion because mutations in VWF or platelet GPIbα can either reduce or increase the affinity of platelet binding (Ruggeri, 2004; Sadler, 2005a; Szántó et al., 2012). However, we want to expand this concept that altered binding kinetics by VWD mutations may cause defects in the signal transduction, impede further thrombus development and result in bleeding. For the 2B mutant A1R1450E, we found that the GOF mutation did reduce the off-rate at the 10-pN, however, as force increased to 25-pN, the lifetime rapidly droped by 10-fold and became insufficient to trigger type α Ca^{2+} efficiently as opposed to the A1WT (Figure 6-5 B). Therefore, the weakened signal transduction caused by the lowered force resistance may bring in an additive explanation to the 2B VWD paradox (Figure 6-7). Whether a similar mechanism operates under pathophysiological conditions has not been defined, further *in vivo* studies will help give an answer.

Haemostasis

Thrombosis

I. Initial tethering

II. Adhesion reinforcement

Type α Ca^{2+}

Inside-out signal

III. Firm adhesion

VWF

Outside-in signal

WT

2B mutant

117
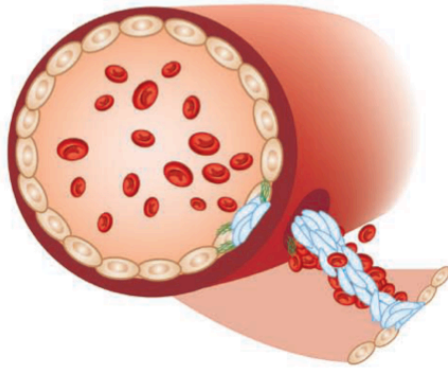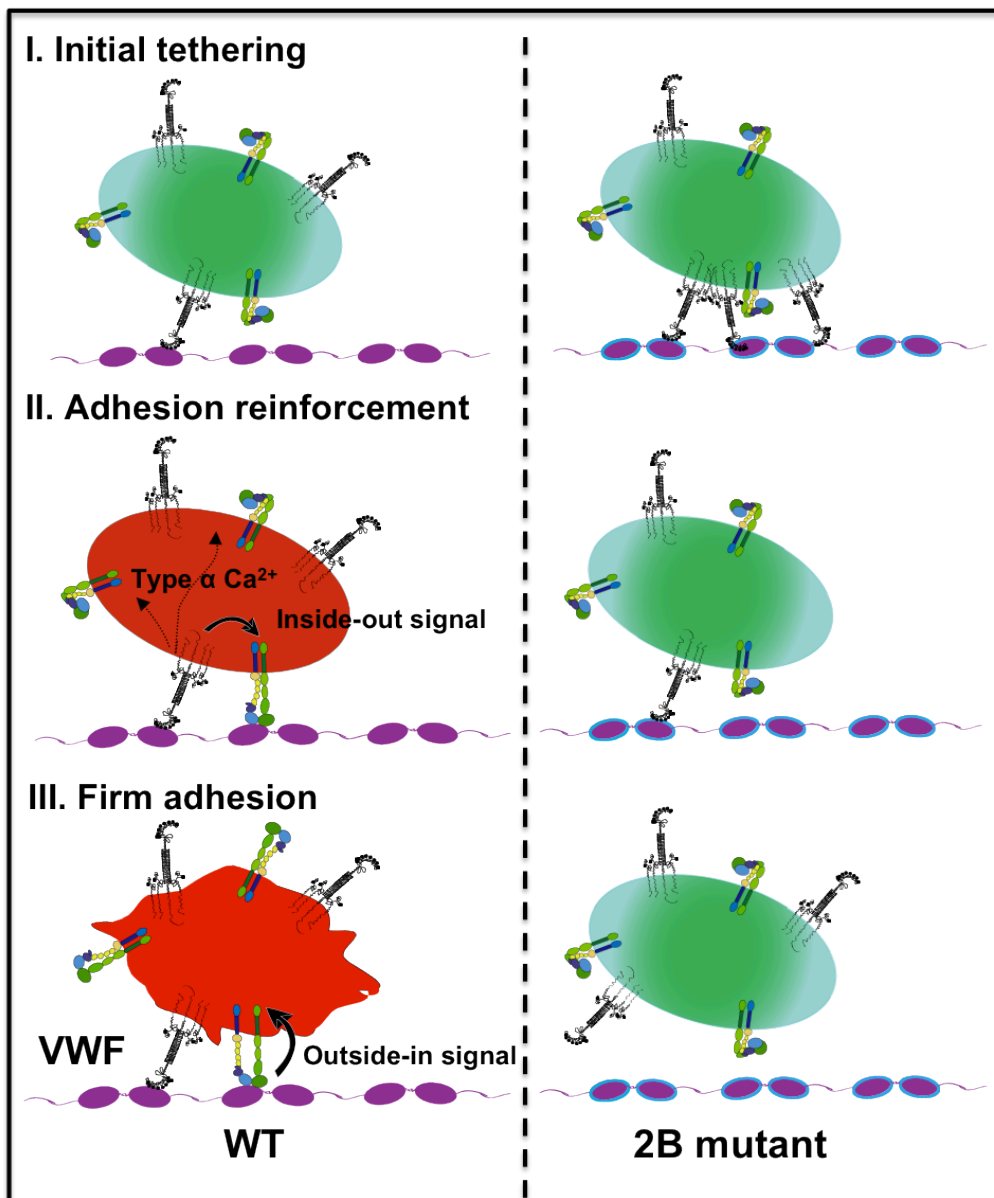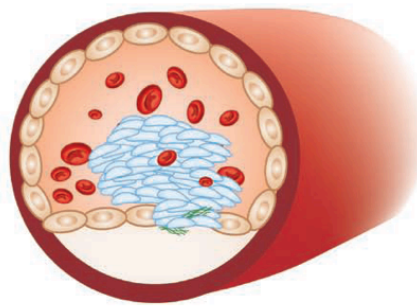
Figure 6-7. Updated model of early-stage platelet adhesion. Rapid shear stress increase caused by blood flow perturbations promotes platelet adhesion at the site of vascular injury for its hemostasis (upper left, platelet adhesion leads to rapid hemostatic plug) and thrombosis function (lower left, platelet adhesion builds up platelet-rich thrombi on the surface of a disrupted atherosclerotic plaque). Force–mediated platelet adhesion is concluded in three stages: I. initial tethering stage, shear force enhances platelet attachment to VWF surface via the A1–GPIbα catch bond; II. adhesion reinforcement stage, force prolonged A1–GPIbα bond transduces signal (Type α Ca^{2+}) primes the integrin $\alpha_{IIb}\beta_3$ to the intermediate state. The additive binding affinity of $\alpha_{IIb}\beta_3$ to VWF reinforces the adhesion between the platelet and VWF. The platelet shape retains discoid at this stage; III. the binding to VWF along with the Ca^{2+} influx and agonist release (i.e. ADP, thrombin, TxA_2) further mature the integrin affinity and activate integrin through both outside-in and inside-out pathways. The platelet undergoes significant shape change toward full activation irreversibly. The type 2B mutant VWF shows the higher GPIbα binding affinity only at low forces. However, some of them do not support effective GPIbα binding as force increases (i.e. R1450E), thereby the force and bond lifetime does not coordinate well for efficient triggering and integrin priming; while the other type 2B mutant VWF shows higher GPIbα binding affinity globally and triggers calcium similarly to WT VWF does, but they do not prime integrin efficiently. The cause for that remains unknown. Overall, the net outcome for 2B mutation is the defect in integrin priming and inefficient platelet activation. The top panels were adapted and modified from (Jackson, 2011) and the illustrations in lower panels were drawn by Yunfeng Chen.

CHAPTER 7: CONCLUSIONS

7.1 Summary

The beauty of being a biomedical engineering Ph.D. student is to think in two completely different mindsets. From a perspective of an engineer, the established mechanisms can guide us to develop new tools. The theory of red blood cell mechanics was well established a decade ago. Taking advantages of its elastic property, close to an ideal spring, people engineered it into an ultrasensitive force probe. In chapter 3, we improved it with the new controlling software and hardware for higher spatial and temporal resolution; moreover, we even combined it with the fluorescent techniques and upgraded it into the fBFP. On the other hand, from a perspective of a biologist, new techniques always could greatly advance scientific research, uncover the underlying biological mechanisms and understand the essence of the unknown world. Therefore, in Chapter 4 to 6, we applied the BFP we built to study the platelet mechanosensory mechanisms on a single-molecule level.

Interestingly, the platelet adhesion acts as a good example showing the importance of physical regulation in biology. An important, yet incompletely under-stood, aspect of thrombogenesis is the impact of shear force on platelet adhesion. Mechanical regulation plays a big part in promoting occlusive thrombus formation, as thrombus propagation and vessel occlusion will probably occur on plaques that markedly

disturb laminar blood flow relative to nonstenotic lesions. In my thesis, we asked two key questions to understand the VWF–GPIbα mediated early-stage platelet adhesion:

i)   How the VWF–GPIbα interaction is mechanically regulated by flow?

ii)   How does force initiate VWF–GPIbα mediated signaling (triggering)?

To answer the first one, we hypothesized two mechanisms: 1) force regulates the VWF–GPIbα dissociation (off-rate) and 2) transport regulates VWF–GPIbα association (on-rate). In Chapter 4, we found the N-terminal sequence Q1238-E1260 of the VWF-A1 regulates the VWF–GPIbα dissociation under the mechanical force. This sequence plays a dual role as it inhibits the A1–GPIbα interaction at low forces but stabilizes the A1–GPIbα interaction in a catch bond as force increases. The inhibitory effect of the peptide form of this sequence was found from the whole blood perfusion assay. This shed light to a potential therapeutic value that translates this peptide into an anti-thrombotic drug. In Chapter 5, we identified distinct steps of transport mechanism regulating A1–GPIbα on-rate: 1) tethering of platelet to the vascular surface over a separation distance; 2) Brownian motion of the platelet; 3) rotational diffusion of the interacting molecules.

To connect the adhesive function of GPIbα with its signaling function and directly prove it as a mechanosensor, we studied how force triggers platelet signal via GPIbα in Chapter 6. We found three mechanisms:

1)   Biophysical regulation: both force and structural variation regulates calcium triggering by affecting the A1–GPIbα engagement duration (bond lifetime).

2)   Geometrical regulation: pulling GPIbα at different locations results in different amplitude of calcium flux.

3)   Biochemical regulation: bonding valency determines the efficiency of calcium triggering.

To further investigate the significance of the GPIbα triggered signal. We found that the minimum signal triggered by a single A1–GPIbα bond can prime the platelet β_3 integrin (The majority is the $\alpha_{IIb}\beta_3$) into intermediate affinity state while the platelet shape still remains discoid. This suggests the initial signal from GPIbα may serve to prime integrin and reinforce the initial adhesion mediated by GPIbα alone.

7.2 Future studies

The structural insights responsible for transducing force into a biochemical signal are still poorly understood. Based on the current model of GPIb complex, the A1 binding site is located ~40 nm above the membrane (Figure 1-2). Consider the force is applied through the A1–GPIbα bond, if so, how does mechanical stimulus is transduced over such long distance? How does it get across membrane? In addition to VWF activation, can force also induce conformational changes in GPIbα? What are the GPIbα and GPIX's contributions in signal transduction? To answer these questions, mutations have to be introduced to GPIb on platelet. However, it is difficult to make mutagenesis on human platelet. To better understand the GPIb or other platelet receptor mediated signal mechanotransduction, the new BFP protocol needs to be developed for mouse platelet (about half size of a human platelet, but more difficult to induce signaling). In addition to calcium readout, other intracellular signal readout can also be developed, i.e. actin and

121

FRET biosensor, to study mechanosensors. In addition to the experimental initiatives, the quantitative results and measurements can be used to model the mechanotransduction and figure out the governing mechanical parameters for each specific receptor and define their relative contributions for diagnostic tool development.

The single-cell and single-molecule studies provided us more in-depth knowledge on the mechanosensory function of platelets, which is central to the initiation and propagation of platelet thrombi. Much remains to be learned about the complex, dynamic interplay between biophysical and biochemical regulatory mechanisms of platelet aggregation, and their contribution to initial thrombus growth, stability and embolization. In future career, I will combine the molecular level (i.e. single-platelet studies in my Ph.D. training) and tissue level (i.e. thrombosis animal model, micro-vessel on microfluidic chip) techniques for a clearer understanding of the pathogenesis of diverse thrombotic and bleeding disorders, including atherosclerosis, ischemia-reperfusion injury, deep venous thrombosis, and VWD; and solving clinical issues such as a partial luminal obstruction (a developing thrombus, an atherosclerotic plaque or an intravascular device), a change in vessel geometry (extrinsic constriction of blood vessels, vascular bifurcation or aneurysm) or sudden flow changes (vessel hypoperfusion due to shunting or upstream obstruction).

CHAPTER 8: MISCELLANEOUS PROJECTS

8.1 A cortical tension study on megakaryocytes by micropipette aspiration

We collaborated with Ms. Yolande Chen from Dr. Seth Corey lab (Northwestern Feinberg School of Medicine, Chicago, IL) and Dr. David Myer and Mr. Reginald Tran from Dr. Wilbur Lam lab (Georgia Institute of Technology, Atlanta, GA). The work was published on *Blood* (Chen et al., 2013).

Megakaryocytes generate platelets through extensive reorganization of the cytoskeleton and plasma membrane. Cdc42 interacting protein 4 (CIP4) is an F-BAR protein that localizes to membrane phospholipids through its BAR domain and interacts with Wiskott- Aldrich Syndrome Protein (WASP) via its SRC homology 3 domain. F-BAR proteins promote actin polymerization and membrane tubulation. To study its function, we used megakaryocytic CHRF-288-11 cell lines. In selected studies, RNAi was used to knockdown CIP4 or WASP.

8.1.1 *Measure cell cortical tension by micropipette aspiration*

CHRF cells were injected into an open-sided chamber filled with 1x PBS. A micropipette was inserted from side to grab one cell at a time. The aspiration pressure was controlled through a homemade manometer system and connected with a water pressure sensor for readout (see section 3.2). There is a tension in the cortical actin layer that pulls the cell into a spherical shape (with a radius, R_c), similar to surface tension pulling a water drop into a sphere. By finely tuning the suction pressure (Δp, pressure

difference between inside and outside micropiette), we could allow the cell maintain a spherical shape while the aspirated region is a hemisphere, which means the aspiration length (L_p) is equal to the pipet radius (R_p). Therefore, similar to deriving BFP spring constant from an aspired RBC (Equation 3-1, see section 3.1), we could apply the Law of Laplace to calculate the cortical tension (T_c, with units of force per length) (Hochmuth, 2000; Chen et al., 2012).

$$T_c = \frac{R_c R_p}{2(R_c - R_p)} \Delta p,$$

<div align="right">Equation 7-1</div>
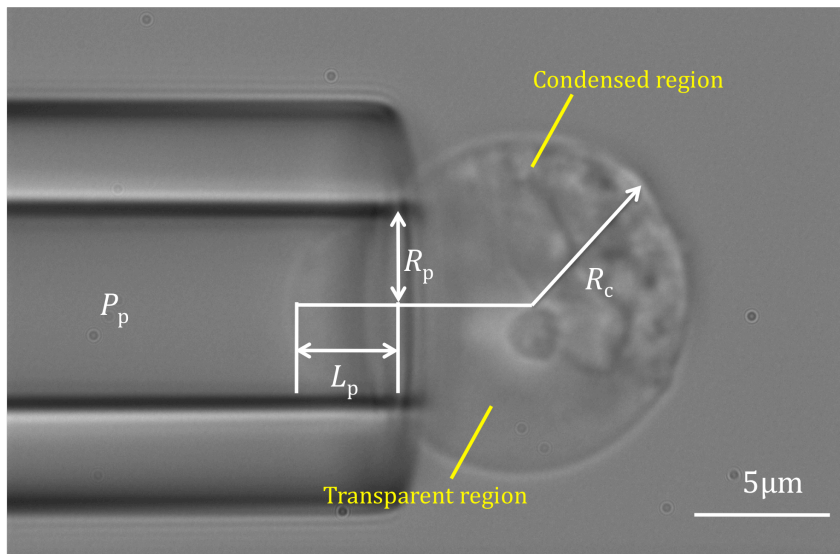
Figure 8-1. The scheme of micropipette aspiration of a CHRF cell. Micrograph of micropipette aspiration of a CHRF cell. The pressure in buffer (P_0), the suction pressure inside the pipette (P_p), the inner radius of the pipette (R_p), the radius of the spherical portion of the cell outside the pipette (R_c), and the length of the cell tongue aspirated inside the pipette (L_p) are indicated. Aspiration could cause polarization of cytoplasmic contents. The image shows the condensed region stays away from the pipette orifice where a transparent region is formed nearby. Sometimes, the transparent region could be dynamically transformed into a bleb.

8.1.2   Effect of CIP4 knockdown on cell cortical tension

Cell cortical rigidity depends on the connections between the actin and the membrane (Brugués et al., 2010). Through its SH3 domain and recruitment of WASP, CIP4 regulates actin polymerization, a main regulator for cortical rigidity (Gilden and Krummel, 2010). To measure stiffness of the actin cortex that provides support for the plasma membrane, we performed micropipette aspiration. To well characterize the effect of CIP4 knockdown, we compared the cortical tensions of CHRF cells under different stimulation conditions, specifically by treating cells with PMA and fibronectin (FN). In general, CIP4 knockdown would result in a significant reduction of the cortical tension (Figure 8-2 A), which suggested that the anchorage of actin fiber with membrane was weakened and CIP4 played a major role in adapting the cytoskeleton with the membrane. The treatment of PMA significantly reduced the cortical tension for both control (Figure 8-2 B) and CIP4 knockdown cells (Figure 8-2 C), while fibronectin treatment seemed not to have any significant effect. However, treating the PMA over 4 hours would lead to an opposite effect that much higher cortical tension and more condensed cytoplasmic contents and irregular morphologies (Figure 8-2 D) as opposed to the normal spherical shape (Figure 8-2 C). The morphological studies of CHRF cells under the isotonic condition showed that the certain exposure to the PMA would limit the cell swelling, while over exposure to the PMA might cause the cell fail to swell (Data not shown).
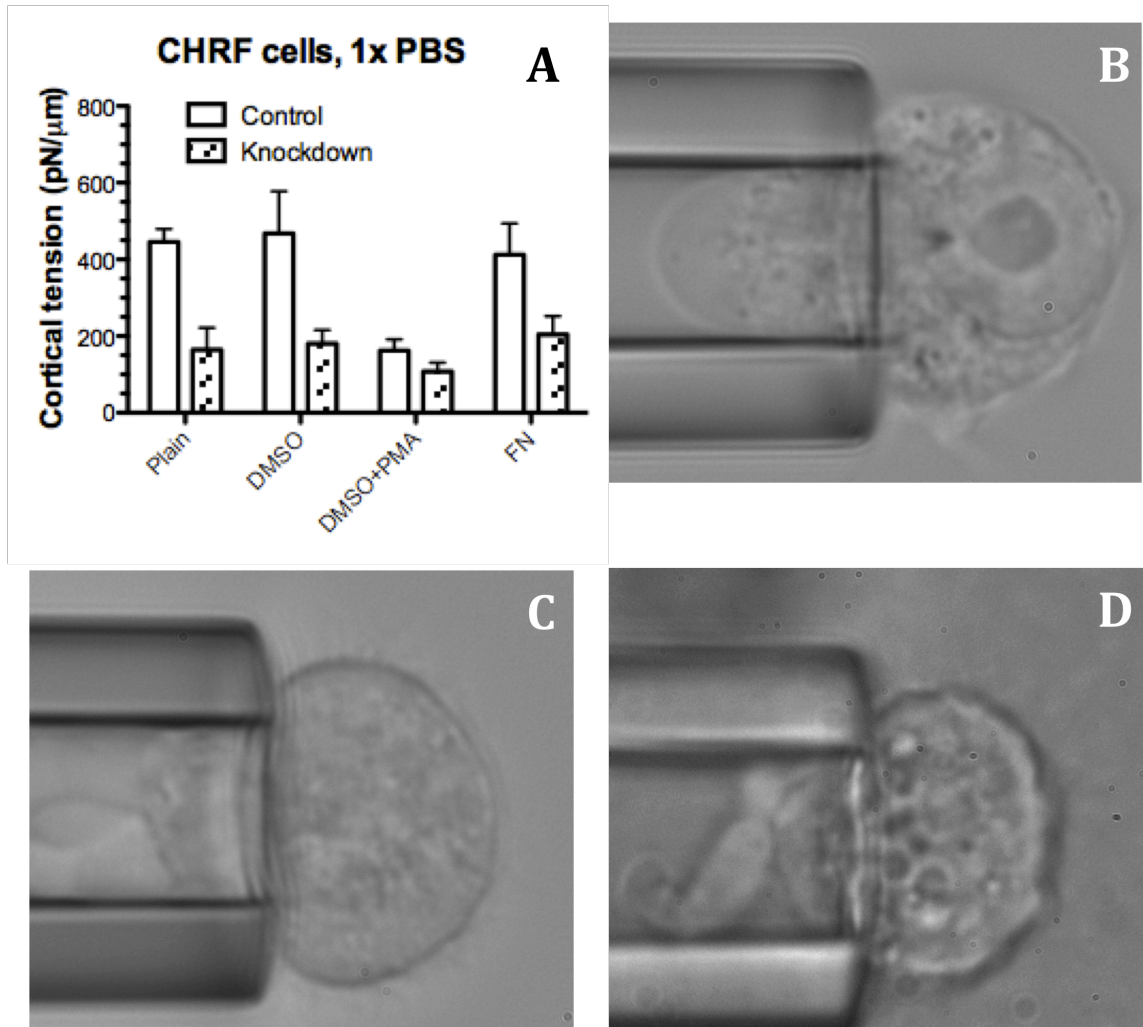
Figure 8-2. Loss of CIP4 reduces cortical tension in CHRF cells. (A) Decreased cortical tension in CHRF cells after reduced levels of CIP4 either at baseline or after treatment with either PMA or fibronectin (FN). (B-D) Representative images of micropipette aspiration of an untreated cell without (B) or with (C) CIP4 knockdown and a PMA treated cell (D). Without CIP4 knockdown, the transparent region was aspirated furthest into the pipette and blebbing was rare. With CIP4 knockdown, cell swelling was observed under the isotonic condition. Repeated blebbing was observed in the inner transparent region inside the pipette. Images were obtained with an inverted microscope with 40x dry lens through a camera (GC1290) (see section 2.5.1). The funky morphology of the PMA treated cell (D) shows the swelling is complete compromised. The end tip of the aspired region constantly blebs.

8.1.3   *Characterize the CHRF cells blebbing*

Compared with control CHRF cells, CIP4 knockdown reduced cortical tension in all conditions tested (Figure 8-2), suggesting that the anchorage of actin fibers with the

126

cellular membrane was weakened. These studies revealed that the actin-rich cellular cortex is softer (due to decreased actin polymerization) in CIP4-deficient cells. These differences were maintained even when cortical tension increased after PMA stimulation. Sometimes, the transparent region turned into blebs (Figure 8-3 A), irregular bulges in cell membrane due to the decoupling of the cytoskeleton from the plasma membrane. In control condition, the transparent region was aspirated farthest into the micropipette and blebbing was rarely observed. With CIP4 knockdown, cell swelling was observed under the isotonic condition, and repeated blebbing was observed in the inner transparent region inside the pipette (Figure 8-3 B)(measurements in Figure 8-2 A were performed before blebbing occurred).
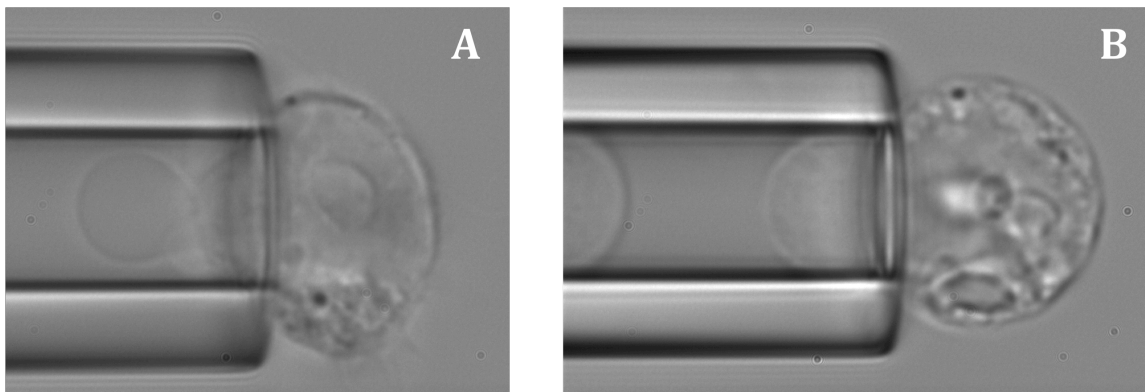
Figure 8-3. **Blebbing of CHRF cells.** (A) Initiation of membrane blebbing. The near-orifice transparent region was pinched off and transformed into a bubble-like protrusion. The dynamic process was driven by the sucking pressure. (B) Repeated blebbing. The protruded bleb was snitched out, followed by a newly-extruded immature bleb.

Micropipette aspiration demonstrated the decreased cortical actin tension in megakaryocytic cells with reduced CIP4 proteins.

8.2 Investigate the β_1 integrin mediated thymocyte adhesion and its regulation by plexinD1-sema3E pathway

We collaborated with Dr. Ellis L. Reinherz lab (Harvard). The work was under review by *PNAS*.

Plexins and semaphorins comprise a large family of receptor-ligand pairs controlling cell guidance in nervous, immune and vascular systems. How plexin regulation of neurite outgrowth, lymphoid trafficking and vascular endothelial cell branching is linked to integrin function, central to most directed movement, remains murky. It has been hypothesized that on developing thymocytes, plexinD1 controls surface topology of nanometer scale β_1 integrin adhesion patches *in cis* while its ligation by sema3E in *trans* regulates individual β_1 integrin catch bonds. Sema3E ligation shortens individual integrin bond lifetimes under force to reduce affinity.
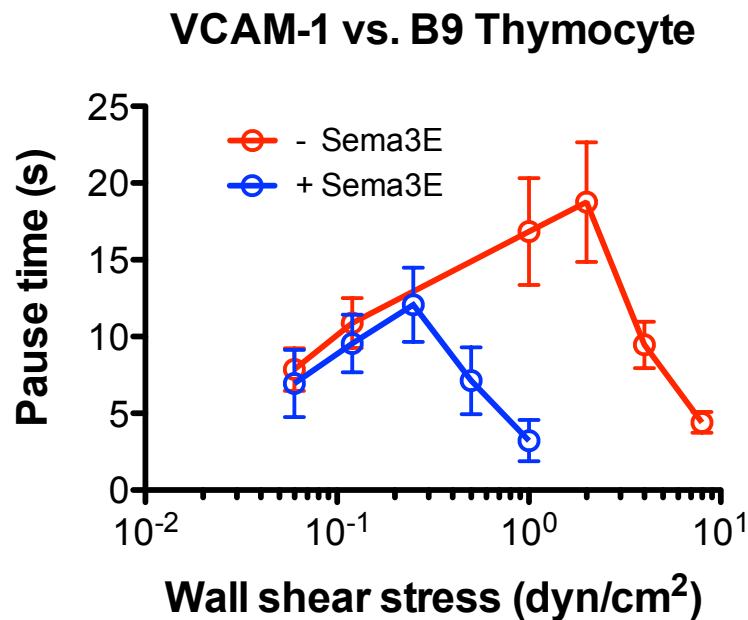
Figure 8-4. Sema3E releases WT thymocyte resistance to shear stress.

128

To study the a_4b_1-VCAM-1 bond characteristics under a range of applied shear stresses and regulation by sema3E (Figure 8-4), we examined thymocyte "pause" time on a VCAM-1-coated surface in a shear flow chamber (Figures 8-4 and 8-5, see section 2.9.2) to recapitulate the adherence characteristics under flow and in response to chemokines under defined shear stress conditions. The WT thymocytes exhibited much greater tethering to the VCAM-1 surface in the absence than in the presence of sema3E (Figure 8-5). This differential is represented by significantly-increased maximal pause time and an 8-fold increase in resistance to applied shear stress (Figure 8-4). This result suggested that plexinD1 exerts a bimodal effect upon integrin avidity; first, by maintaining a tight clustered membrane geometry and, second, through interaction with its ligand sema3E, an abrogation of b_1 integrin "catch" bonds. These results helped demonstrate tunable molecular features of integrin adhesion with broad implications for multiple cellular processes.

- sema3E

+ sema3E

| **0.12 dyn/cm^2** | **1 dyn/cm^2** | **8 dyn/cm^2** |
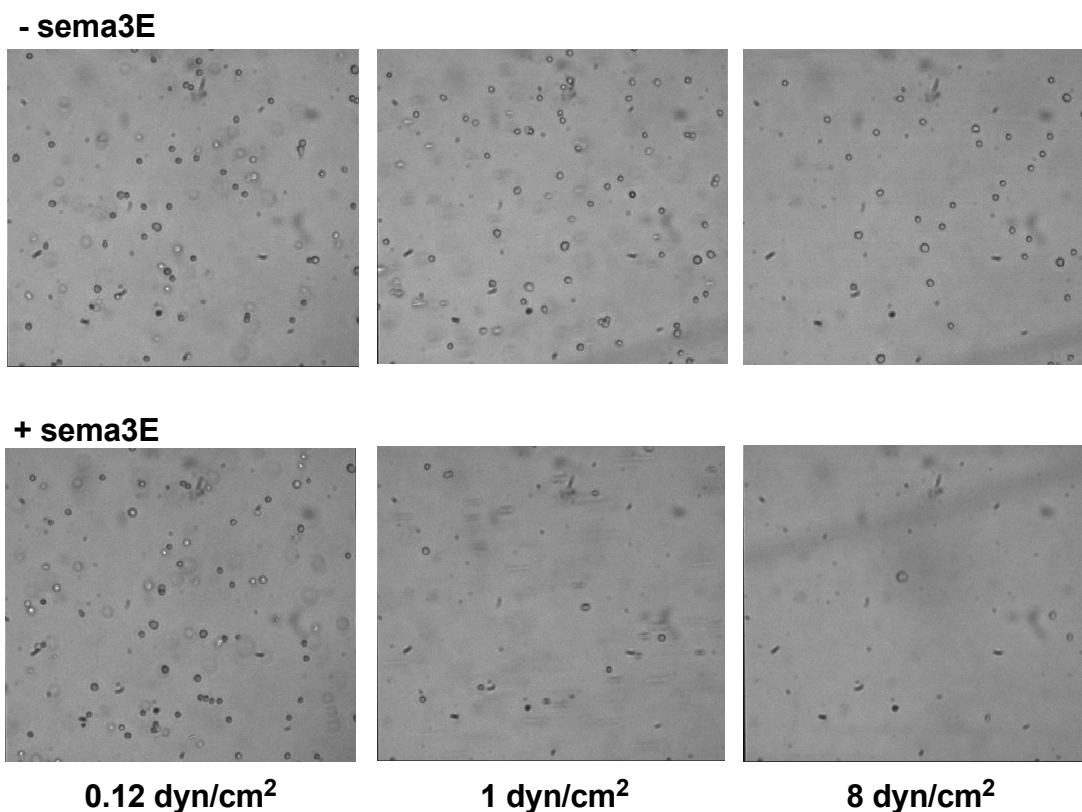
Figure 8-5. Representative images of cells in shear flow chamber under increasing shear force. The shear forces represent 3 differing shear stress conditions contributing to Figure 8-4. At 0.12 dyn/cm^2, there is no significant difference between pause times for untreated and sema3e-treated WT thymocytes. At 1 dyn/cm^2, the difference in pause time is maximal and by 8 dyn/cm^2, the pause times for untreated WT cells have fallen to the same level as those observed for semaE-treated cells at 1 dyn/cm^2.

8.3 Force-stiffened synergistic binding of syndecan-4 and β_1 integrin to thy-1

This study has been pioneered and further developed by me and another peer Ph.D. student Vince Fiore from Dr. Thomas Barker lab (Georgia Institute of Technology, Atlanta, GA). The work was about to submit to *PNAS*.

Cells are able to sense the mechanical properties of their environment and alter their phenotype, giving rise to developmentally-regulated and/or pathological processes (DuFort et al., 2011). As one of the outstanding questions in cell biology and medicine,

the molecular mechanisms by which mechanical force is transduced into biochemical signals remains obscure (Roca-Cusachs et al., 2012). Single-molecule approaches (i.e. BFP, see Chapter 3) have been extensively used to study force regulation of protein-protein interactions, measure molecular elasticity and determine protein conformational changes (Chen et al., 2010; Huang et al., 2010; Chen et al., 2012), yielding significant insight into such mechanisms. For distinct receptor-ligand systems, such as interactions involved in leukocyte (Marshall et al., 2003; Chen et al., 2010) and platelet adhesions (Yago et al., 2008), bonds can be stabilized rather than disrupted by force; these bonds are termed catch bonds. Catch bonds are likely essential to key cell physiological events that occur in conditions where significant forces are experienced, such as during leukocyte adhesion to the vascular endothelium under shear stresses imposed by blood flow (McEver and Zhu, 2010; Lefort and Ley, 2012). They are also suggested to play fundamental roles in pathological progression, such as in the case of primary tumor metastasis. Two types of structural models for catch bonds have been proposed to explain how force modulates the ligand-binding interface: one based on allosteric mechanisms (Hertig and Vogel, 2012) and the other entailing a sliding-rebinding mechanism (Lou and Zhu, 2007). However, alternative mechanisms for catch bond formation may exist.

Thy-1 (CD90) is a heavily N-glycosylated single v-type immunoglobulin (Ig) domain-containing glycoprotein, probably of primordial origin within the IgSF (Campbell et al., 1981). It is localized to the outer leaflet of the plasma membrane via a C-terminal glycophosphatidylinositol (GPI)-anchor, which specifies lateral mobility within the lipid bilayer (Tiveron et al., 1994; Chen et al., 2006). Thy-1 is known to bind

integrins in a variety of tissue-specific contexts, including $\alpha_M\beta_2$ (Mac-1) on leukocytes (Wetzel et al., 2004; 2006), $\alpha_v\beta_3$ on melanoma cells (Saalbach et al., 2005) and neurons (Hermosilla et al., 2008; Avalos et al., 2009), and $\alpha_v\beta_5$ on lung fibroblasts (Zhou et al., 2010). For a full review, see (Barker and Hagood, 2009). Binding to α_v integrins is mediated by Thy-1's Arg-Leu-Asp (RLD) motif, as mutation to non-functional Arg-Leu-Glu (RLE) abolishes binding (Hermosilla et al., 2008; Avalos et al., 2009; Zhou et al., 2010). Thy-1 also binds heparin sulfate proteoglycans, including syndecan-4, through a conserved polycationic motif in the C-C' strand loop motif (Williams and Gagnon, 1982; Avalos et al., 2009). In response to inflammatory cytokines, such as TNFα or IL-1β, Thy-1 expression is induced on the endothelium where it plays a critical role in extravasation of circulating leukocytes (Wetzel et al., 2006; Schubert et al., 2011).

Integrins and syndecans are two primary receptor families that mediate adhesion, but their relative and functional contributions to cell–extracellular matrix (ECM) and cell-cell interactions remain to be investigated. Growing evidences indicate that synergistic signaling is required for proper control of adhesive function and cell phenotype regulation in response to the external environment (Bass and Humphries, 2002; Bass et al., 2007). Specifically, syndecan-4 engagement of the HepII domain of fibronectin (type III repeats 12-14) promotes intracellular signaling through PKCα, Rho family GTPases, and their GEFs and GAPs (Saoncella et al., 1999; Mostafavi-Pour et al., 2003; Dovas et al., 2006; Bass et al., 2007; 2008). This in concert with FAK, Src, and other signaling modules controlled via integrin ligation, direct adhesion assembly and maturation (Parsons et al., 2010). Interestingly, this assembly process is regulated by

mechanical force, with myosin II-mediated contractility facilitating the growth of adhesion plaques during initial adhesion assembly and maturation at the leading edge (Balaban et al., 2001; Stricker et al., 2011; Schwarz and Gardel, 2012). Intriguingly, the spatial distribution of these receptors and how synergistic signaling is regulated at the single-molecule level is largely unknown.

In this study, we used the BFP to investigate the potential force regulation of the hypothesized Thy-1–$\alpha_5\beta_1$ bond. Surprisingly, we found a complex regulation of adhesive bonds at the single-molecule level: tensile force prolongs the bond lifetime (i.e. catch bonds). In contrast to the well-known catch bonds of bimolecular systems, such as L-selectin (Marshall et al., 2003), GPIbα (Yago et al., 2008; Ju et al., 2013b)(All previous chapters) and LFA-1(Chen et al., 2010), the Thy-1–$\alpha_5\beta_1$ catch bond was strongly correlated with adhesion events showing a bond stiffening phenotype, termed dynamic bond stiffening (DBS), which required co-receptor engagement by syndecan-4 on living cells. Thus, the data strongly suggest a unique, previously unreported class of receptor-ligand bonds whereby force triggers co-receptor recognition and formation of a trimolecular complex that is required for force-mediated adhesion signaling.

8.3.1 *Thy-1–K562 adhesions are primarily mediated by Thy-1–$\alpha_5\beta_1$ bonds*

To verify the direct interaction between Thy-1 and $\alpha_5\beta_1$ integrin, we characterized single-molecule interactions between recombinant Thy-1–Fc and the $\alpha_5\beta_1$ integrin-expressing cell line, K562 (Figure 8-6 A and B) using a biomembrane force probe (BFP). As previously reported, the absence (*black trace*, Figure 8-6 C) or presence (*blue and red traces,* Figure 8-6 C) of a bond is detected by the existence of a tensile force signal upon

K562 cell retraction from the Thy-1 presenting BFP, allowing calculation of adhesion frequency from repeated touches (Figure 8-6 F). To verify binding specificities, we measured adhesion frequencies in the presence of function-blocking mAbs (see section 2.5.3). Blocking with anti-β_1 mAb significantly decreased adhesion frequency, as did stable knockdown of β_1 expression using RNAi. Using a probe not coated with Thy-1 ligand reduced adhesion frequency to nearly zero, whereas anti-β_1 mAb diminished adhesion frequency by 3-fold, but did not completely block adhesions (Figure 8-6 F). Mutation of Thy-1 (D37E) in the purported integrin-binding motif, RLD, abolished the binding in a similar manner as β_1 antibody blockade (Figure 8-6 F), confirming this as the binding motif for $\alpha_5\beta_1$. As $\alpha_5\beta_1$ is the only constitutively expressed RGD-binding integrin on K562 cells (Hemler et al., 1987), our data indicated the binding events were primarily mediated by Thy-1−$\alpha_5\beta_1$ interactions.
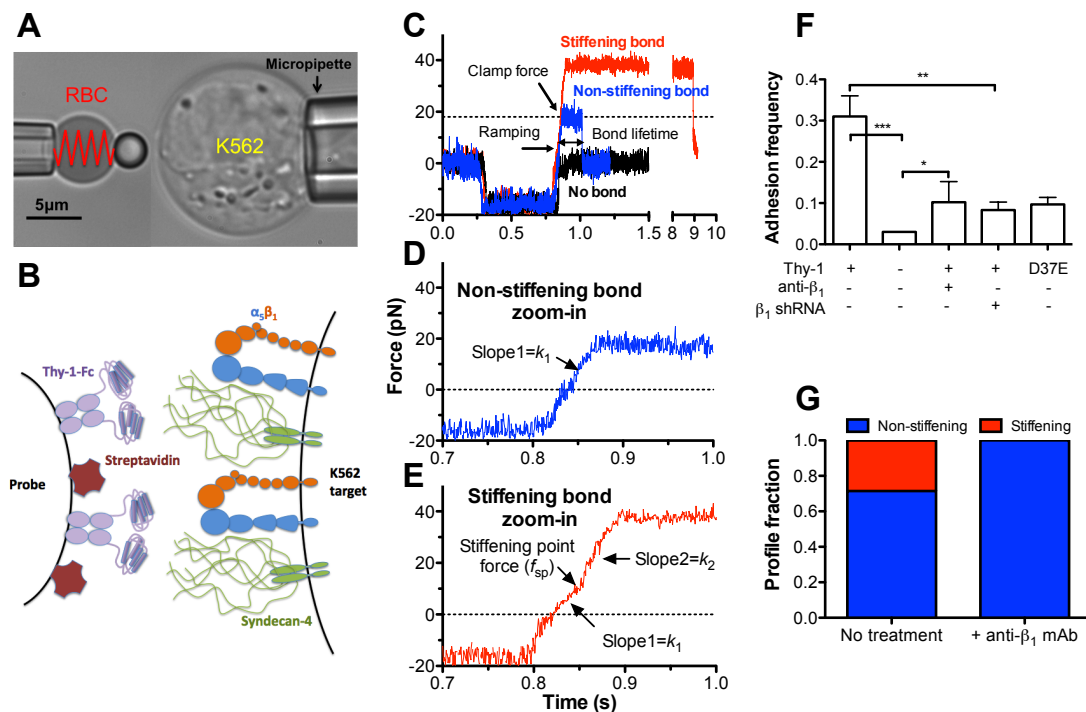
Figure 8-6. BFP setup for observing Thy-1 binding to K562 cell and molecular stiffening effect. (A) An RBC with a probe bead attached to apex (*left*) was aligned against a target K562 cell (*right*). (B) Illustration of interacting molecules. The molecules of interest: α5β1 and syndecan-4 were expressed on a target cell. Recombinant Thy-1 was coated on the probe bead. (C) Representative force vs. time plots showing no bond (black), non-stiffening bond (blue) and stiffening bond (red) events. The experiment was done in repeated cycles; each cycle consisted of four phases indicated as approach, contact, retract (force ramp), and hold (force clamp). Data (points) were acquired at 1,200 fps. (D and E) Representative force vs. time zoom-in plots in the ramping phase showing non-stiffening (D) and stiffening (E) signatures. The force at stiffening point (SP) (f_{sp}), the stiffness before SP (k_1) and after SP (k_2) are indicated. Zero forces are shown by dotted lines. (F) Binding specificity. Adhesion frequencies between K562 cells and beads coated with Thy-1, without Thy-1, with Thy-1 in the presence of 20 μg/ml anti-$β_1$ mAb (AIIB2), with Thy-1 vs. $β_1$ knockdown K562 cells, with Thy-1 mutant D37E. Data are presented as mean ± S.E.M. of 3-5 pairs of cells and beads repeatedly contacting 50 times with 0.5s each contact. * = p < 0.05; ** = p < 0.01; *** = p < 0.001, as assessed by unpaired, two-tailed Student's t-test. (G) Fraction of non-stiffening (blue) vs. stiffening (red) Thy-1–K562 bonds observed at the absence and presence of anti-$β_1$ mAb.

8.3.2   *Bond stiffening phenotype gives rise to Thy-1–K562 catch bond*

When the force-loading signatures of positive bond events were interrogated, we unexpectedly identified two types of binding events with distinct signatures: 1) a non-stiffening bond, featuring a single linear segment in the force-loading phase (Figure 8-6 D), and 2) a stiffening bond, featuring an abrupt kink signature (denoted stiffening point (SP)) that separated the force-loading phase into two linear segments, the second having a significantly steeper slope (Figure 8-6 E). The steeper slope within the force-loading regime strongly suggested an abrupt increase in the stiffness of the total bond. Stiffening bonds also often displayed longer lifetimes, as compared to the short lifetimes of non-stiffening bonds (Figure 8-6 C). The prevalence of the stiffening events over total bond events was approximately 30%.   Addition of the function-blocking anti-$β_1$ mAb completely eliminated the stiffening effect (Figure 8-6 G).

135
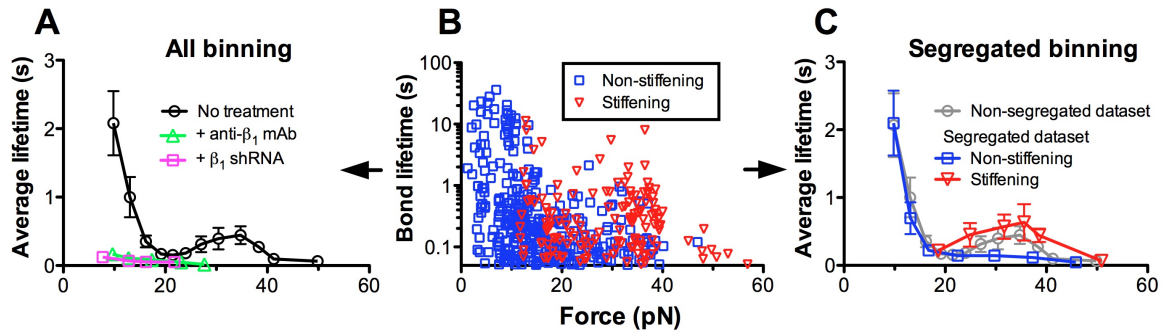
Figure 8-7. Stiffening effect prolongs the bond lifetime under force. (A) Plots of lifetime (mean ± S.E.M.) vs. force of Thy-1–K562 bonds at absence (circle), presence (triangle) of 20 µg/ml β_1 blocking mAb and with β_1 knockdown K562 cells (square). The data were derived by binning the raw data in panel B by force and averaging lifetimes in each force bin. (B) Scatter plots of bond lifetimes vs. corresponding clamp forces. Each individual lifetime (scatter point) was measured from every bond event as shown in Figure 8-6 C. Bond signatures: non-stiffening and stiffening were color-coded in blue and red respectively. (C) Plots of lifetime (mean ± S.E.M.) vs. force for non-stiffening (blue square), stiffening (red triangle) events by binning each population separately. The non-segregated data (A, circle), binning the non-stiffening and stiffening events together, are also referenced (gray circle) and compared.

When the Thy-1–K562 average bond lifetimes were plotted against force, a striking triphasic force dependency was observed (Figure 8-7 A). Specifically, classic slip bonds were observed in the regime <20 pN, catch bonds were observed from 20-40 pN, and after reaching the maxima, a second slip bond regime >40pN was observed. By comparison, anti-β_1 blocking mAb or RNAi significantly decreased bond lifetimes and the slip-catch-slip triphasic profile was abolished; only short-lived bonds remained (Figure 8-7 A). When individual bond events were color-coded based on the two distinct signatures in the force-loading phase, an intriguing discrimination between the two populations emerged. The non-stiffening events distributed universally over the entire force range, while stiffening events only occur at the force regime of >15 pN. Moreover, the stiffening events consistently demonstrated long lifetimes and mostly clustered in the force regime of 20-40 pN, overlapping the catch-bond regime (Figure 8-7 B). Segregating the force-dependent lifetimes (all data; *gray*, Figure 8-7 C) for each

136

population convincingly demonstrates that the non-stiffening events (*blue*, Figure 8-7 C) are responsible for the slip regime, while the stiffening events (*red*, Figure 8-7 C) are primarily responsible for the catch bond regime. Catch bonds in the high force regime were solely contributed by the stiffening bonds. Thus we term this novel phenomenon "Dynamic bond stiffening" or DBS, as the molecular bond is both mechanically stiffened and increased in lifetime in response to an applied force over the sub-second timescale.

8.3.3 *Syndecan-4 is a co-receptor for Thy-1 required for DBS and lifetime prolongation.*

Partial blocking by anti-β_1 mAb suggested an additional adhesive interaction between the cell surface and Thy-1 (Figure 8-6 F). It was reported that Thy-1 contains a putative polycationic heparin binding sequence, which mediates binding to the heparin sulfate proteoglycan (HSPG), syndecan-4 and activation of PKCα (Avalos et al., 2009). When K562 cells were pretreated with heparinase to cleave heparin sulfate glycosaminoglycans (GAGs), a hairy structure, from the cell surface, adhesions were partially blocked (Figure 8-8 A). Using K562 cells with syndecan-4 (Syn4) knockdown by siRNA showed similar results. Dual inhibitions of K562 cells on $\alpha_5\beta_1$ and Syn4 (with both anti-β_1 and Syn4 siRNA, or the combination of β_1 knockdown and heparinase) abrogated the total Thy-1–K562 adhesions to the level of non-specific binding (Figure 8-8 A). These results suggested that HSPGs, in particular syndecan-4, is a co-receptor for Thy-1.

In addition, we found that the treatments of heparinase or Syn4 RNAi almost entirely eliminated the stiffening bond phenotype (Figure 8-8 B and C). Force was no longer able to prolong the Thy-1–K562 bond lifetime with these treatments, and therefore DBS was completely abrogated (Figure 8-8 D); Therefore, co-receptor engagement is

intimately connected with the bond stiffening phenotype, catch bonds, and DBS. Furthermore, this suggests that co-receptor Syn4 engagement could be visualized with the BFP via the stiffening signature in the bond-loading profile.
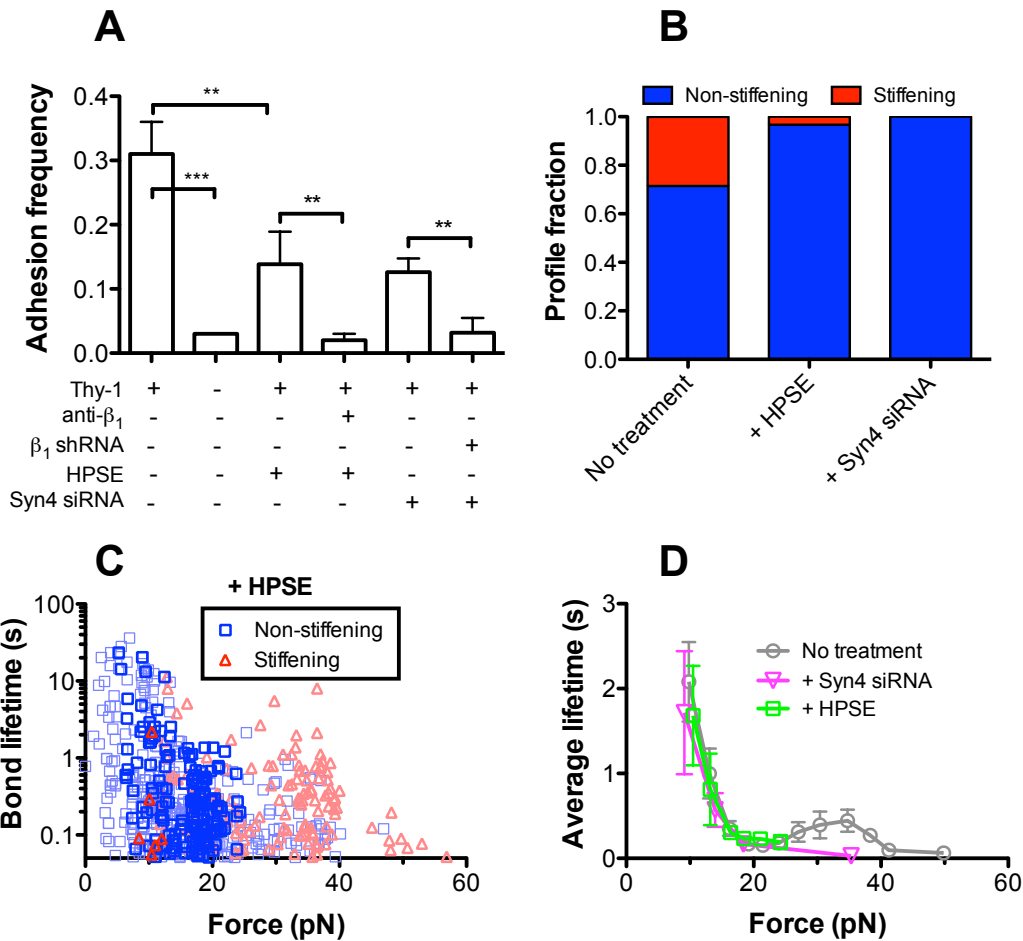
Figure 8-8. HSPG engagement is required for the stiffening effect and force-mediated lifetime prolongation. (*A*) Adhesion frequencies of the Thy-1 binding to K562 cell at indicated conditions. Frequencies measured using syndecan-4 (Syn4) knockdown K562 cells with and without β_1 integrin blocking mAbs in solution are also shown. The normal and β_1 knockdown K562 cells were pre-treated with HPSE to block Thy-1 binding to heparin sulfate as negative controls. The same keys are used as Figure 2F. (*B*) Fraction of non-stiffening (blue) vs. stiffening (red) Thy-1–K562 bonds at the absence and presence of HPSE and those with Syn4 siRNA in K562 cells. (*C*) Scatter plots of bond lifetimes vs. corresponding clamp forces for HPSE treated K562 cells. The measurements and color-coding are the same as the data of Figure 3*B*, which is dimmed out as the background. The same keys are shared with Figure 3*B*. (*D*) Plots of lifetime (mean ± S.E.M.) vs. force of Thy-1–K562 bonds at absence of any treatment (gray circles), with syndecan-4 knockdown K562 cells (magenta triangles), with HPSE treated K562 cells (green squares). Column graphs of data depicted in *B-D* are shown as mean ± S.E.M**.** * = p < 0.05; ** = p < 0.01; *** = p < 0.001, as assessed by unpaired, two-tailed Student's t-test.

REFERENCES

Andrews, R., and Berndt, M. (2004). Platelet physiology and thrombosis. Thrombosis Research *114*, 447–453.

Andrews, R.K., Booth, W.J., Gorman, J.J., Castaldi, P.A., and Berndt, M.C. (1989). Purification of botrocetin from Bothrops jararaca venom. Analysis of the botrocetin-mediated interaction between von Willebrand factor and the human platelet membrane glycoprotein Ib-IX complex. Biochemistry *28*, 8317–8326.

Arya, M., Anvari, B., Romo, G.M., Cruz, M.A., Dong, J.-F., Mcintire, L.V., Moake, J.L., and López, J.A. (2002). Ultralarge multimers of von Willebrand factor form spontaneous high-strength bonds with the platelet glycoprotein Ib-IX complex: studies using optical tweezers. Blood *99*, 3971–3977.

Auton, M., Cruz, M.A., and Moake, J. (2007). Conformational stability and domain unfolding of the Von Willebrand factor A domains. J. Mol. Biol. *366*, 986–1000.

Auton, M., Sedlák, E., Marek, J., Wu, T., Zhu, C., and Cruz, M. (2009). Changes in thermodynamic stability of von Willebrand factor differentially affect the force-dependent binding to platelet GPIb [alpha]. Biophys J *97*, 618–627.

Auton, M., Sowa, K.E., Behymer, M., and Cruz, M.A. (2012). N-terminal flanking region of A1 domain in von Willebrand factor stabilizes structure of A1A2A3 complex and modulates platelet activation under shear stress. J Biol Chem *287*, 14579–14585.

Auton, M., Sowa, K.E., Smith, S.M., Sedlák, E., Vijayan, K.V., and Cruz, M.A. (2010a). Destabilization of the A1 domain in von Willebrand factor dissociates the A1A2A3 tri-domain and provokes spontaneous binding to glycoprotein Ibalpha and platelet activation under shear stress. J Biol Chem *285*, 22831–22839.

Auton, M., Zhu, C., and Cruz, M.A. (2010b). The Mechanism of VWF-Mediated Platelet GPIbα Binding. Biophys J *99*, 1192–1201.

Avalos, A.M., Valdivia, A.D., Muñoz, N., Herrera-Molina, R., Tapia, J.C., Lavandero, S., Chiong, M., Burridge, K., Schneider, P., Quest, A.F.G., et al. (2009). Neuronal Thy-1 induces astrocyte adhesion by engaging syndecan-4 in a cooperative interaction with alphavbeta3 integrin that activates PKCalpha and RhoA. J Cell Sci *122*, 3462–3471.

Azuma, H., Dent, J.A., Sugimoto, M., Ruggeri, Z.M., and Ware, J. (1991). Independent assembly and secretion of a dimeric adhesive domain of von Willebrand factor containing the glycoprotein Ib-binding site. J Biol Chem *266*, 12342–12347.

Balaban, N.Q., Schwarz, U.S., Riveline, D., Goichberg, P., Tzur, G., Sabanay, I., Mahalu, D., Safran, S., Bershadsky, A., Addadi, L., et al. (2001). Force and focal adhesion assembly: a close relationship studied using elastic micropatterned substrates. Nat. Cell. Biol *3*, 466–472.

Barg, A., Ossig, R., Goerge, T., Schneider, M.F., Schillers, H., Oberleithner, H., and Schneider, S.W. (2007). Soluble plasma-derived von Willebrand factor assembles to a haemostatically active filamentous network. Thrombosis and Haemostasis *97*, 514–526.

Barker, T.H., and Hagood, J.S. (2009). Getting a grip on Thy-1 signaling. Biochim. Biophys. Acta *1793*, 921–923.

Bass, M., and Humphries, M. (2002). Cytoplasmic interactions of syndecan-4 orchestrate adhesion receptor and growth factor receptor signalling. Biochem J *368*, 1.

Bass, M.D., Morgan, M.R., Roach, K.A., Settleman, J., Goryachev, A.B., and Humphries, M.J. (2008). p190RhoGAP is the convergence point of adhesion signals from alpha 5 beta 1 integrin and syndecan-4. J Cell Biol *181*, 1013–1026.

Bass, M.D., Roach, K.A., Morgan, M.R., Mostafavi-Pour, Z., Schoen, T., Muramatsu, T., Mayer, U., Ballestrem, C., Spatz, J.P., and Humphries, M.J. (2007). Syndecan-4-dependent Rac1 regulation determines directional migration in response to the extracellular matrix. J Cell Biol *177*, 527–538.

Baumgartner, H.R., Turitto, V., and Weiss, H.J. (1980). Effect of shear rate on platelet interaction with subendothelium in citrated and native blood. II. Relationships among platelet adhesion, thrombus dimensions, and fibrin formation. J. Lab. Clin. Med. *95*, 208–221.

Bergmeier, W., Piffath, C.L., Goerge, T., Cifuni, S.M., Ruggeri, Z.M., Ware, J., and Wagner, D.D. (2006). The role of platelet adhesion receptor GPIbalpha far exceeds that of its main ligand, von Willebrand factor, in arterial thrombosis. Proc Natl Acad Sci USA *103*, 16900–16905.

Brugués, J., Maugis, B., Casademunt, J., Nassoy, P., Amblard, F., and Sens, P. (2010). Dynamical organization of the cytoskeletal cortex probed by micropipette aspiration. Proc Natl Acad Sci USA *107*, 15415–15420.

Campbell, D.G., Gagnon, J., Reid, K.B., and Williams, A.F. (1981). Rat brain Thy-1 glycoprotein. The amino acid sequence, disulphide bonds and an unusual hydrophobic region. Biochem J *195*, 15–30.

Celikel, R., Ruggeri, Z.M., and Varughese, K.I. (2000). von Willebrand factor conformation and adhesive function is modulated by an internalized water molecule. Nat. Struct. Biol. *7*, 881–884.

Celikel, R., Varughese, K.I., Madhusudan, Yoshioka, A., Ware, J., and Ruggeri, Z.M. (1998). Crystal structure of the von Willebrand factor A1 domain in complex with the

function blocking NMC-4 Fab. Nat. Struct. Biol. *5*, 189–194.

Chen, W. (2009). The Force Regulation on Binding Kinetics and Conformations of Integrin and Selectins Using a Biomembrane Force Probe. Ph.D. Thesis, Ga Inst. Technol., Atlanta 1–166.

Chen, W., Evans, E.A., McEver, R.P., and Zhu, C. (2008a). Monitoring receptor-ligand interactions between surfaces by thermal fluctuations. Biophys J *94*, 694–701.

Chen, W., Lou, J., and Zhu, C. (2010). Forcing switch from short- to intermediate- and long-lived states of the A domain generates LFA-1/ICAM-1 catch bonds. J Biol Chem *285*, 35967–35978.

Chen, W., Lou, J., Evans, E.A., and Zhu, C. (2012). Observing force-regulated conformational changes and ligand dissociation from a single integrin on cells. J Cell Biol *199*, 497–512.

Chen, W., Zarnitsyna, V.I., Sarangapani, K.K., Huang, J., and Zhu, C. (2008b). Measuring Receptor–Ligand Binding Kinetics on Cell Surfaces: From Adhesion Frequency to Thermal Fluctuation Methods. Cel. Mol. Bioeng. *1*, 276–288.

Chen, Y., Aardema, J., Kale, S., Whichard, Z.L., Awomolo, A., Blanchard, E., Chang, B., Myers, D.R., Ju, L., Tran, R., et al. (2013). Loss of the F-BAR protein CIP4 reduces platelet production by impairing membrane-cytoskeleton remodeling. Blood *122*, 1695–1706.

Chen, Y., Thelin, W.R., Yang, B., Milgram, S.L., and Jacobson, K. (2006). Transient anchorage of cross-linked glycosyl-phosphatidylinositol-anchored proteins depends on cholesterol, Src family kinases, caveolin, and phosphoinositides. J Cell Biol *175*, 169–178.

Chesla, S., Selvaraj, P., and Zhu, C. (1998). Measuring two-dimensional receptor-ligand binding kinetics by micropipette. Biophys J *75*, 1553–1572.

Clemetson, J.M., and Uff, S. (2002). Crystal structure of the platelet glycoprotein Ibalpha N-terminal domain reveals an unmasking mechanism for receptor activation. J Biol Chem *277*, 35657–35663.

Clemetson, K., Naim, H., and Lüscher, E. (1981). Relationship between glycocalicin and glycoprotein Ib of human platelets. Proceedings of the National Academy of Sciences *78*, 2712.

Clemetson, K.J. (2007). A short history of platelet glycoprotein Ib complex. Thrombosis and Haemostasis *98*, 63–68.

Coburn, L., Damaraju, V., Dozic, S., and Eskin, S. (2011). GPIb [alpha]-vWF rolling under shear stress shows differences between type 2B and 2M von Willebrand disease. Biophys J *100*, 304–312.

Colace, T.V., and Diamond, S.L. (2013). Direct observation of von Willebrand factor elongation and fiber formation on collagen during acute whole blood exposure to pathological flow. Arteriosclerosis, Thrombosis, and Vascular Biology *33*, 105–113.

Cruz, M.A., and Handin, R.I. (1993). The interaction of the von Willebrand factor-A1 domain with platelet glycoprotein Ib/IX. J Biol Chem *268*, 21238–21245.

Cruz, M.A., Chen, J., Whitelock, J.L., Morales, L.D., and López, J.A. (2005). The platelet glycoprotein Ib-von Willebrand factor interaction activates the collagen receptor alpha2beta1 to bind collagen: activation-dependent conformational change of the alpha2-I domain. Blood *105*, 1986–1991.

Cruz, M.A., Diacovo, T.G., Emsley, J., Liddington, R., and Handin, R.I. (2000). Mapping the glycoprotein Ib-binding site in the von willebrand factor A1 domain. J Biol Chem *275*, 19098–19105.

Doggett, T.A. (2003). Alterations in the intrinsic properties of the GPIb -VWF tether bond define the kinetics of the platelet-type von Willebrand disease mutation, Gly233Val. Blood *102*, 152–160.

Doggett, T.A., Girdhar, G., Lawshé, A., Schmidtke, D.W., Laurenzi, I.J., Diamond, S.L., and Diacovo, T.G. (2002). Selectin-like kinetics and biomechanics promote rapid platelet adhesion in flow: the GPIb(alpha)-vWF tether bond. Biophys J *83*, 194–205.

Dong, J., Berndt, M., Schade, A., McIntire, L., Andrews, R., and Lopez, J. (2001). Ristocetin-dependent, but not botrocetin-dependent, binding of von Willebrand factor to the platelet glycoprotein Ib-IX-V complex correlates with shear-dependent interactions. Blood *97*, 162.

Dong, J., Schade, A.J., Romo, G.M., Andrews, R.K., Gao, S., McIntire, L.V., and Lopez, J.A. (2000). Novel gain-of-function mutations of platelet glycoprotein IBalpha by valine mutagenesis in the Cys209-Cys248 disulfide loop. Functional analysis under statis and dynamic conditions. J Biol Chem *275*, 27663–27670.

Dong, J.-F., Moake, J.L., Nolasco, L., Bernardo, A., Arceneaux, W., Shrimpton, C.N., Schade, A.J., Mcintire, L.V., Fujikawa, K., and López, J.A. (2002). ADAMTS-13 rapidly cleaves newly secreted ultralarge von Willebrand factor multimers on the endothelial surface under flowing conditions. Blood *100*, 4033–4039.

Dong, J.F. (2001). Tyrosine Sulfation of Glycoprotein Ibalpha . ROLE OF ELECTROSTATIC INTERACTIONS IN VON WILLEBRAND FACTOR BINDING. Journal of Biological Chemistry *276*, 16690–16694.

Dovas, A., Yoneda, A., and Couchman, J.R. (2006). PKCbeta-dependent activation of RhoA by syndecan-4 during focal adhesion formation. J Cell Sci *119*, 2837–2846.

Du, X. (2007). Signaling and regulation of the platelet glycoprotein Ib-IX-V complex. Current Opinion in Hematology *14*, 262.

DuFort, C.C., Paszek, M.J., and Weaver, V.M. (2011). Balancing forces: architectural control of mechanotransduction. Nat Rev Mol Cell Biol *12*, 308–319.

Dumas, J.J., Kumar, R., McDonagh, T., Sullivan, F., Stahl, M.L., Somers, W.S., and Mosyak, L. (2004). Crystal structure of the wild-type von Willebrand factor A1-glycoprotein Ibalpha complex reveals conformation differences with a complex bearing von Willebrand disease mutations. J Biol Chem *279*, 23327–23334.

Dustin, M.L., Bromley, S.K., Davis, M.M., and Zhu, C. (2001). Identification of self through two-dimensional chemistry and synapses. Annu. Rev. Cell Dev. Biol. *17*, 133–157.

Emsley, J., Cruz, M., Handin, R., and Liddington, R. (1998). Crystal structure of the von Willebrand Factor A1 domain and implications for the binding of platelet glycoprotein Ib. J Biol Chem *273*, 10396–10401.

Evans, E., Ritchie, K., and Merkel, R. (1995). Sensitive force technique to probe molecular adhesion and structural linkages at biological interfaces. Biophys J *68*, 2580–2587.

Federici, A.B., Mannucci, P.M., Stabile, F., Canciani, M.T., Di Rocco, N., Miyata, S., Ware, J., and Ruggeri, Z.M. (1997). A type 2b von Willebrand disease mutation (Ile546-->Val) associated with an unusual phenotype. Thrombosis and Haemostasis *78*, 1132–1137.

Finger, E.B., Puri, K.D., Alon, R., Lawrence, M.B., Andrian, von, U.H., and Springer, T.A. (1996). Adhesion through L-selectin requires a threshold hydrodynamic shear. Nature *379*, 266–269.

Fox, J.E., Aggerbeck, L.P., and Berndt, M.C. (1988). Structure of the glycoprotein Ib.IX complex from platelet membranes. J Biol Chem *263*, 4882–4890.

Fukuda, K., Doggett, T., Laurenzi, I.J., Liddington, R.C., and Diacovo, T.G. (2005). The snake venom protein botrocetin acts as a biological brace to promote dysfunctional platelet aggregation. Nat Struct Mol Biol *12*, 152–159.

Gandhi, C., Khan, M.M., Lentz, S.R., and Chauhan, A.K. (2012). ADAMTS13 reduces vascular inflammation and the development of early atherosclerosis in mice. Blood *119*, 2385–2391.

Gelles, J., Schnapp, B.J., and Sheetz, M.P. (1988). Tracking kinesin-driven movements with nanometre-scale precision. Nature *331*, 450–453.

Gilden, J., and Krummel, M.F. (2010). Control of cortical rigidity by the cytoskeleton: emerging roles for septins. Cytoskeleton (Hoboken) *67*, 477–486.

Girma, J.P., Takahashi, Y., Yoshioka, A., Diaz, J., and Meyer, D. (1990). Ristocetin and botrocetin involve two distinct domains of von Willebrand factor for binding to platelet

membrane glycoprotein Ib. Thrombosis and Haemostasis *64*, 326–332.

Gutierrez, E., Petrich, B.G., Shattil, S.J., Ginsberg, M.H., Groisman, A., and Kasirer-Friede, A. (2008). Microfluidic devices for studies of shear-dependent platelet adhesion. Lab Chip *8*, 1486–1495.

Heinrich, V., Leung, A., and Evans, E. (2005). Nano-to-microscale mechanical switches and fuses mediate adhesive contacts between leukocytes and the endothelium. J Chem Inf Model *45*, 1482–1490.

Hemler, M.E., Huang, C., Takada, Y., Schwarz, L., Strominger, J.L., and Clabby, M.L. (1987). Characterization of the cell surface heterodimer VLA-4 and related peptides. J Biol Chem *262*, 11478–11485.

Hermosilla, T., Muñoz, D., Herrera-Molina, R., Valdivia, A., Muñoz, N., Nham, S.-U., Schneider, P., Burridge, K., Quest, A.F.G., and Leyton, L. (2008). Direct Thy-1/alphaVbeta3 integrin interaction mediates neuron to astrocyte communication. Biochim. Biophys. Acta *1783*, 1111–1120.

Hertig, S., and Vogel, V. (2012). Catch bonds. Curr. Biol. *22*, R823–R825.

Hochmuth, R.M. (2000). Micropipette aspiration of living cells. J Biomech *33*, 15–22.

Huang, J., Zarnitsyna, V., Liu, B., Edwards, L., Jiang, N., Evavold, B., and Zhu, C. (2010). The kinetics of two-dimensional TCR and pMHC interactions determine T-cell responsiveness. Nature *464*, 932–936.

Huizinga, E.G., Tsuji, S., Romijn, R.A.P., Schiphorst, M.E., de Groot, P.G., Sixma, J.J., and Gros, P. (2002). Structures of glycoprotein Ibalpha and its complex with von Willebrand factor A1 domain. Science *297*, 1176–1179.

Jackson, S.P. (2011). Arterial thrombosis--insidious, unpredictable and deadly. Nat Med *17*, 1423–1436.

Jackson, S.P., Mistry, N., and Yuan, Y. (2000). Platelets and the injured vessel wall--"rolling into action": focus on glycoprotein Ib/V/IX and the platelet cytoskeleton. Trends Cardiovasc. Med. *10*, 192–197.

Jackson, S.P., Nesbitt, W.S., and Westein, E. (2009). Dynamics of platelet thrombus formation. J Thromb Haemost *7*, 17–20.

Ju, L., Dong, J.-F., Cruz, M.A., and Zhu, C. (2013a). N-terminal flanking region of VWF-A1 regulates its triphasic force-dependent dissociation from GPIbα. Blood.

Ju, L., Dong, J.-F., Cruz, M.A., and Zhu, C. (2013b). The N-terminal flanking region of the A1 domain regulates the force-dependent binding of von Willebrand factor to platelet glycoprotein Ibα. Journal of Biological Chemistry.

Ju, L., Wang, Y.D., Hung, Y., Wu, C.-F.J., and Zhu, C. (2013c). An HMM-based algorithm for evaluating rates of receptor-ligand binding kinetics from thermal fluctuation data. Bioinformatics *29*, 1511–1518.

Kasirer-Friede, A., Cozzi, M.R., Mazzucato, M., De Marco, L., Ruggeri, Z.M., and Shattil, S.J. (2004). Signaling through GP Ib-IX-V activates alpha IIb beta 3 independently of other receptors. Blood *103*, 3403–3411.

Kasirer-Friede, A., Ware, J., Leng, L., Marchese, P., Ruggeri, Z.M., and Shattil, S.J. (2002). Lateral clustering of platelet GP Ib-IX complexes leads to up-regulation of the adhesive function of integrin alpha IIbbeta 3. J Biol Chem *277*, 11949–11956.

Keuren, J.F.W., Baruch, D., Legendre, P., Denis, C.V., Lenting, P.J., Girma, J.-P., and Lindhout, T. (2004). von Willebrand factor C1C2 domain is involved in platelet adhesion to polymerized fibrin at high shear rate. Blood *103*, 1741–1746.

Kim, J., Zhang, C.-Z., Zhang, X., and Springer, T.A. (2010). A mechanically stabilized receptor-ligand flex-bond important in the vasculature. Nature *466*, 992–995.

Kong, F., Garcia, A.J., Mould, A.P., Humphries, M.J., and Zhu, C. (2009). Demonstration of catch bonds between an integrin and its ligand. J Cell Biol *185*, 1275–1284.

Kong, F., Li, Z., Parks, W.M., Dumbauld, D.W., García, A.J., Mould, A.P., Humphries, M.J., and Zhu, C. (2013). Cyclic Mechanical Reinforcement of Integrin-Ligand Interactions. Molecular Cell.

Kumar, R.A., Dong, J.-F., Thaggard, J.A., Cruz, M.A., López, J.A., and Mcintire, L.V. (2003). Kinetics of GPIbalpha-vWF-A1 tether bond under flow: effect of GPIbalpha mutations on the association and dissociation rates. Biophys J *85*, 4099–4109.

Kuwahara, M., Sugimoto, M., Tsuji, S., Miyata, S., and Yoshioka, A. (1999). Cytosolic calcium changes in a process of platelet adhesion and cohesion on a von Willebrand factor-coated surface under flow conditions. Blood *94*, 1149–1155.

Lawler, J., and Hynes, R.O. (1989). An integrin receptor on normal and thrombasthenic platelets that binds thrombospondin. Blood *74*, 2022–2027.

Le Trong, I., Aprikian, P., Kidd, B.A., Forero-Shelton, M., Tchesnokova, V., Rajagopal, P., Rodriguez, V., Interlandi, G., Klevit, R., Vogel, V., et al. (2010). Structural basis for mechanical force regulation of the adhesin FimH via finger trap-like β sheet twisting. Cell *141*, 645–655.

Lefort, C.T., and Ley, K. (2012). Neutrophil arrest by LFA-1 activation. Front Immunol *3*, 157.

Lenting, P., Pegon, J., Groot, E., and de Groot, P. (2010). Regulation of von Willebrand factor-platelet interactions. Thrombosis and Haemostasis *104*, 104.

146

Li, R., and Emsley, J. (2013). The organizing principle of the platelet glycoprotein Ib-IX-V complex. Journal of Thrombosis and Haemostasis *11*, 605–614.

Long, M., Chen, J., Jiang, N., Selvaraj, P., McEver, R.P., and Zhu, C. (2006). Probabilistic modeling of rosette formation. Biophys J *91*, 352–363.

Lou, J., and Zhu, C. (2007). A structure-based sliding-rebinding mechanism for catch bonds. Biophys J *92*, 1471–1485.

Lou, J., and Zhu, C. (2008). Flow induces loop-to-beta-hairpin transition on the beta-switch of platelet glycoprotein Ib alpha. Proc Natl Acad Sci USA *105*, 13847–13852.

Lou, J., Yago, T., Klopocki, A.G., Mehta, P., Chen, W., Zarnitsyna, V.I., Bovin, N.V., Zhu, C., and McEver, R.P. (2006). Flow-enhanced adhesion regulated by a selectin interdomain hinge. J Cell Biol *174*, 1107–1117.

Luo, S.-Z., Mo, X., Afshar-Kharghan, V., Srinivasan, S., López, J.A., and Li, R. (2007). Glycoprotein Ibalpha forms disulfide bonds with 2 glycoprotein Ibbeta subunits in the resting platelet. Blood *109*, 603–609.

MacKerell, A.D., Bashford, D., Bellott, Dunbrack, R.L., Evanseck, J.D., Field, M.J., Fischer, S., Gao, J., Guo, H., Ha, S., et al. (1998). All-Atom Empirical Potential for Molecular Modeling and Dynamics Studies of Proteins †. J. Phys. Chem. B *102*, 3586–3616.

Marchese, P., Saldívar, E., Ware, J., and Ruggeri, Z. (1999). Adhesive properties of the isolated amino-terminal domain of platelet glycoprotein Ibα in a flow field. Proc Natl Acad Sci *96*, 7837.

Marshall, B.T., Long, M., Piper, J.W., Yago, T., McEver, R.P., and Zhu, C. (2003). Direct observation of catch bonds involving cell-adhesion molecules. Nature *423*, 190–193.

Marshall, B.T., Sarangapani, K.K., Wu, J., Lawrence, M.B., McEver, R.P., and Zhu, C. (2006). Measuring molecular elasticity by atomic force microscope cantilever fluctuations. Biophys J *90*, 681–692.

Martin, C., Morales, L.D., and Cruz, M.A. (2007). Purified A2 domain of von Willebrand factor binds to the active conformation of von Willebrand factor and blocks the interaction with platelet glycoprotein Ibalpha. J Thromb Haemost *5*, 1363–1370.

Matsushita, T., and Sadler, J.E. (1995). Identification of amino acid residues essential for von Willebrand factor binding to platelet glycoprotein Ib. Charged-to-alanine scanning mutagenesis of the A1 domain of human von Willebrand factor. J Biol Chem *270*, 13406–13414.

Matuskova, J., Chauhan, A.K., Cambien, B., Astrof, S., Dole, V.S., Piffath, C.L., Hynes, R.O., and Wagner, D.D. (2006). Decreased plasma fibronectin leads to delayed thrombus

growth in injured arterioles. Arteriosclerosis, Thrombosis, and Vascular Biology *26*, 1391–1396.

Maxwell, M.J., Westein, E., Nesbitt, W.S., Giuliano, S., Dopheide, S.M., and Jackson, S.P. (2007). Identification of a 2-stage platelet aggregation process mediating shear-dependent thrombus formation. Blood *109*, 566–576.

Mazzucato, M., Cozzi, M.R., Battiston, M., Jandrot-Perrus, M., Mongiat, M., Marchese, P., Kunicki, T.J., Ruggeri, Z.M., and De Marco, L. (2009). Distinct spatio-temporal Ca2+ signaling elicited by integrin alpha2beta1 and glycoprotein VI under flow. Blood *114*, 2793–2801.

Mazzucato, M., Pradella, P., Cozzi, M.R., De Marco, L., and Ruggeri, Z.M. (2002). Sequential cytoplasmic calcium signals in a 2-stage platelet activation process induced by the glycoprotein Ibalpha mechanoreceptor. Blood *100*, 2793–2800.

Mazzucato, M., Santomaso, A., Canu, P., Ruggeri, Z.M., and De Marco, L. (2007). Flow dynamics and haemostasis. Ann. Ist. Super. Sanita *43*, 130–138.

McEver, R.P., and Zhu, C. (2010). Rolling cell adhesion. Annu. Rev. Cell Dev. Biol. *26*, 363–396.

Mehta, A.D., Finer, J.T., and Spudich, J.A. (1997). Detection of single-molecule interactions using correlated thermal diffusion. Proc Natl Acad Sci USA *94*, 7927–7931.

Mekrache, M., Bachelot-Loza, C., Ajzenberg, N., Saci, A., Legendre, P., and Baruch, D. (2003). Activation of pp125FAK by type 2B recombinant von Willebrand factor binding to platelet GPIb at a high shear rate occurs independently of alpha IIb beta 3 engagement. Blood *101*, 4363–4371.

Miller, J.L., CUNNINGHAM, D., Lyle, V.A., and Finch, C.N. (1991). Mutation in the gene encoding the alpha chain of platelet glycoprotein Ib in platelet-type von Willebrand disease. Proc Natl Acad Sci USA *88*, 4761–4765.

Miura, S., Li, C.Q., Cao, Z., Wang, H., Wardell, M.R., and Sadler, J.E. (2000). Interaction of von Willebrand factor domain A1 with platelet glycoprotein Ibalpha-(1-289). Slow intrinsic binding kinetics mediate rapid platelet adhesion. J Biol Chem *275*, 7539–7546.

Miyata, S., and Ruggeri, Z.M. (1999). Distinct structural attributes regulating von Willebrand factor A1 domain interaction with platelet glycoprotein Ibalpha under flow. J Biol Chem *274*, 6586–6593.

Mo, X., Liu, L., Lopez, J.A., and Li, R. (2012). Transmembrane domains are critical to the interaction between platelet glycoprotein V and glycoprotein Ib-IX complex. J Thromb Haemost *10*, 1875–1886.

Mohri, H., Fujimura, Y., Shima, M., Yoshioka, A., Houghten, R.A., Ruggeri, Z.M., and

Zimmerman, T.S. (1988). Structure of the von Willebrand factor domain interacting with glycoprotein Ib. J Biol Chem *263*, 17901–17904.

Molloy, J.E., Burns, J.E., Kendrick-Jones, J., Tregear, R.T., and White, D.C. (1995). Movement and force produced by a single myosin head. Nature *378*, 209–212.

Morales, L.D., Martin, C., and Cruz, M.A. (2006). The interaction of von Willebrand factor-A1 domain with collagen: mutation G1324S (type 2M von Willebrand disease) impairs the conformational change in A1 domain induced by collagen. J Thromb Haemost *4*, 417–425.

Moriki, T., MURATA, M., Kitaguchi, T., Anbo, H., Handa, M., Watanabe, K., Takahashi, H., and Ikeda, Y. (1997). Expression and functional characterization of an abnormal platelet membrane glycoprotein Ib alpha (Met239 --> Val) reported in patients with platelet-type von Willebrand disease. Blood *90*, 698–705.

Morris, G.M., Huey, R., Lindstrom, W., Sanner, M.F., Belew, R.K., Goodsell, D.S., and Olson, A.J. (2009). AutoDock4 and AutoDockTools4: Automated docking with selective receptor flexibility. J Comput Chem *30*, 2785–2791.

Mostafavi-Pour, Z., Askari, J.A., Parkinson, S.J., Parker, P.J., Ng, T.T.C., and Humphries, M.J. (2003). Integrin-specific signaling pathways controlling focal adhesion formation and cell migration. J Cell Biol *161*, 155–167.

MURATA, M., Russell, S.R., Ruggeri, Z.M., and Ware, J. (1993). Expression of the phenotypic abnormality of platelet-type von Willebrand disease in a recombinant glycoprotein Ib alpha fragment. J Clin Invest *91*, 2133–2137.

Navdaev, A., and Clemetson, K.J. (2002). Glycoprotein Ib cross-linking/ligation on echicetin-coated surfaces or echicetin-IgMkappa in stirred suspension activates platelets by cytoskeleton modulated calcium release. J Biol Chem *277*, 45928–45934.

Nesbitt, W., Westein, E., Tovar-Lopez, F., Tolouei, E., Mitchell, A., Fu, J., Carberry, J., Fouras, A., and Jackson, S. (2009). A shear gradient–dependent platelet aggregation mechanism drives thrombus formation. Nat Med *15*, 665–673.

Nesbitt, W.S., Giuliano, S., Kulkarni, S., Dopheide, S.M., Harper, I.S., and Jackson, S.P. (2003). Intercellular calcium communication regulates platelet aggregation and thrombus growth. Journal of Cell Biology *160*, 1151–1161.

Nesbitt, W.S., Kulkarni, S., Giuliano, S., Goncalves, I., Dopheide, S.M., Yap, C.L., Harper, I.S., Salem, H.H., and Jackson, S.P. (2002). Distinct glycoprotein Ib/V/IX and integrin alpha IIbbeta 3-dependent calcium signals cooperatively regulate platelet adhesion under flow. J Biol Chem *277*, 2965–2972.

Ni, H., Yuen, P.S.T., Papalia, J.M., Trevithick, J.E., Sakai, T., Fässler, R., Hynes, R.O., and Wagner, D.D. (2003). Plasma fibronectin promotes thrombus growth and stability in injured arterioles. Proc Natl Acad Sci USA *100*, 2415–2419.

Okada, Y., Nishikawa, J.-I., Semma, M., and Ichikawa, A. (2011). Induction of integrin β3 in PGE₂-stimulated adhesion of mastocytoma P-815 cells to the Arg-Gly-Asp-enriched fragment of fibronectin. Biochem. Pharmacol. *81*, 866–872.

Othman, M. (2007). Platelet-type von Willebrand disease and type 2B von Willebrand disease: a story of nonidentical twins when two different genetic abnormalities evolve into similar phenotypes. Semin. Thromb. Hemost. *33*, 780–786.

Otsu, N. (1975). A threshold selection method from gray-level histograms. Automatica.

Parsons, J.T., Horwitz, A.R., and Schwartz, M.A. (2010). Cell adhesion: integrating cytoskeletal dynamics and cellular tension. Nat Rev Mol Cell Biol *11*, 633–643.

Peng, Y., Shrimpton, C.N., Dong, J.-F., and López, J.A. (2005). Gain of von Willebrand factor-binding function by mutagenesis of a species-conserved residue within the leucine-rich repeat region of platelet glycoprotein Ibalpha. Blood *106*, 1982–1987.

Petrie, T.A., Capadona, J.R., Reyes, C.D., and García, A.J. (2006). Integrin specificity and enhanced cellular activities associated with surfaces presenting a recombinant fibronectin fragment compared to RGD supports. Biomaterials *27*, 5459–5470.

Phillips, J.C., Braun, R., Wang, W., Gumbart, J., Tajkhorshid, E., Villa, E., Chipot, C., Skeel, R.D., Kalé, L., and Schulten, K. (2005). Scalable molecular dynamics with NAMD. J Comput Chem *26*, 1781–1802.

Rabinowitz, I., Tuley, E.A., Mancuso, D.J., Randi, A.M., Firkin, B.G., Howard, M.A., and Sadler, J.E. (1992). von Willebrand disease type B: a missense mutation selectively abolishes ristocetin-induced von Willebrand factor binding to platelet glycoprotein Ib. Proc Natl Acad Sci USA *89*, 9846–9849.

Roca-Cusachs, P., Iskratsch, T., and Sheetz, M.P. (2012). Finding the weakest link: exploring integrin-mediated mechanical molecular pathways. J Cell Sci *125*, 3025–3038.

Ruggeri, Z.M. (1999). Structure and function of von Willebrand factor. Thrombosis and Haemostasis *82*, 576–584.

Ruggeri, Z.M. (2002). Platelets in atherothrombosis. Nat Med *8*, 1227–1234.

Ruggeri, Z.M. (2003). Von Willebrand factor, platelets and endothelial cell interactions. J Thromb Haemost *1*, 1335–1342.

Ruggeri, Z.M. (2004). Type IIB von Willebrand disease: a paradox explains how von Willebrand factor works. J Thromb Haemost *2*, 2–6.

Ruggeri, Z.M. (2007). Von Willebrand factor: looking back and looking forward. Thromb Haemostasis *98*, 55–62.

Ruggeri, Z.M. (2009). Platelet adhesion under flow. Microcirculation *16*, 58–83.

Ruggeri, Z.M., and Mendolicchio, G.L. (2007). Adhesion mechanisms in platelet function. Circulation Research *100*, 1673–1685.

Ruggeri, Z.M., Dent, J.A., and Saldívar, E. (1999). Contribution of distinct adhesive interactions to platelet aggregation in flowing blood. Blood *94*, 172–178.

Ruggeri, Z.M., Orje, J.N., Habermann, R., Federici, A.B., and Reininger, A.J. (2006). Activation-independent platelet adhesion and aggregation under elevated shear stress. Blood *108*, 1903–1910.

Russell, S.D., and Roth, G.J. (1993). Pseudo-von Willebrand disease: a mutation in the platelet glycoprotein Ib alpha gene associated with a hyperactive surface receptor. Blood *81*, 1787–1791.

Saalbach, A., Wetzel, A., Haustein, U.-F., Sticherling, M., Simon, J.C., and Anderegg, U. (2005). Interaction of human Thy-1 (CD 90) with the integrin alphavbeta3 (CD51/CD61): an important mechanism mediating melanoma cell adhesion to activated endothelium. Oncogene *24*, 4710–4720.

Sadler, J. (2005a). New concepts in von Willebrand disease. Annual Review of Medicine *56*, 173.

Sadler, J.E. (2005b). von Willebrand factor: two sides of a coin. J Thromb Haemost *3*, 1702–1709.

Sali, A., and Blundell, T.L. (1993). Comparative protein modelling by satisfaction of spatial restraints. J. Mol. Biol. *234*, 779–815.

Saoncella, S., Echtermeyer, F., Denhez, F., Nowlen, J.K., Mosher, D.F., Robinson, S.D., Hynes, R.O., and Goetinck, P.F. (1999). Syndecan-4 signals cooperatively with integrins in a Rho-dependent manner in the assembly of focal adhesions and actin stress fibers. Proc Natl Acad Sci USA *96*, 2805–2810.

Sarangapani, K.K., Marshall, B.T., McEver, R.P., and Zhu, C. (2011). Molecular stiffness of selectins. J Biol Chem *286*, 9567–9576.

Sarangapani, K.K., Yago, T., Klopocki, A.G., Lawrence, M.B., Fieger, C.B., Rosen, S.D., McEver, R.P., and Zhu, C. (2004). Low force decelerates L-selectin dissociation from P-selectin glycoprotein ligand-1 and endoglycan. J Biol Chem *279*, 2291–2298.

Savage, B., Almus-Jacobs, F., and Ruggeri, Z.M. (1998). Specific synergy of multiple substrate-receptor interactions in platelet thrombus formation under flow. Cell *94*, 657–666.

Savage, B., Saldívar, E., and Ruggeri, Z.M. (1996). Initiation of platelet adhesion by arrest onto fibrinogen or translocation on von Willebrand factor. Cell *84*, 289–297.

Schneider, S.W., Nuschele, S., Wixforth, A., Gorzelanny, C., Alexander-Katz, A., Netz,

R.R., and Schneider, M.F. (2007). Shear-induced unfolding triggers adhesion of von Willebrand factor fibers. Proc Natl Acad Sci USA *104*, 7899–7903.

Schubert, K., Polte, T., Bönisch, U., Schader, S., Holtappels, R., Hildebrandt, G., Lehmann, J., Simon, J.C., Anderegg, U., and Saalbach, A. (2011). Thy-1 (CD90) regulates the extravasation of leukocytes during inflammation. Eur. J. Immunol. *41*, 645–656.

Schwarz, U.S., and Gardel, M.L. (2012). United we stand: integrating the actin cytoskeleton and cell-matrix adhesions in cellular mechanotransduction. J Cell Sci *125*, 3051–3060.

Shankaran, H., Alexandridis, P., and Neelamegham, S. (2003). Aspects of hydrodynamic shear regulating shear-induced platelet activation and self-association of von Willebrand factor in suspension. Blood *101*, 2637–2645.

Shen, Y., Romo, G., Dong, J., Schade, A., McIntire, L., Kenny, D., Whisstock, J., Berndt, M., Lopez, J., and Andrews, R. (2000). Requirement of leucine-rich repeats of glycoprotein (GP) Ibalpha for shear-dependent and static binding of von Willebrand factor to the platelet membrane GP Ib-IX-V complex. Blood *95*, 903.

Springer, T.A. (2011). Biology and physics of von Willebrand factor concatamers. J Thromb Haemost *9 Suppl 1*, 130–143.

Springer, T.A., and Dustin, M.L. (2012). Integrin inside-out signaling and the immunological synapse. Current Opinion in Cell Biology *24*, 107–115.

Springer, T.A., Zhu, J., and Xiao, T. (2008). Structural basis for distinctive recognition of fibrinogen gammaC peptide by the platelet integrin alphaIIbbeta3. The Journal of Cell Biology *182*, 791–800.

Stricker, J., Aratyn-Schaus, Y., Oakes, P.W., and Gardel, M.L. (2011). Spatiotemporal constraints on the force-dependent growth of focal adhesions. Biophys J *100*, 2883–2893.

Sun, G., Zhang, Y., Huo, B., and Long, M. (2009). Surface-bound selectin-ligand binding is regulated by carrier diffusion. Eur Biophys J *38*, 701–711.

Szántó, T., Joutsi-Korhonen, L., Deckmyn, H., and Lassila, R. (2012). New insights into von Willebrand disease and platelet function. Semin. Thromb. Hemost. *38*, 55–63.

Takagi, J., Petre, B.M., Walz, T., and Springer, T.A. (2002). Global conformational rearrangements in integrin extracellular domains in outside-in and inside-out signaling. Cell *110*, 599–511.

Tischer, A., Cruz, M.A., and Auton, M. (2013). The linker between the D3 and A1 domains of vWF suppresses A1-GPIbα catch bonds by site-specific binding to the A1 domain. Protein Sci. *22*, 1049–1059.

Tiveron, M.C., Nosten-Bertrand, M., Jani, H., Garnett, D., Hirst, E.M., Grosveld, F., and Morris, R.J. (1994). The mode of anchorage to the cell surface determines both the function and the membrane location of Thy-1 glycoprotein. J Cell Sci *107 (Pt 7)*, 1783–1796.

Tovar-Lopez, F.J., Rosengarten, G., Westein, E., Khoshmanesh, K., Jackson, S.P., Mitchell, A., and Nesbitt, W.S. (2010). A microfluidics device to monitor platelet aggregation dynamics in response to strain rate micro-gradients in flowing blood. Lab Chip *10*, 291–302.

Turitto, V.T., and Baumgartner, H.R. (1979). Platelet interaction with subendothelium in flowing rabbit blood: effect of blood shear rate. Microvasc. Res. *17*, 38–54.

Ulrichts, H., Udvardy, M., Lenting, P.J., Pareyn, I., Vandeputte, N., Vanhoorelbeke, K., and Deckmyn, H. (2006). Shielding of the A1 domain by the D'D3 domains of von Willebrand factor modulates its interaction with platelet glycoprotein Ib-IX-V. J Biol Chem *281*, 4699–4707.

Varughese, K.I., Celikel, R., and Ruggeri, Z.M. (2002). Structure and function of the von Willebrand factor A1 domain. Curr. Protein Pept. Sci. *3*, 301–312.

Varughese, K.I., Ruggeri, Z.M., and Celikel, R. (2004). Platinum-induced space-group transformation in crystals of the platelet glycoprotein Ib alpha N-terminal domain. Acta Crystallogr. D Biol. Crystallogr. *60*, 405–411.

Veigel, C., Coluccio, L.M., Jontes, J.D., Sparrow, J.C., Milligan, R.A., and Molloy, J.E. (1999). The motor protein myosin-I produces its working stroke in two steps. Nature *398*, 530–533.

Wayman, A., Chen, W., McEver, R., and Zhu, C. (2010). Triphasic force dependence of E-selectin/ligand dissociation governs cell rolling under flow. Biophys J.

Weiss, H.J., Turitto, V.T., and Baumgartner, H.R. (1978). Effect of shear rate on platelet interaction with subendothelium in citrated and native blood. I. Shear rate--dependent decrease of adhesion in von Willebrand's disease and the Bernard-Soulier syndrome. J. Lab. Clin. Med. *92*, 750–764.

Wetzel, A., Chavakis, T., Preissner, K.T., Sticherling, M., Haustein, U.-F., Anderegg, U., and Saalbach, A. (2004). Human Thy-1 (CD90) on activated endothelial cells is a counterreceptor for the leukocyte integrin Mac-1 (CD11b/CD18). J Immunol *172*, 3850–3859.

Wetzel, A., Wetzig, T., Haustein, U.F., Sticherling, M., Anderegg, U., Simon, J.C., and Saalbach, A. (2006). Increased neutrophil adherence in psoriasis: role of the human endothelial cell receptor Thy-1 (CD90). J. Invest. Dermatol. *126*, 441–452.

Williams, A.F., and Gagnon, J. (1982). Neuronal cell Thy-1 glycoprotein: homology with immunoglobulin. Science *216*, 696–703.

Wu, T., Lin, J., Cruz, M., Dong, J., and Zhu, C. (2010). Force-induced cleavage of single VWFA1A2A3 tridomains by ADAMTS-13. Blood *115*, 370.

Wu, Y.P., van Breugel, H.H., Lankhof, H., Wise, R.J., Handin, R.I., De Groot, P.G., and Sixma, J.J. (1996). Platelet adhesion to multimeric and dimeric von Willebrand factor and to collagen type III preincubated with von Willebrand factor. Arteriosclerosis, Thrombosis, and Vascular Biology *16*, 611–620.

Xiang, X., Lee, C.-Y., Li, T., Chen, W., Lou, J., and Zhu, C. (2011). Structural basis and kinetics of force-induced conformational changes of an αA domain-containing integrin. PLoS ONE *6*, e27946.

Xiao, T., Takagi, J., Coller, B.S., Wang, J.-H., and Springer, T.A. (2004). Structural basis for allostery in integrins and binding to fibrinogen-mimetic therapeutics. Nature *432*, 59–67.

Yago, T., Lou, J., Wu, T., Yang, J., Miner, J.J., Coburn, L., López, J.A., Cruz, M.A., Dong, J.-F., Mcintire, L.V., et al. (2008). Platelet glycoprotein Ibalpha forms catch bonds with human WT vWF but not with type 2B von Willebrand disease vWF. J Clin Invest *118*, 3195–3207.

Yago, T., Wu, J., Wey, C.D., Klopocki, A.G., Zhu, C., and McEver, R.P. (2004). Catch bonds govern adhesion through L-selectin at threshold shear. J Cell Biol *166*, 913–923.

Yago, T., Zarnitsyna, V.I., Klopocki, A.G., McEver, R.P., and Zhu, C. (2007). Transport governs flow-enhanced cell tethering through L-selectin at threshold shear. Biophys J *92*, 330–342.

Yan, R., Mo, X., Paredes, A.M., Dai, K., Lanza, F., Cruz, M.A., and Li, R. (2011). Reconstitution of the platelet glycoprotein Ib-IX complex in phospholipid bilayer Nanodiscs. Biochemistry *50*, 10598–10606.

Ye, F., Kim, C., and Ginsberg, M.H. (2012). Reconstruction of integrin activation. Blood *119*, 26–33.

Zhou, Y., Hagood, J.S., Lu, B., Merryman, W.D., and Murphy-Ullrich, J.E. (2010). Thy-1-integrin alphav beta5 interactions inhibit lung fibroblast contraction-induced latent transforming growth factor-beta1 activation and myofibroblast differentiation. J Biol Chem *285*, 22382–22393.

Zhu, C., Jiang, N., Huang, J., Zarnitsyna, V.I., and Evavold, B.D. (2013). Insights from in situ analysis of TCR-pMHC recognition: response of an interaction network. Immunol. Rev. *251*, 49–64.

Zhu, C., Long, M., Chesla, S.E., and Bongrand, P. (2002). Measuring Receptor/Ligand Interaction at the Single-Bond Level: Experimental and Interpretative Issues. Ann Biomed Eng *30*, 305–314.

Zhu, C., Yago, T., Lou, J., Zarnitsyna, V.I., and McEver, R.P. (2008). Mechanisms for flow-enhanced cell adhesion. Ann Biomed Eng *36*, 604–621.